PLACE IN RETURN BOX
to remove this checkout from your record.
TO AVOID FINES return on or before date due.

DATE DUE	DATE DUE	DATE DUE

1/98 c/CIRC/DateDue.p65-p.14

TIME-DOMAIN IMAGING OF RADAR TARGETS USING ULTRA-WIDEBAND OR SHORT PULSE RADARS

by

Yingcheng Dai

A DISSERTATION

Submitted to
Michigan State University
in partial fulfillment of the requirements
for the degree of

DOCTOR OF PHILOSOPHY

Department of Electrical Engineering

1997

ABSTRACT

TIME-DOMAIN IMAGING OF RADAR TARGETS USING ULTRA-WIDEBAND OR SHORT PULSE RADARS

By

Yingcheng Dai

The development of viable short-pulse radar system has renew the interest in time domain imaging performed directly in time-domain with temporally measured signal. Since the short-pulse response of a target provides significant information about the positions and strengths of scattering centers, and if observations are made over a wide range of aspect angle, one might created an image of the target using the short-pulse response information. In this thesis, we have developed and implemented a time-domain radar imaging technique based on a space-time magnetic field integral equation, using a sine modulated exponential pulse, and employing the inverse Radon transform. Images of various aircraft models were created from measured target responses over a wide band of frequencies and over the entire range of aspect angles.

For the limited-view problem, two techniques have been proposed to process this practical situation. One of the approach is the method of projections onto convex sets (POCS) which has been use in image processing for a long time. We extend this

approach to radar imaging for the first time and show some useful results. Another approach which we have demonstrated is to process the available measured projections in order to generate an estimate of the full set of projections, an image which is called a sinogram. The goal of this approach is to recover the sinogram from the available measured data using linear prediction. Since the scattered field of a target can be written as a superposition of distinct specular reflection arising from scattering centers on the target, the position and strength of the scattering centers can be predicted using linear prediction with the change of the observation angle. Thus the missing data can be predicted before reconstructing the image.

In the imaging of complex radar target, the PO approximation is used in the reconstruction algorithm. However, the PO approximation is inadequate for scattering problems of a complex shaped conducting object such as aircraft. At high frequency, edge diffractions, multiple reflections, creeping waves, and surface travelling waves may also be important scattering mechanisms. Additionally, the spectral and angular windows for data are usually restricted by practical constraints. Therefore the time domain image of a aircraft may be different from their geometrical shape. We have investigated time domain imaging of aircraft employing SMEP responses, and interpret the reconstructed image from a new approach, based on analysis of the scattering mechanisms and the back-projection algorithm utilized in image retrieval. The time-domain inverse scattering identity with the incorporation of Geometrical Theory of Diffraction (GTD) is derived and some interesting experimental results are provided.

ACKNOWLEDGMENTS

I would like to express my sincerest appreciation to Dr. K. M. Chen. His encouragement to finish my graduate studies at Michigan State University and his teaching and guidance during my research will not be forgotten. Thank him very much for his generous support throughout my work. I am especially grateful to Dr. E. J. Rothwell. His sincere interest, encouragement and expert technical advice will long be remembered. To D. P. Nyquist, thank for his outstanding teaching, deep concern and guidance. To Dr. Byron Drachman, thank him for his participating as a member of my committee.

I also want to thank my fellows at EM lab. It has been a great pleasure to work and learn with them.

Finally, I would like to express my special gratitude to my wonderful wife, Qing Li, and my parents for their constant love, financial support, and understanding.

TABLE OF CONTENTS

LIST OF TABLES

LIST OF FIGURES

CHAPTER 1

INTRODUCTION

Microwave imaging of airborne targets has received considerable interest in recent years. Most attention has focused on the use of inverse synthetic aperture radar (ISAR) [50,51]. In ISAR, the target is modelled as a collection of scattering centers at sufficiently high frequencies and the image is constructed from a 2-D inverse Fourier transform of the Cartesian frequency spectra, or a backprojection algorithm along with a 1-D inverse Fourier transform of the polar frequency spectra [50]. The development of viable short-pulse radar systems has renewed the interest in time-domain imaging performed directly in the time domain with temporally measured signals. The use of time- domain techniques was first discussed by Kennaugh and Cosgroff in 1957 [6]. Since then, many researchers have developed approaches to the inverse scattering problem [7-12]. They have shown that the target impulse, step, and ramp responses are related to the target geometry based on physical optics principles. Under the physical optics approximation, Bojarski has established a Fourier transform relationship between the geometry of the conducting scatterer and a form of the scattering cross section [14]. Since this approach is based on the physical optics approximation, it is valid only in the limit of high frequency. When the size of the scatterer is comparable to the incident pulsewidth, the physical optics solution is inadequate for this scattering problem. Furthermore, the impulse, step, or ramp response of the target is hard to obtain in practice.

The purpose of this thesis is to develop and implement an imaging technique directly in the time domain. Since the short-pulse response of a target provides significant information about the positions and strengths of scattering centers, and if observations are made over a wide range of aspect angles, one might create an image of the target using the short-pulse response information. The starting point of this thesis is the time-domain magnetic field integral equation (MFIE). The derivation of the MFIE and its numerical solutions are provided in chapter 2. Chapter 3 gives the time-domain inverse scattering identity (thickness function) developed from the time-domain MFIE and the Radon transform. It shows that the size and shape of an object can be obtained from its cross-sectional area function, and that the problem can be reduced to the classical Radon problem. In this process, the Sine-Modulated Exponential Pulse (SMEP) is used as the incident field.

Since the area function can be estimated from the scattered field when the incident field is a SMEP, the remaining problem is thus essentially that of reconstruction from projections. The basic idea of reconstruction of an image from a series of its projections appears to have been first discussed by Radon [16]. The techniques that exist for reconstruction fall into two directions. The whole operation can be done in frequency space directly, or the equivalent of these expressions can be transformed into the spatial domain. Whether implemented in the spatial domain or in the frequency domain, the reconstruction algorithms can be conveniently interpreted by means of a straightforward and interesting theorem, which is the projection-slice theorem. This theorem states that the Fourier transform of a projection is a center cross section of the Fourier transform of the projected object. Most modern tomographic systems are based on this theorem. Thus, by formulating the object reconstruction problem as a form of the Radon problem, the

2

many reconstruction techniques and the properties of reconstruction from projections which are well developed in other fields for the two-dimensional case can be extended and applied to the inverse scattering problem. Chapter 4 gives the development of the reconstruction algorithm and provides clear images with highly-defined edges using stepped-frequency, multi-aspect measurement data of aircraft models.

For complete reconstruction, the time-domain approach requires data for all aspect directions. However, in practice, information usually available only for limited view-angles; thus, it is necessary to analyze the effect of incomplete information which may cause the inverse problem to be ill-posed in nature. The limited-view problem has attracted considerable attention in computed tomography imaging research, and techniques for dealing with it have been proposed. Techniques can be put into two categories: transform techniques that incorporate no a priori information, and finite series expansion methods that may incorporate a priori information as constraints. The transform techniques are usually single-pass direct reconstruction [18-20] while the finite series expansion methods are usually iterative [21-27]. Projection onto convex sets (POCS) in particular has shown great flexibility in dealing with known geometric constraints and with noise. We will extend POCS into radar target imaging. The details are carried out in chapter 5. Also in chapter 5 we will demonstrate a new reconstruction algorithm for radar imaging in the limited-angle case. The goal of this approach is to recover the sinogram from the available measured data using linear prediction. Since the scattered field of a target can be written as a superposition of distinct specular reflections arising from scattering centers on the target, the trace of the scattering centers can be predicted using linear prediction with the change of the observation angle. Thus, the missing data may be predicted before reconstructing the image.

In the proposed time domain imaging technique, the physical optics approximation is used to model the scattered field of an aircraft. However, the PO approximation is inadequate for scattering problems of a complex shaped conducting object such as aircraft. At high frequency, edge diffractions, multiple reflections, creeping waves, and surface travelling waves may also be important scattering mechanisms. Additionally, the spectral and angular windows for data are usually restricted by practical constraints. Therefore, the time domain image of an aircraft may be different from its geometrical shape. In chapter 6 we will investigate time domain imaging of aircraft employing SMEP responses, and interpret the reconstructed image from a new approach based on analysis of the scattering mechanisms and the back-projection algorithm utilized in image retrieval. The time-domain inverse scattering identity with the incorporation of Geometrical Theory of Diffraction (GTD) is derived and some interesting experimental results are provided.

CHAPTER 2

INTEGRAL EQUATION AND ITS SOLUTION

FOR TRANSIENT SCATTERING

2.1   Introduction

Before the advent of the high-speed digital computers, most electromagnetic scattering problems were solved in the frequency domain. The boundary value solutions associated with electromagnetic radiation and scattering phenomena were based upon analytical techniques that attempted to generate closed-form solutions and were, therefore, limited to a few classes of problems. Approximate techniques such as geometric optics (GO), physical optics (PO), and the Rayleigh approximation were applied to other problems to obtain estimates of the scattered response. With the advent of high-speed computers, the frequency-domain integral equation technique has also provided many interesting and useful results.

The integral equation and its solution could also be obtained directly in the time domain [1,2]. Indeed, the frequency-domain integral equations have their time-domain counterparts [3]. With the developments of high resolution radar and electromagnetic pulse (EMP), the investigation of radiation and scattering of transient waveforms from conducting objects has attracted increasing interest. There are two integral-equation techniques available for solving transient electromagnetic problems [3]. One of them involves the Fourier transform of the frequency response of the scatter to synthesize the

5

time-domain response. The alternative technique is based on the time-domain integral equation and its subsequent solution using the marching-on-in-time method. The details of this approach and other approximate techniques will described in Section 2.3. The derivation of the general integral equation for the scattering problem is covered in Section 2.2.

2.2   Time-Domain Integral Equations

The integral equation method has several advantages, such as geometrical generality, compactness, and computability, which make it an attractive approach to solving electromagnetic boundary value problems. In this section we will provide in detail the derivations of the time-domain integral equations directly, rather than via the inverse Fourier transform of the frequency-domain solution [2].

2.2.1   Magnetic Field Integral Equation

Consider the scattering of electromagnetic waves by good conductors, as shown in Figure 2.1. The electric and magnetic fields of the scatted wave satisfy the time-domain Maxwell equations in the source-free, free space region outside the conductor.

$$\nabla \times \vec{E}^s(\vec{r},t) = -\mu_0 \frac{\partial}{\partial t} \vec{H}^s(\vec{r},t)$$

$$\nabla \times \vec{H}^s(\vec{r},t) = \varepsilon_0 \frac{\partial}{\partial t} \vec{E}^s(\vec{r},t)$$

$$\nabla \cdot \vec{E}^s(\vec{r},t) = 0$$

$$\nabla \cdot \vec{H}^s(\vec{r},t) = 0$$

(2.1)

where ε_0 and μ_0 are the permittivity and permeability of free space, respectively, and $\vec{r}$
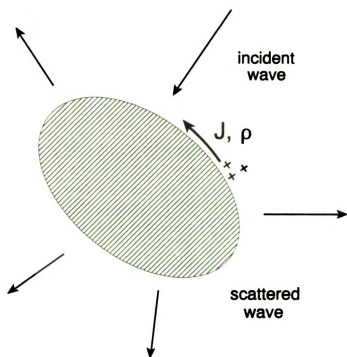
Figure 2.1 Scattering of an incident electromagnetic wave by a perfect conducting body.

is the position vector.

These fields can be derived from a scaler potential ϕ^s and a vector potential $\vec{A}^s$ such that

$$\vec{E}^s(\vec{r},t) = -\nabla\phi(\vec{r},t) - \frac{\partial}{\partial t}\vec{A}^s(\vec{r},t), \quad \vec{H}^s(\vec{r},t) = \frac{1}{\mu_0}\nabla\times\vec{A}^s(\vec{r},t) \qquad (2.2)$$

These potentials are related to each other by the Lorentz condition

$$\nabla\cdot\vec{A}^s(\vec{r},t) + \frac{1}{c^2}\frac{\partial}{\partial t}\phi^s(\vec{r},t) = 0 \qquad (2.3)$$

where c is the free-space light speed. Applying equations (2.1) and (2.2) yield the wave equations satisfied by ϕ^s and $\vec{A}^s$

$$\left(\nabla^2 - \frac{1}{c^2}\frac{\partial^2}{\partial t^2}\right)\phi^s(\vec{r},t) = 0, \quad \left(\nabla^2 - \frac{1}{c^2}\frac{\partial^2}{\partial t^2}\right)\vec{A}^s(\vec{r},t) = 0 \qquad (2.4)$$

The retarded solutions of the wave equations (2.4) are

$$\phi^s(\vec{r},t) = \frac{1}{4\pi\varepsilon_0}\int_s \frac{\varrho(\vec{r}',t - |\vec{r}-\vec{r}'|/c)}{|\vec{r}-\vec{r}'|}ds'$$

$$\vec{A}^s(\vec{r},t) = \frac{\mu_0}{4\pi}\int_s \frac{\vec{J}(\vec{r}',t - |\vec{r}-\vec{r}'|/c)}{|\vec{r}-\vec{r}'|}ds' \qquad (2.5)$$

where $\vec{J}$ is the current density and ϱ is the charge density on the surface of the body. They are related by the continuity equation

$$\nabla\cdot\vec{J}(\vec{r},t) + \frac{\partial}{\partial t}\varrho(\vec{r},t) = 0 \qquad (2.6)$$

Substituting (2.5) into (2.2) gives the following integral representation of the scattered magnetic field $\vec{H}^s(\vec{r},t)$ at a point $\vec{r}$ exterior to the scatterer and at time t

8

$$\vec{H}^s(\vec{r},t) = \frac{1}{4\pi}\int_s\left[\vec{J}(\vec{r}',\tau)\times\nabla'(\frac{1}{R})-\frac{1}{CR^2}\vec{R}\times\frac{\partial}{\partial\tau}\vec{J}(\vec{r}',\tau)\right]ds' \qquad (2.7)$$

where

$$\vec{R} = \vec{r}-\vec{r}', \qquad R = |\vec{r}-\vec{r}'| \qquad (2.8)$$

and τ is the retarded time defined by

$$\tau = t - \frac{1}{c}|\vec{r}-\vec{r}'| \qquad (2.9)$$

The operator ∇' acts on the source point $\vec{r}'$. Equation (2.7) expresses the magnetic field of the scattered wave at a point in space and time as a composition of excitations from individual points of the scatterer's surface at specific retarded times.

The derivation of the Magnetic Field Integral Equation (MFIE) begins by applying the appropriate boundary condition. On the surface of a perfectly conducting scatterer, the total magnetic field is related to the surface current density at all times through the equation

$$\vec{J}(\vec{r},t) = \hat{n}\times[\vec{H}^i(\vec{r},t)+\vec{H}^s(\vec{r},t)] \qquad (2.10)$$

where $\hat{n}$ is the outgoing unit vector normal to S.

Applying (2.10) to the representation (2.7) yields the time-dependent MFIE [2]

$$\vec{J}(\vec{r},t) = 2\hat{n}\times\vec{H}^i(\vec{r},t)+\frac{\hat{n}}{2\pi}\times\int_s[\frac{1}{c}\frac{\partial}{\partial\tau}\vec{J}(\vec{r}',\tau)+\frac{\vec{J}(\vec{r}',\tau)}{R}]\times\frac{\vec{R}}{R^2}ds' \qquad (2.11)$$

where the integral is taken to be a principal value (P.V.) type. As we will see later, the special form of this integral equation plays a fundamental role in enabling us to construct its solution using a marching-on-in-time method.

9

2.2.2 Electric Field Integral Equation

The time-domain scattering of an electromagnetic wave by a perfect conductor can also be formulated in terms of an Electric Field Integral Equation (EFIE). Using (2.5) and (2.2), one can obtain the following integral representation of the scattered electric field $\vec{E}^s(\vec{r},t)$ at a point $\vec{r}$ exterior to the scatterer and at time t, in terms of the retarded values of the surface charge density ϱ and the surface current density $\vec{J}$ induced on the scatterer's surface S

$$\vec{E}^s(\vec{r},t) = -\frac{1}{4\pi}\int_s \frac{1}{R}\left\{\frac{1}{\varepsilon_o R}\nabla R \varrho(\vec{r}',\tau) + \frac{1}{\varepsilon_0}\frac{\partial}{\partial\tau}\varrho(\vec{r}',\tau)\nabla R + \mu_0\frac{\partial}{\partial\tau}\vec{J}(\vec{r}',\tau)\right\}ds' \quad (2.12)$$

The EFIE for the scattering problem involving a perfect conductor may be derived from the following boundary condition which holds for all points on S

$$\hat{n}\times\left[\vec{E}^i(\vec{r},t)+\vec{E}^s(\vec{r},t)\right] = 0 \quad\quad\quad (2.13)$$

Applying condition (2.13) one arrives at the following EFIE involving ϱ and $\vec{J}$

$$\hat{n}\times\vec{E}^i(\vec{r},t) = \frac{\hat{n}}{2\pi}\times\int_s\left[\frac{\mu_0}{R}\frac{\partial}{\partial\tau}\vec{J}(\vec{r}',\tau)-\frac{\varrho(\vec{r}',\tau)}{\varepsilon_0}\frac{\vec{R}}{R^3}-\frac{1}{\varepsilon_0}\frac{\partial}{\partial\tau}\varrho(\vec{r}',\tau)\cdot\frac{\vec{R}}{cR^2}\right]ds' \quad (2.14)$$

where the integral involved is also of the P.V. type. Clearly, the EFIE is a Fredholm integral equation of the first kind while the MFIE is a Fredholm integral equation of the second kind.

2.3 Numerical Solution of MFIE

There are two useful integral equation techniques available for solving transient electromagnetic problems. One of them involves using the Fourier transform of the

frequency response of the scatter to synthesize the time-domain response [3]. The alternative technique is based on the time-domain integral equation and its subsequent solution using the marching-on-in-time method. Here, we will describe the marching-on-in-time method in detail.

2.3.1 Rigorous Solutions

A commonly used technique for solving transient scattering problems is the marching-on-in-time method. Consider the MFIE

$$\bar{J}_s(\bar{r},t) = 2\hat{n}\times\bar{H}^i(\bar{r},t) - \frac{\hat{n}}{2\pi}\times\int\left\{\frac{1}{c}\frac{\partial}{\partial\tau}\bar{J}_s(\bar{r}',\tau) + \frac{\bar{J}_s(\bar{r}',\tau)}{R}\right\}\times\frac{\bar{R}}{R^2}ds' \qquad (2.15)$$

where $\int$ denotes the principal value integral, and $\tau = t - R/c$ is the retarded time.

This equation is clearly a Fredholm integral equation of the second kind. Note that for a given time t, the unknown $\bar{J}_s$ inside the integral has an argument $\tau = t - R/c$. Since the principal value integral excludes the point $R=0$, τ is always less than t. Thus, we can regard (2.15) as an expression for the unknown current $\bar{J}_s(t)$, at any given time t, in terms of the known incident term $2\hat{n}\times\bar{H}^i$, and an integral which is also known from the past history of the current $\bar{J}_s$. This procedure forms the basis of an iterative technique for constructing the solution of (2.15). The solution is started at the time $t=t_o$, invoking causality which guarantees that all past currents and their derivatives are identically zero for $t<t_o$. The solution is then constructed by gradually building it up for $t>t_o$, by marching on in time using a time-stepping procedure.

11

The method of moments can be applied to the solution of equation (2.15). First,

let's express the unknown $\vec{J}_s$ in an expansion of pulse basis functions

$$\vec{J}_s(\vec{r}',t) = \sum_{i=1}^{N_s} \sum_{j=1}^{N_t} \vec{A}_{ij}(\vec{r}',t) V_i(\vec{r}') U_j(t) \qquad (2.16)$$

where

$$V_i(\vec{r}') = \left\{ \begin{array}{ll} 1 & \text{for } \vec{r}' \text{ on the surface segment center at } \vec{r}_i \\ 0 & \text{elsewhere} \end{array} \right.$$

$$U_j(t) = \left\{ \begin{array}{ll} 1 & \text{for } t \text{ in the time interval centered at } t_j \\ 0 & \text{elsewhere} \end{array} \right.$$

The unknown $\vec{A}_{ij}$ are the vector weight coefficients for the space-time sampled values of

the current $\vec{J}_s$ on the surface of the structure which is assumed to be subdivided into N_s

patches centered at r_i. The total time is also assumed to be subdivided into N_t time-steps.

Since there is $\partial \vec{J}_s / \partial t$ in equation (2.15), $\vec{J}_s(t)$ and $\partial \vec{J}_s / \partial t$ should be differentiable

at the observation time t, so we use a second-order Lagrange interpolation to approximate

the current

$$\vec{A}_{ij}(\vec{r}',t) = \vec{A}_{ij}(t) = \frac{(t-t_j)(t-t_{j+1})}{(t_{j-1}-t_j)(t_{j-1}-t_{j+1})} \vec{A}_{i\,j-1} + \frac{(t-t_{j-1})(t-t_{j+1})}{(t_j-t_{j-1})(t_j-t_{j+1})} \vec{A}_{i\,j+1}$$
$$+ \frac{(t-t_{j-1})(t-t_j)}{(t_{j+1}-t_{j-1})(t_{j+1}-t_j)} \vec{A}_{i\,j+1} \qquad (2.17)$$

where $\vec{A}_{ij}$ is the sample value of $\vec{J}_s$ at the center point of patch Δs_i at time t_j. Then,

substituting equation (2.16) into (2.15), and point matching at the center point of each

patch Δs_i gives

$$J_s(\vec{r}_i,t) = 2\hat{n} \times \vec{H}^i(\vec{r}_i,t) - \frac{\hat{n}}{2\pi} \times \int \sum_{p=1}^{N_s} \sum_{q=1}^{N_t} \left[\frac{\partial}{\partial \tau} \vec{A}_{pq}(\tau) \frac{1}{cR^2} + \vec{A}_{pq}(\tau) \frac{1}{R^3} \right] \times \vec{R} \, V_p(\vec{r}') \, U_q(\tau) \, ds'$$

(2.18)

$$i = 1,2,...N_s$$

Note that $p=i$ gives the contribution of the principal value integral due to the induced currents in the self-patch itself. However, it can be shown that this contribution is zero if Δs_i is a flat surface

$$\vec{J}_s \times \vec{R} = \hat{n} J_s R \quad \rightarrow \quad \hat{n} \times (\vec{J}_s \times \vec{R}) = \hat{n} \times \hat{n} J_s R = 0$$

(2.19)

We can consider $\vec{J}_s$ and R to be constant within patch Δs_p, and thus the integral over each patch can be approximated by multiplying the current value at point $\vec{r}_p$ with the area Δs_p. Then

$$J_s(\vec{r}_i,t) = 2\hat{n} \times \vec{H}^i(\vec{r}_i,t) - \frac{\hat{n}}{2\pi} \times \sum_{p=1p\ne i}^{N_s} \sum_{q=1}^{N_t} \Delta s_p \left[\frac{\partial}{\partial \tau} \vec{A}_{pq}(\tau) \frac{1}{cR_{ip}^2} + \vec{A}_{pq}(\tau) \frac{1}{R_{ip}^3} \right] \times \vec{R}_{ip} U_q(\tau) \qquad i=1,2,...N_s$$

(2.20)

where $R_{ip} = |\vec{r}_i - \vec{r}_p|$. Point matching at time t_j, and letting $q = j - int\left[\frac{R_{ip}}{c\Delta t} + 0.5 \right]$, where

$int[\cdots]$ denotes taking the integer part of the data, equation (2.20) becomes

$$J_s(\vec{r}_i,t_j) = \vec{A}_{ij} = 2\hat{n} \times \vec{H}^i(\vec{r}_i,t_j) - \frac{\hat{n}}{2\pi} \times \sum_{p=1p\ne i}^{N_s} \Delta s_p \left\{ \frac{1}{cR_{ip}^2} \left[\frac{\partial \vec{A}_{pq}(\tau)}{\partial \tau} \right]_{t=t_j} + \frac{1}{R_{ip}^3} \vec{A}_{pq}(\tau) \Big|_{t=t_j} \right\} \times \vec{R}_{ip} \qquad j=1,...,N_t$$

(2.21)

The sample points in time are not independent of the space sample points used. In order to let the two adjacent current sample in space not fall in the same time interval,

the time sample spacing Δt must be related to the space sample spacing ΔR by

$$c\Delta t \leq \Delta R \qquad (2.22)$$

Finally, we can use a method of marching-on-in-time to solve the problem. First, assuming the start time is t_0, and all the surface currents on S are zero for all time less than t_0 to view the integral equation as an initial value problem. For instance, let us assume that at time t_1 the incident field has just reached the scatterer. By virtue of the retardation and the principal value nature of the integral, a current is induced on part of the scatterer which is equal to $2\hat{n} \times \vec{H}^i(\vec{r}_1, t_1)$. As the time progresses further to t_2, the current at each point is then given by the known incident field $2\hat{n} \times \vec{H}^i(\vec{r}, t_2)$ plus a contribution from current at other points on the scatterer at earlier times which is also known. Using this idea gives

$$for\ j{=}1, \quad \vec{A}_{ij} = \vec{A}_{i1} = 2\hat{n} \times \vec{H}^i(\vec{r}_i, t_1)$$

$$(2.23)$$

$$for\ j{=}2, \quad \vec{A}_{ij} = \vec{A}_{i2} = 2\hat{n} \times \vec{H}^i(\vec{r}_i, t_2) + \frac{\hat{n}}{2\pi} \times \sum_{\substack{p=1 \\ p \neq i}}^{N_s} \left\{ \frac{1}{cR_{ip}^2} \frac{\partial}{\partial \tau} \vec{A}_{pq}(\tau) \Big|_{t=t_2} + \frac{1}{R_{ip}^3} \vec{A}_{pq}(\tau) \right\} \times \vec{R}_{ip} \Delta s_p$$

$$\vdots \qquad \vdots$$

Thus, marching on in time will allow us to build up the current solution from previously known values. This method has many advantages, such as ease of programming and speed. Also, the solution is usually explicit and does not involve the inversion of large matrices. However, a major disadvantage of the method is that the computed solution often becomes unstable as time progresses, usually taking the form of a very regular exponentially increasing oscillation which alternates in sign at each time-

14

step [4,5]. The cause of this instability will be seen to be related to the existence of resonant frequencies at which the corresponding frequency domain integral equation has more than one solution.

2.3.2 Instabilities In Marching-on-in-Time Methods

The occurrence of exponentially increasing instabilities is a common feature of time marching method for solving transient scattering problems. In this section we will examine how the instability arises and describe a simple method to eliminate the instability. More details can be found in Rynne [4] and Smith [5].

The system equation (2.21) can be written as

$$\frac{1}{2}\vec{A}_{i,j} = \hat{n}_i \times \vec{H}_{i,j} + \hat{n}_i \times \sum_{p=1}^{N_s} \sum_{q=1}^{N_q} a_{pq}^i \vec{A}_{p,j-q} \qquad (2.24)$$

where $i = 1,2\cdots N_s$, $j = 1,2\cdots N_t$, a_{pq}^i are some constants and $N_q = int\left[\dfrac{R_{ip}}{c\Delta t} + 0.5\right]$

Now, recast this system of coupled linear equations as follows. Introduce the auxiliary variables

$$\vec{A}_{p,j}^{(q)} = \vec{A}_{p,j-q} \qquad p=1,\cdots,N_s \quad q=1,\cdots,N_q \qquad (2.25)$$

These are vectors in R^3. Fix i and j. Then equation (2.24) shows that each component of the 3-vector $A_{i,j}^{(0)}$ is a linear combination of the components of the $N_s N_q$-length vector $\vec{A}_{q,j}^{(p)}$ and the component of the forcing term $\hat{n}_i \times \vec{H}_{i,j}$, and, moreover,

$$\vec{A}_{i,j}^{(1)} = \vec{A}_{i,j-1}^{(0)}, \quad \vec{A}_{i,j}^{(2)} = \vec{A}_{i,j-1}^{(1)}, \cdots, \quad \vec{A}_{i,j}^{(N_t)} = \vec{A}_{i,j-1}^{(N_t-1)} \qquad (2.26)$$

In short, each component of any such vector $A_{i,j}^{(p)}$ is a linear combination of the components of the $N_s N_q$-length vector $\vec{A}_{q,j}^{(p)}$ and the component $\hat{n}_i \times \vec{H}_{i,j}$.

Now, let Y_j denote the following column vector in $R^{3N_s N_t}$ assembled from the auxiliary variables $\vec{A}_{q,j}^{(p)}$ ($q=1,...,N_s$ and $q=1,...,N_q$)

$$Y_j = [\vec{A}_{1,j}^{(0)}, \vec{A}_{1,j}^{(1)},...,\vec{A}_{1,j}^{(N_t)},...,\vec{A}_{N_s,j}^{(0)},...,\vec{A}_{N_s,j}^{(N_t)}]^T \qquad (2.27)$$

Also, let h_j denote the following column vector in $R^{3N_s N_q}$ assembled from the forcing terms

$$h_j = [\hat{n}_1 \times \vec{H}_{1,j}, O, ..., O, \hat{n}_2 \times \vec{H}_{2,j}, O, ..., O,..., \hat{n}_{N_s} \times \vec{H}_{N_s,j}, O, ..., O]^T \qquad (2.28)$$

Here O denotes the zero vector in R^3. Then

$$Y_j = BY_{j-1} + h_j \qquad (2.29)$$

Here B is a suitable matrix in terms of the constants a_{pq}^i.

The initial quiescence of the system before the transient arrives requires that $Y_o=0$. If H^{inc} represents a transient of finite duration then $H_o=0$, and $H_j=0$, for all j exceeding some fixed M. Hence $h_j=0$ for $j>M$. The solution is therefore (when $j>M$)

$$Y_j = B^{(j-M)}(h_M + Bh_{M-1} + ... + B^{M-1}h_1) \qquad (2.30)$$

Thus, if B has an eigenvalue of modulus exceeding 1, the vector Y_j will grow

exponentially in modulus. To demonstrate this, suppose that B has diagonal Jordan form

$$\Lambda = diag(\lambda_1, \lambda_2, \cdots, \lambda_{N_sN_q}) \tag{2.31}$$

where $B=U^{-1}\Lambda U$ for some non-singular matrix U. Denoting UY_j by Z_j, the system (2.29) is equivalent to

$$Z_j = \Lambda Z_{j-1} + Uh_j \tag{2.32}$$

The homogeneous solution to (2.32) are of the form

$$Z_j = [a_1\lambda_1^j, a_2\lambda_2^j, \ldots, a_{N_sN_q}\lambda_{N_sN_q}^j]^T \tag{2.33}$$

where $a_1, a_2, \ldots$ are constants, and any nonzero component is unstable if its corresponding eigenvalue λ_i is of modulus exceeding 1.

There is a simple remedy to the problem of the onset of instability. Consider the following weighted average across 3 times steps:

$$\bar{Y}_j = (Y_{j+1} + 2Y_j + Y_{j-1})/4 \tag{2.34}$$

Therefore we replace (2.29) by

$$Y_j = \frac{1}{4}(B^2 + 2B + I)Y_{j-1} + (2I + B)h_j \tag{2.35}$$

which represents the effect of doing two time marching steps followed by an averaging process (2.34). The eigenvalues of $(B^2+2B+I)/4$ are $(\lambda+1)^2$, where λ is any eigenvalue of B. This has the virtue of shifting the troublesome eigenvalue near -1 to around zero, and more generally of shifting any eigenvalue which may be slightly outside the unit circle to inside. So this process will almost shift all the eigenvalues of the unstable marching process inside the unit circle. Sample numerical results will be provided in Chapter 4.

2.3.3 Approximations

For scatterers that are large compared to the wavelength, the physical optics approximation is a well-known method in the frequency domain. Similar approximations can also be obtained in the time domain. In this section, we will extend the idea of the physical-optics approximation in the frequency domain into the time domain.

For a perfectly conducting body, the surface-current-density distribution derived in the frequency domain under the physical optics approximation is

$$
\vec{J}_{po}(\vec{r},\omega) = \begin{cases} 2\,\hat{n}\times\vec{H}^{i}(\vec{r},\omega) & \vec{k}^{i}\cdot\hat{n}<0 \\ 0 & \vec{k}^{i}\cdot\hat{n}>0 \end{cases} \tag{2.36}
$$

Where $\hat{n}$ is the unit vector normal to the surface at point $\vec{r}$, $\vec{H}^{i}(\vec{r},\omega)$ is the incident magnetic field with angular frequency ω, and $\vec{k}^{i}$ is the incident wave vector. For a time-function excitation, the incident fields may be decomposed into their frequency-domain components by superposition as follows

$$
\vec{h}^{i}(\vec{R},t) = \sum_{m} A_{m}\hat{H}^{i}(\vec{R},\omega_{m}) = \sum_{m} \vec{H}_{m}^{i}(\vec{R},\omega_{m}) \tag{2.37}
$$

and

$$
\vec{J}_{po}(\vec{r},t) = \begin{cases} \displaystyle\sum_{m} 2\hat{n}\times\vec{H}^{i_{m}}(\vec{r},\omega_{m}) = 2\,\hat{n}\times\vec{h}^{i}(\vec{r},t) & \vec{k}^{i}\cdot\hat{n}<0 \\ 0 & \vec{k}^{i}\cdot\hat{n}>0 \end{cases} \tag{2.38}
$$

Under the far-zone approximations, equation (2.7) can be simplified as

18

$$\vec{h}_{po}^{s}(\vec{r},t) = \frac{1}{4\pi}\int_{s}\left[\vec{J}(\vec{r}',\tau)\times\nabla'(\frac{1}{R}) - \frac{1}{cR^2}\vec{R}\times\frac{\partial}{\partial\tau}\vec{J}(\vec{r}',\tau)\right]ds'$$

$$= \frac{1}{4\pi}\int_{s}\left[\vec{J}(\vec{r}',\tau)\times\frac{\vec{R}}{R^3} + \frac{\partial\vec{J}(\vec{r}',\tau)}{\partial\tau'}\times\frac{\vec{R}}{cR^2}\right]ds' \qquad (2.39)$$

$$\approx -\frac{1}{4\pi Rc}\int_{s}\hat{R}\times\frac{\partial\vec{J}(\vec{r}',\tau')}{\partial\tau'}ds'$$

Thus $\vec{h}^{s}$ can be explicitly written in terms of the incident field as

$$\vec{h}^{s}(\vec{r},t) = -\frac{1}{2\pi Rc}\hat{R}\times\int_{i}\hat{n}'\times\frac{\partial\vec{h}^{i}(\vec{r}',\tau)}{\partial t}ds' \qquad (2.40)$$

where $\int_{i}$ denotes an integral over the illuminated portion of the target.

The physical optics approximation allows the direct evaluation of $\vec{J}$ from a knowledge of the scatterer's geometry and orientation with respect to the incident wave. One of the short-comings of the PO approximations is its inability to accurately to represent the current near the shadow boundary.

CHAPTER 3

TIME-DOMAIN INVERSE SCATTERING IDENTITY

3.1   Introduction

Target imaging and identification using electromagnetic responses in the time and frequency domains has attracted increasing interest, with most methods carried out in the frequency domain. The use of time domain techniques was first discussed by Kennaugh and Cosgroff in 1957 [6]. Since then many researchers have developed approaches to the inverse scattering problem [7-12]. They have shown that the target impulse, step, and ramp responses are related to the target geometry based on physical optics principles. Under the physical optics approximation Bojarski has established a Fourier transform relationship between the geometry of the conducting scatterer and a form of the scattering cross section [14]. Since this approach is based on the physical optics approximation, it is valid only in the limit of high frequency. When the size of the scatterer is comparable to the incident pulsewidth, the physical optics solution is inadequate for this scattering problem. Furthermore, the impulse, step, or ramp response of the target is hard to obtain in practice.

In this chapter we start from the space-time magnetic field integral equation, and by using a Sine-Modulated Exponential Pulse (SMEP) waveform as the incident field, an exact two-dimensional time-domain bistatic inverse scattering identity can be obtained based on the inverse Radon transform. The formal definition of the Radon transform is

given in Section 3.2. In Section 3.3, the time-domain bistatic inverse scattering identity is derived in details. Special cases such as the monostatic case, rotationally symmetric target, flying object and three dimensional case are treated in Section 3.3.2, 3.3.3, 3.3.4, and 3.3.5, respectively.

3.2   The Radon Transform

Radon transform theory has become a very important mathematical operation and its applications are well known. They include computerized tomography (CT) applications in, for example, diagnostic medicine, radio astronomy, electron microscopy, optical interferometry, and geophysical exploration. These well-established concepts can be extended and applied to the radar inverse scattering problem.

3.2.1   Radon Transform in Several Dimensions

The Radon transform of a function at a given hyperplane is defined as the integral of the function over that hyperplane [11-13]. For a hyperplane in n-dimensional Euclidean space defined by

$$\hat{\xi} \cdot \vec{x} = p \tag{3.1}$$

where $\vec{x}$ is the spatial position vector, $\hat{\xi}$ is a unit vector orthogonal to the hyperplane, and p is the Euclidean distance from the origin, the Radon transform $F(\hat{\xi}, p)$ of a function $f(\vec{x})$ over the hyperplane is given by

$$F(\hat{\xi},p) = \int_{\xi \cdot \vec{x}=p} f(\vec{x})\,ds \qquad (3.2)$$

The above equation may be expressed more conveniently in the following form by using the Dirac delta function δ

$$F(\hat{\xi},p) = \int f(\vec{x})\,\delta(p - \hat{\xi}\cdot\vec{x})\,ds \qquad (3.3)$$

The inversion of the Radon transform consists of expressing $f(\vec{x})$ in terms of its integrals $F(\hat{\xi},p)$ over the hyperplanes. The inversion formula for odd dimension in n is

$$f(\vec{x}) = \frac{1}{2(2\pi j)^{n-1}}\int_{|\xi|=1} F_p^{(n-1)}(\hat{\xi},\hat{\xi}\cdot\vec{x})\,d\hat{\xi} \qquad (3.4)$$

where $F_p^{(n-1)}$ is the $(n-1)$th derivative of F with respect to p. For even n, the inversion formula is

$$f(\vec{x}) = \frac{1}{(2\pi j)^n}\int_{|\xi|=1} d\hat{\xi}\int_{-\infty}^{\infty} dp\,\frac{F_p^{(n-1)}(p,\hat{\xi})}{p-\hat{\xi}\cdot\vec{x}} \qquad (3.5)$$

Since the two-dimensional Radon transform has been used in this work, we will mainly discuss this case as an example which will also help understanding the Radon transform for higher dimensional cases.

3.2.2   Two Dimensions

We will use the coordinate system defined in Fig. 3.1 to describe line integrals. Let (x,y) designate coordinates of points in the plane, and consider some arbitrary function f defined on some domain D of 2-dimensional Euclidean space. If L is any line in the
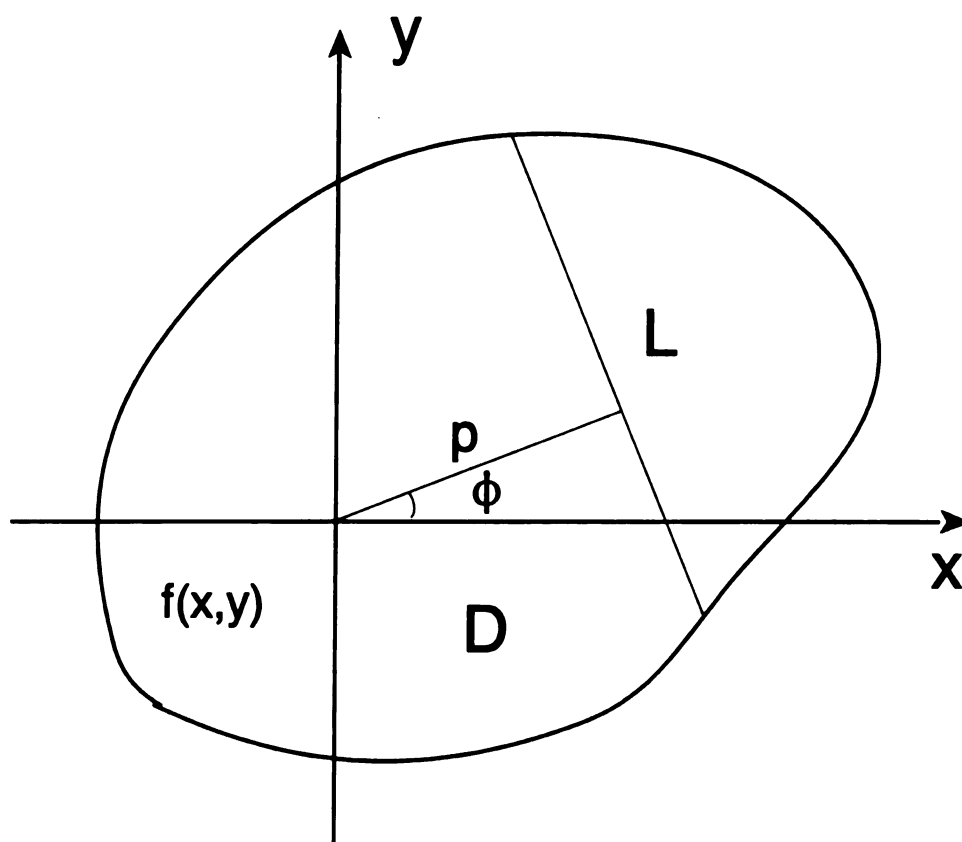
Figure 3.1   Geometry of 2-D Radon transform.

plane, then the line integral of f along all possible lines L is the two-dimensional Radon transform of f provided the integral exists. It can be written as

$$F = \int_L f(x,y)\, ds \tag{3.6}$$

where ds is an increment of length along L.

The equation of line L in Fig. 3.1 is

$$x\cos\phi + y\sin\phi = p \tag{3.7}$$

Then the transform can be written as an integral over two dimensional Euclidean space by using the delta function to select the line L from the space

$$F(p,\phi) = \int_{-\infty}^{\infty}\int_{-\infty}^{\infty} f(x,y)\delta(x\cos\phi + y\sin\phi - p)\, dx\, dy = \int f(\vec{x})\delta(p - \hat{\xi}\cdot\vec{x})\, d\vec{x} \tag{3.8}$$

where $\vec{x} = (x,y)$ and $\hat{\xi} = (\cos\phi,\ \sin\phi)$.

If $F(p,\phi)$ is known for all p and ϕ, then $F(p,\phi)$ is the two-dimensional Radon transform of $f(x,y)$. A projection is formed by combining a set of line integrals. The simplest projection is a collection of parallel integrals as is given by $F(p,\phi)$ for a fixed angle ϕ.

Since $\hat{\xi}\cdot\vec{x} = x\cos\phi + y\sin\phi$, the inverse Radon transform for the two-dimensional case $(n=2)$ can be written from (3.5) as

$$f(x,y) = -\frac{1}{4\pi^2}\int_0^\pi d\phi \int_{-\infty}^{\infty} \frac{\dfrac{\partial}{\partial p}F(p,\hat{\xi})}{p - \hat{\xi}\cdot\vec{x}}\, dp \tag{3.9}$$

If the replacements $x = r\cos\theta$, $y = r\sin\theta$ are made, then f in polar coordinates becomes

24

$$f(r,\theta) = -\frac{1}{4\pi^2}\int_0^\pi d\phi \int_{-\infty}^\infty \frac{\frac{\partial}{\partial p}F(p,\hat{\xi})}{p - r\cos(\phi - \theta)} dp \qquad (3.10)$$

These formulas for *n=2* constitute a solution to the problem of reconstruction from projections.

3.3 Derivation of Space-Time Integral Equations and Inverse Scattering Identity

When an electromagnetic field is incident upon an object, currents and charges are induced on and in the object. The induced currents and charges will then maintain a scattered electromagnetic field. Once the induced currents flowing on the conducting scatterer surface and the scatterer geometry are given, the scattered field can be calculated directly. The expression for the surface currents (MFIE) has been derived in chapter 2. In this Section, we will apply this expression to derive the inverse scattering identities for the monostatic and bistatic cases, respectively. Finally, we will also discuss the cases of the rotationally symmetric object, flying radar targets, and the 3-D case.

3.3.1 The Bistatic Case

From chapter 2 we know that the expression for the induced surface current $\vec{J}$ at the point $\vec{r}$ on the scatterer surface and at the time t can be written as

$$\vec{J}(\vec{r},t) = \begin{cases} 2\hat{n} \times \vec{h}^i(\vec{r},t) + \vec{J}_c(\vec{r},t) & \hat{n}\cdot\hat{q} > 0 \\ \vec{J}_c(\vec{r},t) & \hat{n}\cdot\hat{q} < 0 \end{cases} \qquad (3.11)$$

where

25

$$\vec{J}_c(\vec{r},t) = \frac{1}{2\pi}\int_s \hat{n}\times\left\{\left[\frac{1}{R^2}+\frac{1}{R}\frac{\partial}{\partial\tau}\right]\vec{J}(\vec{r}',\tau)\times\hat{a}_R\right\}ds \qquad (3.12)$$

where $\vec{h}^i(\vec{r},t)$ is the incident magnetic field, $\hat{n}$ is the unit vector normal to the scatterer surface, $\vec{r}$ is the position vector to the observation point, $\vec{r}'$ is the position vector to the integration point, $R = |\vec{r}-\vec{r}'|$, $\hat{a}_R = (\vec{r}-\vec{r}')/R$, $\hat{q}$ is the unit vector to the transmitting antenna, $\tau=t-R$, and t denotes normalized time in meters (ct).

From equation (3.11), we can see that the first term of the right-hand side represents the direct influence of the incident field on the current at the observation point. When applied to the illuminated side of the scatterer, it yields the familiar physical optics approximation for the surface current. The second term on the right-hand side of (3.11) represents the influence of currents at other surface points on the current at the observation point.

Once the surface current density has been obtained, the far scattered field of the scatterer shown in Figure 3.2 can be calculated by the expression

$$\vec{h}^s(\vec{r}_s,t) = \frac{1}{4\pi}\left[\nabla\times\int_s \frac{\vec{J}(\vec{r}',\tau')}{R_s}ds'\right] \qquad (3.13)$$

where $R_s = |\vec{r}_s-\vec{r}'|$, and $\tau' = t-R_s$

Assuming that the observation point $\vec{r}_s$ is not on S, the curl operator may be carried inside the integral. Using the far-field approximations and standard vector identities, we have
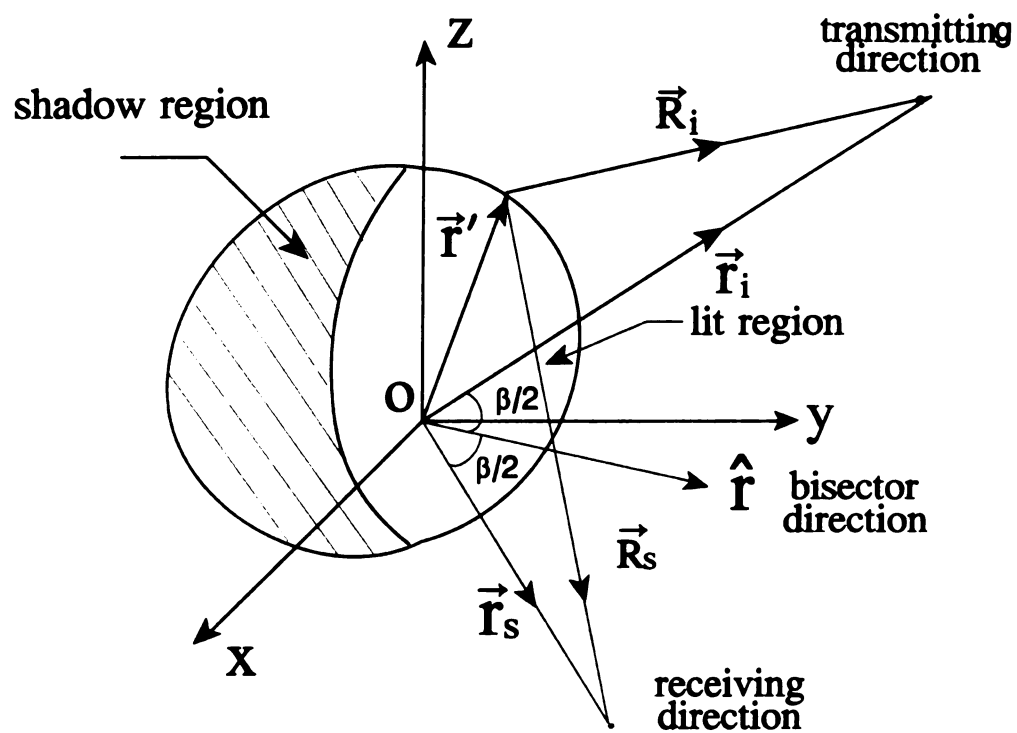
Figure 3.2   Geometry of the scatterer and graphic view of space parameters.

$$\vec{h}^s(\vec{r}_s,t) \approx -\frac{1}{4\pi R_s}\int_s \hat{R}_s \times \frac{\partial \vec{J}(\vec{r}',\tau')}{\partial \tau'}ds' \qquad (3.14)$$

where $\hat{R}_s = (\vec{r}_s - \vec{r}')/|\vec{r}_s - \vec{r}'|$

In the far zone, we can use the approximations $R_s \approx r_s - \hat{r}_s \cdot \vec{r}'$ for the retarded time

τ' and $R_s \approx r_s$ and $\hat{R}_s \approx \hat{r}_s$ for the amplitude term. Then (3.14) becomes

$$\vec{h}^s(\vec{r}_s,t) = -\frac{1}{4\pi r_s}\int_s \hat{r}_s \times \frac{\partial \vec{J}(\vec{r}',\tau')}{\partial \tau'}ds' \qquad (3.15)$$

Now, we define the aperture function

$$A(\hat{r}_i,\hat{n}) = \begin{cases} 1 & \hat{r}_i \cdot \hat{n}(\vec{r}') > 0 \\ 0 & \hat{r}_i \cdot \hat{n}(\vec{r}') < 0 \end{cases} \qquad (3.16)$$

which is unity on the illuminated region of scatterer surface, and zero in the shadow

region. Substituting (3.11) into (3.15), we have

$$\vec{h}^s(\vec{r}_s,t) = -\frac{1}{2\pi r_s}\int_s \hat{r}_s \times \hat{n}' \times \frac{\partial \vec{h}^i(\vec{r}',\tau)}{\partial \tau}A(\hat{r}_i,\hat{n})ds' - \frac{1}{4\pi r_s}\int_s \hat{r}_s \times \frac{\partial \vec{J}_c(\vec{r}',\tau')}{\partial \tau'}ds' \qquad (3.17)$$

where $\tau = t - R_i - R_s \approx t - r_i - r_s + (\hat{r}_i + \hat{r}_s)\cdot\vec{r}'$, and $\tau' = t - R_s \approx t - r_s + \hat{r}_s \cdot \vec{r}'$. Using the vector

identity $\hat{r}_s \times (\hat{n}' \times \hat{h}^i) = \hat{n}'(\hat{r}_s \cdot \hat{h}^i) - \hat{h}^i(\hat{r}_s \cdot \hat{n}')$, (3.17) can be written as

$$h^s(\vec{r}_s,t) = \frac{1}{2\pi r_s}\int_s \hat{n}' \cdot \vec{K}\frac{\partial h^i(\vec{r}',\tau)}{\partial \tau}A(\hat{r}_i,\hat{n})ds' - \frac{1}{4\pi r_s}\left[\int_s \hat{r}_s \times \frac{\partial \vec{J}_c(\vec{r}',\tau')}{\partial \tau'}ds'\right]\cdot\hat{h}^i \qquad (3.18)$$

where $\vec{K} = \hat{r}_s - (\hat{r}_s \cdot \hat{h}^i)\hat{h}^i$, and $h^s(\vec{r}_s,t) = \hat{h}^i \cdot \vec{h}^s(\vec{r}_s,t)$. Now, letting the same incident pulse

28

illuminate the shadow region of the scatterer, we have

$$h_2^s(\vec{r}_s,t) = \frac{1}{2\pi r_s}\int_s \hat{n}'\cdot\vec{K}\frac{\partial h^i(\vec{r}',\tau)}{\partial\tau}A_2(\hat{r}_i,\hat{n})ds' - \frac{1}{4\pi r_s}\left[\int_s \hat{r}_s\times\frac{\partial\vec{J}_{c2}(\vec{r}',\tau')}{\partial\tau'}ds'\right]\cdot\hat{h}^i \quad (3.19)$$

Combining (3.18) and (3.19) yields

$$\frac{1}{2\pi r_s}\int_s \hat{n}'\cdot\vec{K}\frac{\partial h^i(\vec{r}',\tau)}{\partial\tau}ds' = H^s(\vec{r}_s,t) \quad (3.20)$$

where

$$h_{c1}^s(\vec{r}_s,t) = \frac{1}{4\pi r_s}\left[\int_s \hat{r}_s\times\frac{\partial\vec{J}_c(\vec{r}',\tau')}{\partial\tau'}ds'\right]\cdot\hat{h}^i$$

$$h_{c2}^s(\vec{r}_s,t) = \frac{1}{4\pi r_s}\left[\int_s \hat{r}_s\times\frac{\partial\vec{J}_{c2}(\vec{r}',\tau')}{\partial\tau'}ds'\right]\cdot\hat{h}^i \quad (3.21)$$

$$H^s(\vec{r}_s,t) = h^s(\vec{r}_s,t)+h_2^s(\vec{r}_s,t)+h_{c1}^s(\vec{r}_s,t)+h_{c2}^s(\vec{r}_s,t)$$

Applying Gauss' law to the left hand side of (3.20), we have

$$\int_v \frac{\partial^2 h^i(\vec{r}',\tau)}{\partial\tau^2}dv' = \frac{\pi r_s}{(\vec{K}\cdot\hat{r})\cos(\beta/2)}H^s(\vec{r}_s,t) \quad (3.22)$$

where $\hat{r}_i+\hat{r}_s = 2\cos\frac{\beta}{2}\hat{r}$, and β is the bistatic angle as shown in Fig. 3.2. Assuming the

incident magnetic field is a SMEP defined by

$$h^i(t) = \sin(\omega_c t)e^{-\alpha t}U(t) \quad (3.23)$$

where $U(t) = \begin{cases} 1 & t>0 \\ 0 & t<0 \end{cases}$, we have

29

$$\frac{dh^i(t)}{dt} = [\omega_c\cos(\omega_c t) - \alpha\sin(\omega_c t)]e^{-\alpha t}U(t) \qquad (3.24)$$

and

$$\frac{d^2h^i(t)}{dt^2} = \left[(\alpha^2 - \omega_c^2)\sin(\omega_c t) - 2\alpha\omega_c\cos(\omega_c t)\right]e^{-\alpha t}U(t) + \omega_c\delta(t) \qquad (3.25)$$

Using the relation $\tau = t - R_i - R_s$, the left hand side of (3.22) can be written as

$$\int_V \frac{\partial^2 h^i(\vec{r}',\tau)}{\partial\tau^2}dv' = \frac{\partial}{\partial t}\int_V \frac{\partial h^i(\vec{r}',\tau)}{\partial\tau}dv' = \frac{\partial^2}{\partial t^2}\int_V h^i(\vec{r}',\tau)dv' \qquad (3.26)$$

Then, using (3.22) and (3.26) together with (3.23) and (3.24), we can obtain the two equations

$$\int_V \sin(\omega_c\tau)e^{-\alpha\tau}U(\tau)dv' = \frac{\pi r_s}{(\vec{K}\cdot\vec{r})\cos(\beta/2)}\int_0^t\int_0^t H^s(\vec{r}_s,t)dt^2 \qquad (3.27)$$

and

$$\int_V \omega_c\cos(\omega_c\tau)e^{-\alpha\tau}U(\tau)dv' = \frac{\pi r_s}{(\vec{K}\cdot\vec{r})\cos(\beta/2)}\left[\int_0^t H^s(\vec{r}_s,t)dt + \alpha\int_0^t\int_0^t H^s(\vec{r}_s,t)dt^2\right] \qquad (3.28)$$

Substituting (3.25) into (3.22) and using (3.27) and (3.28), we have

$$\int_V \delta(\tau)dv' = \frac{\pi r_s}{(\vec{K}\cdot\vec{r})\cos(\beta/2)\omega_c}\left[H^s(\vec{r}_s,t) + 2\alpha\int_0^t H^s(\vec{r}_s,t)dt \right.$$
$$\left. + (\omega_c^2 + \alpha^2)\int_0^t\int_0^t H^s(\vec{r}_s,t)dt^2\right] \qquad (3.29)$$

Now, defining the characteristic function

$$\gamma(\vec{r}') = \begin{cases} 1 & \vec{r}' \in V \\ 0 & \vec{r}' \notin V \end{cases} \tag{3.30}$$

we have

$$\int\int\int_{-\infty}^{\infty} \gamma(\vec{r}')\delta(t_s - \hat{r}\cdot\vec{r}')dv' = \frac{2\pi r_s}{\vec{K}\cdot\hat{r}\omega_c}\left[H^s(\vec{r}_s,t) + 2\alpha\int_0^t H^s(\vec{r}_s,t)dt \right.$$
$$\left. + (\omega_c^2 + \alpha^2)\int_0^t\int_0^t H^s(\vec{r}_s,t)dt^2\right] \tag{3.31}$$

where we use the relation $\tau = t - R_i - R_s$ and the properties of the Delta function

$$\delta(\tau) = \delta(-\tau)$$
$$\delta(2\cos\frac{\beta}{2}\tau) = \frac{1}{2\cos(\beta/2)}\delta(\tau) \tag{3.32}$$

and $t_s = \dfrac{r_i + r_s - t}{2\cos(\beta/2)}$.

It can be see from equation (3.31) and Fig. 3.3 that the right hand side of (3.31) is the Radon transform of $\gamma(\vec{r}')$ (see Section 3.2). It denotes the projected area function at the plane $t_s = \hat{r}\cdot\vec{r}'$

$$A(\hat{r},t_s) = \int\int\int_{-\infty}^{\infty} \gamma(\vec{r}')\delta(t_s - \hat{r}\cdot\vec{r}')dv' \tag{3.33}$$

Here $A(\hat{r},t_s)$ is the projected area onto t_s for the particular aspect direction $\hat{r}$ along t_s.

Note that the cross sectional area $A(\hat{r},t_s)$ is formed with a time scale such that the cutting plane $t_s = \hat{r}\cdot\vec{r}'$ used to determine $A(\hat{r},t_s)$ moves with $1/(2\cos(\beta/2))$ (one half for the monostatic case) of the velocity of the incident SMEP.

31

If the view angles are available only in the $x-y$ plane ($\theta' = \pi/2$, $0 \le \phi^i \le 2\pi$), then the body geometry can be related to the cross-sectional areas $A(\hat{r},t_s)$ through

$$A(\hat{r},t_s) = \int\int\int_{-\infty}^{\infty} \gamma(x',y',z')\delta(t_s-(x'\cos\phi^i+y'\sin\phi^i))dx'dy'dz' \tag{3.34}$$

Integrating with respect to z', (3.34) becomes

$$A(\hat{r},t_s) = \int\int_{-\infty}^{\infty} \Gamma(x',y')\delta(t_s-(x'\cos\phi^i+y'\sin\phi^i))dx'dy' \tag{3.35}$$

where $\Gamma(x,y) = \int_{-\infty}^{\infty}\gamma(x,y,z)dz$ is the "thickness function" of the target in the z direction.

Taking the two-dimensional inverse Radon transform of equation (3.35) (see Section 3.2.2 equation (3.10)), we can get the thickness function [11-13].

$$\Gamma(\bar{\rho}') = -\frac{1}{4\pi^2}\int_0^{2\pi}\int_{-\infty}^{\infty}\frac{\partial A(\hat{r},t_s)}{\partial t_s}\frac{dt_s d\phi}{t_s-\rho'\cos(\phi'-\phi)}$$

$$= -\frac{1}{2\pi^2}\int_0^{\pi}\int_{-\infty}^{\infty}\frac{A(\hat{r},t_s)}{(t_s-\rho'\cos(\phi'-\phi))^2}dt_s d\phi \tag{3.36}$$

$$= -\frac{1}{\pi^2}\int_0^{\pi}\int_{-\infty}^{\infty}\frac{\cos(\beta/2)A(\hat{r},t_s)}{(t-\rho_{is}+2\rho'\cos(\beta/2)\cos(\phi'-\phi))^2}dt d\phi$$

where $\bar{\rho}' = x'\hat{x}+y'\hat{y} = \rho'\cos\phi'\hat{x}+\rho'\sin\phi'\hat{y}$, and $\rho_{is} = \rho_i+\rho_s$. Substituting (3.31) into (3.36), we have

$$\Gamma(\bar{\rho}')=-\frac{2\rho_s\cos(\beta/2)}{(\bar{K}\cdot\hat{\rho})\pi\omega_c}\int_0^{\pi}\int_{-\infty}^{\infty}\frac{H^s(\bar{\rho}'_s,t)+2\alpha\int_0^t H^s(\bar{\rho}'_s,t)dt+(\omega_c^2+\alpha^2)\int_0^t\int_0^t H^s(\bar{\rho}'_s,t)dt^2}{[t-\rho_{is}+2\rho'\cos(\beta/2)\cos(\phi'-\phi)]^2}dt d\phi \tag{3.37}$$

From equation (3.37), we know ϕ depends on ϕ^i, ϕ^s and β. Here we only

32
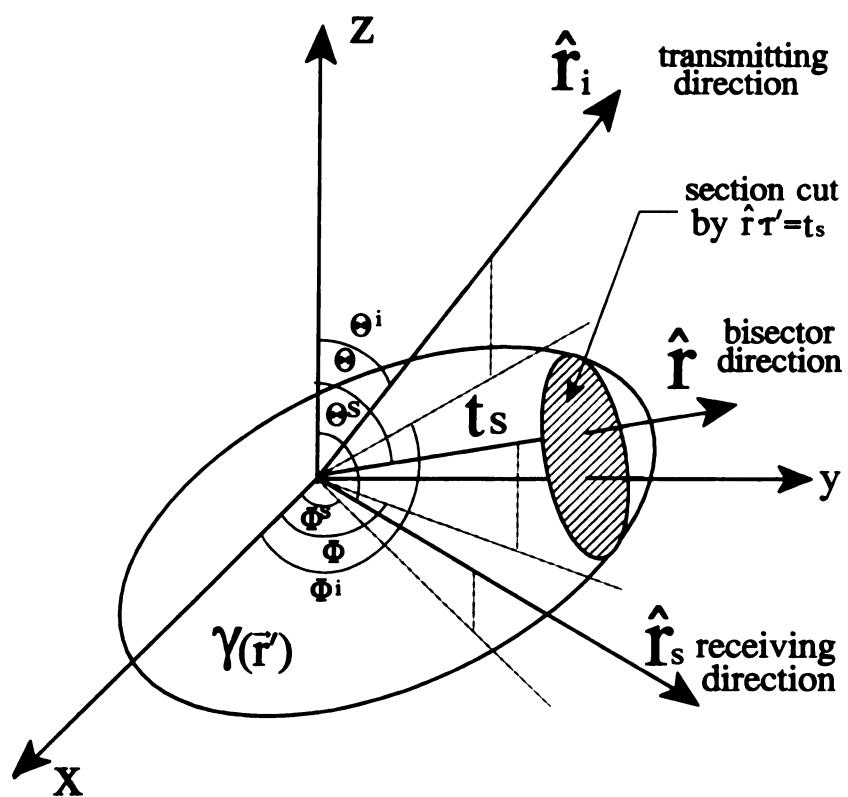
Figure 3.3 Geometry of 3-D body reconstruction problem

33

consider the special case when both transmitting and receiving antennas are fixed and the

target rotating or the scatterer is static and the transmitting and receiving antennas are

moving around the scatterer with bistatic angle $\phi^i - \phi^s = $ constant β. Then $\phi = \phi^i - \beta/2$ (see

Figure 3.2 and Figure 3.3), we have

$$\Gamma(\bar{\rho}') = -\frac{2\rho_s\cos(\beta/2)}{(\vec{K}\cdot\hat{\rho})\pi\omega_c}\int_{\beta/2}^{\pi+\beta/2}\int_{-\infty}^{\infty}\frac{H^s(\bar{\rho}_s',t)+2\alpha\int_0^t H^s(\bar{\rho}_s',t)dt + (\omega_c^2+\alpha^2)\int_0^t\int_0^t H^s(\bar{\rho}_s',t)dt^2}{[t-\rho_{is}+2\rho'\cos(\beta/2)\cos(\phi'-\phi^i+\beta/2)]^2}dt\,d\phi^i$$
(3.38)

$$= -\frac{2\rho_s\cos(\beta/2)}{(\vec{K}\cdot\hat{\rho})\pi\omega_c}\int_0^\pi\int_{-\infty}^{\infty}\frac{H^s(\bar{\rho}_s',t)+2\alpha\int_0^t H^s(\bar{\rho}_s',t)dt+(\omega_c^2+\alpha^2)\int_0^t\int_0^t H^s(\bar{\rho}_s',t)dt^2}{[t-\rho_{is}+2\rho'\cos(\beta/2)\cos(\phi'-\phi^i+\beta/2)]^2}dt\,d\phi^i$$

This is the complete solution to the two-dimensional bistatic problem of recovering

a body from its scattered field; it needs the reflected fields and the correction term from

all possible directions in the x-y plane. The next step is to solve equation (3.38). We can

use an iterative method to get the 2-dimensional target geometry [9]. First, neglect the

correction terms $h_{c1}^s(\bar{\rho}',t)$ and $h_{c2}^s(\bar{\rho}',t)$ in equation (3.38). This is the time domain

physical optics inverse problem. We can thus obtain an initial estimate of $\Gamma_1(\bar{\rho})$, and the

correction terms, $h_{c1}^s(\bar{\rho}',t)$ and $h_{c2}^s(\bar{\rho}',t)$, in (3.38) can be obtained by solving

$\vec{J}_c(\vec{r},t)$, $\vec{J}_{c2}(\vec{r},t)$ in (11) using the marching on in time method, and then used in (3.21).

Then the correction terms can be used in (3.38) to obtain a new estimate of $\Gamma_2(\bar{\rho})$. Then $\Gamma_1(\bar{\rho})$

and $\Gamma_2(\bar{\rho})$ can be compared to see if the change is less than some small number, and the

procedure continued until this convergence criterion is satisfied. The numerical results for

a sphere of 14 inch radius using those procedures will be shown in Chapter 4.

Note that from (3.22) we can see that when the incident magnetic field is a ramp,

using the physical optics approximation by dropping the correction terms, and using

$\beta=0, \vec{K} \cdot \hat{r}=1$ for the monostatic case, then the backscattered ramp response is proportional

to the cross-sectional area of the target as a function of the distance along the line of the

incident direction [15]. This is the same result which Kennaugh, Cosgriff, and Moffatt had

obtained [6], [7]. Das and Boerner [12] have shown that the size and shape of an object

can be obtained from its area functions, and the problem can be reduced to the classical

Radon problem.

3.3.2 The Monostatic Case

For the monostatic case, the same procedure could be used to derived the inverse

scattering identity as described in Section 3.3.1. We could also use our formulas (3.37)

just obtained for the monostatic identity if we let the bistatic angle $\beta = 0$, then

$$\cos(\beta/2) = 0$$

$$\hat{\rho}_s = \hat{\rho}$$

$$\rho_{is} = 2\rho$$

(3.39)

$$\vec{K} \cdot \hat{\rho} = \left[\hat{\rho} - (\hat{\rho} \cdot \hat{h}^i)\hat{h}^i \right] \cdot \hat{\rho} = 1$$

Applying (3.39), (3.37) becomes

$$\Gamma(\bar{\rho}') = -\frac{2\rho}{\pi \omega_c} \int_0^\pi \int_{-\infty}^\infty \frac{H^s(\bar{\rho}'_s,t) + 2\alpha \int_0^t H^s(\bar{\rho}'_s,t)dt + (\omega_c^2 + \alpha^2)\int_0^t \int_0^t H^s(\bar{\rho}'_s,t)dt^2}{[t - 2\rho + 2\rho'\cos(\phi' - \phi^i)]^2} dt\, d\phi^i \quad (3.40)$$

Comparing Figure 3.3 and 3.4 will help understanding this identity.
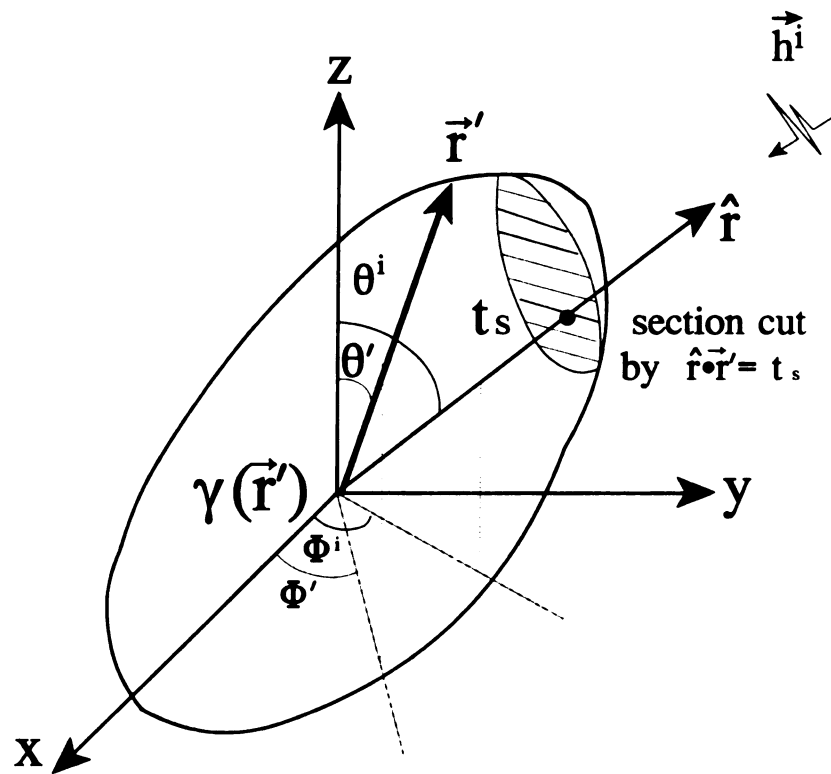
Figure 3.4. Geometry of 3-D monostatic body reconstruction problem.

3.3.3 Rotational Symmetric Targets

If the scatterer as shown in fig. 3.4 is a rotationally symmetric target about the z-axis, then it is the simplest case to reconstruct the body shape of the scatterer, because the contour of a rotationally symmetric object can be completely described by the radius ρ which varies as a function of z, and its projected area function can be expressed as

$$A = \pi \rho^2(z) \qquad (3.41)$$

where $\rho(z)$ is the radius of the scatterer along z axis. Substituting the projected area function into (3.31) yields the inversion equation for the rotationally symmetric case

$$\rho(z) = \left\{ \frac{2r_s}{\omega_c(\vec{K}\cdot\hat{r})}\left[H^s(\vec{r}_s,t) + 2\alpha\int_0^t H^s(\vec{r}_s,t)dt + (\omega_c^2+\alpha^2)\int_0^t\int_0^t H^s(\vec{r}_s,t)dt^2 \right] \right\}^{\frac{1}{2}} \qquad (3.42)$$

This expression needs the reflected field for only two incident directions to reconstruct the rotational body, and we can use the iterative approach or the direct "marching on in time" approach to solve (3.42). If the upper part and the lower part of the scatterer is also symmetric, we can simplify (3.42) as

$$\rho(z) = \left\{ \frac{2r_s}{\omega_c(\vec{K}\cdot\hat{r})}\left[H_1^s(\vec{r}_s,t) + 2\alpha\int_0^t H_1^s(\vec{r}_s,t)dt + (\omega_c^2+\alpha^2)\int_0^t\int_0^t H_1^s(\vec{r}_s,t)dt^2 \right] \right\}^{\frac{1}{2}} \qquad (3.43)$$

where $H_1^s(\vec{r}_s,t) = h^s(\vec{r}_s,t) + h_{cl}^s(\vec{r}_s,t)$. If we use PO approximations and neglect the correction terms, then (3.43) becomes

$$\rho(z) = \left\{ \frac{2r_s}{\omega_c(\vec{K}\cdot\hat{r})}\left[h^s(\vec{r}_s,t) + 2\alpha\int_0^t h^s(\vec{r}_s,t)dt + (\omega_c^2+\alpha^2)\int_0^t\int_0^t h^s(\vec{r}_s,t)dt^2 \right] \right\}^{\frac{1}{2}} \qquad (3.44)$$
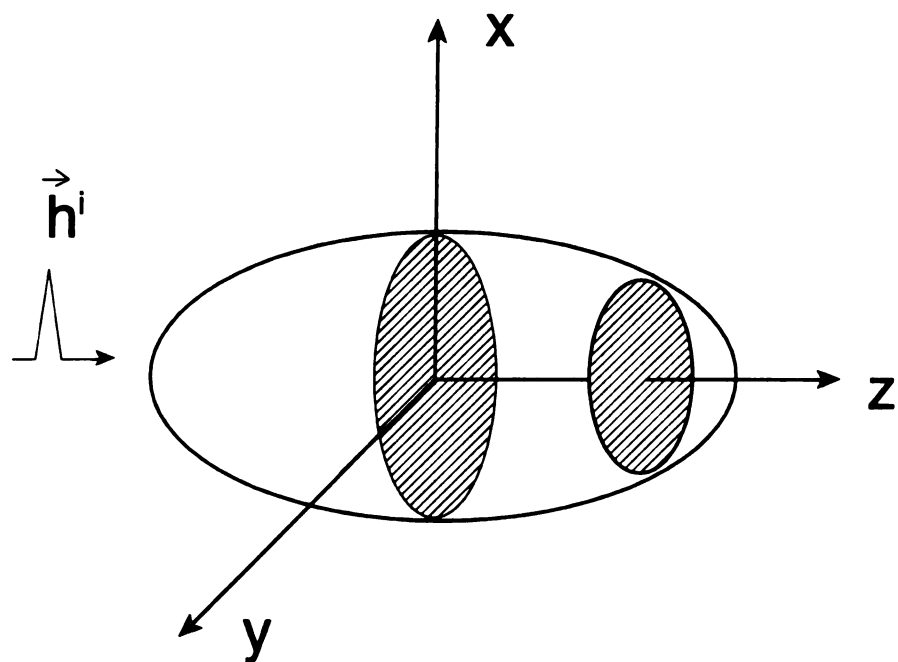
Figure 3.5 Geometry of rotationally symmetric scattering problem

3.3.4 Flying Radar Targets

In this special case, we assume that the upper part of the flying object is symmetric to the lower part of the object such that only the reflected fields from the lower part of the object are needed to recover the shape of the scatterer [52]. Also note that the bistatic angle β and the distance between the scatterer and the transmitting and receiving antennas change with the movement of the flying object. In order to simplify the problem, we assume that the flying object has constant altitude h, and the distance between the two antennas is a constant d. When the target flies forward, it is equivalent to letting the antennas move backwards at the same velocity of the target while keeping the target static. The geometry of the scatterer is shown in figure 3.6. The following relations can be found from the figure

$$r_i = \sqrt{h^2 + (h\cot\phi + \frac{d}{2})^2} \tag{3.45}$$

$$r_s = \sqrt{h^2 + (h\cot\phi - \frac{d}{2})^2} \tag{3.46}$$

$$r = \sqrt{h^2 + (h\cot\phi)^2} \tag{3.47}$$

$$\sin\phi^s = \frac{r}{r_s}\sin\phi = \frac{1}{\sqrt{1 + (\cot\phi - \frac{d}{2h})^2}} \tag{3.48}$$
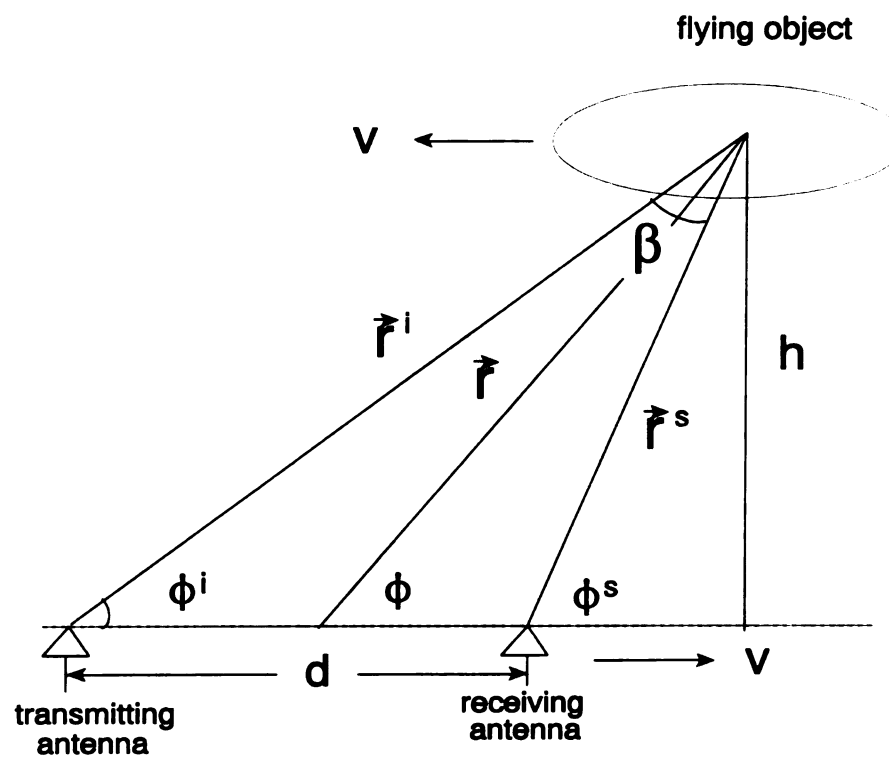
Figure 3.6   Geometry of the flying object

$$\frac{\beta}{2} = \arcsin\frac{1}{\sqrt{1+(\cot\phi-\dfrac{d}{2h})^2}} - \phi \qquad (3.49)$$

$$\cos\frac{\beta}{2} = \cos\left[\arcsin\frac{1}{\sqrt{1+(\cot\phi-\dfrac{d}{2h})^2}} - \phi\right]$$

$$= \cos\left[\arcsin\frac{1}{\sqrt{1+(\cot\phi-\dfrac{d}{2h})^2}}\right]\cos\phi + \frac{\sin\phi}{\sqrt{1+(\cot\phi-\dfrac{d}{2h})^2}}$$

$$\qquad (3.50)$$

$$= \sqrt{1-\frac{1}{1+(\cot\phi-\dfrac{d}{2h})^2}}\cos\phi + \frac{\sin\phi}{\sqrt{1+(\cot\phi-\dfrac{d}{2h})^2}}$$

$$= \frac{1-\dfrac{d}{4h}\sin2\phi}{\sin\phi\sqrt{1+(\cot\phi-\dfrac{d}{2h})^2}}$$

Since the bistatic angle is changes with the movement of the flying object, the related terms should be inside the integral in the expression of the thickness function. The thickness function can be written as

$$\Gamma(\vec{\rho}') = -\frac{2}{\pi\omega_c}\int_0^\pi\int_{-\infty}^\infty \frac{r_s\cos(\beta/2)\left[H^s(\vec{r}_s',t)+2\alpha\int_0^t H^s(\vec{r}_s',t)dt + (\omega_c^2+\alpha^2)\int_0^t\int_0^t H^s(\vec{r}_s',t)dt^2\right]}{\vec{K}\cdot\hat{r}\left[t-r_i-r_s+2r'\cos(\beta/2)\cos(\phi'-\phi)\right]^2}dt\,d\phi$$

$$= -\frac{2}{\pi\omega_c}\int_0^\pi\int_{-\infty}^\infty \frac{r_s\cos(\beta/2)\bar{H}(\vec{r}',t)}{\vec{K}\cdot\hat{r}\left[t-r_i-r_s+2r'\cos(\beta/2)\cos(\phi'-\phi)\right]^2}dt\,d\phi$$

$$\qquad (3.51)$$

where

$$\bar{H}(\vec{r}',t) = H^s(\vec{r}'_s,t) + 2\alpha \int_0^t H^s(\vec{r}'_s,t)dt + (\omega_c^2 + \alpha^2)\int_0^t \int_0^t H^s(\vec{r}'_s,t)dt^2 \tag{3.52}$$

Then, substituting (3.45), (3.46) and (3.50) into (3.51) yields

$$\Gamma(\vec{r}') = \frac{-2}{\pi \omega_c} \int_0^\pi \int_{-\infty}^\infty \frac{(h - \frac{d}{4}\sin2\phi)\bar{H}(\vec{r}',t)\sqrt{1 + (\cot\phi - \frac{d}{2h})^2} \; dt \, d\phi}{\vec{K}\cdot\vec{r}\left[(t - r_{is})\sin\phi\sqrt{1 + (\cot\phi - \frac{d}{2h})^2} + 2r'(1 - \frac{d}{4h}\sin2\phi)\cos(\phi' - \phi)\right]^2} \tag{3.53}$$

where

$$r_{is} = h\sqrt{1 + (\cot\phi + \frac{d}{2h})^2} + h\sqrt{1 + (\cot\phi - \frac{d}{2h})^2} \tag{3.54}$$

The time-domain identity (3.54) can also be used to construct an image from short pulse radar measurements.

3.3.5 Three Dimensional Case

Assuming the incident magnetic field is a Half Gaussian Modulated Sine (HGMS)

$$h(t) = \sin(\omega_c t)e^{-\pi(\frac{t}{a})^2} U(t) = \sin(\omega_c t)e^{-\alpha t^2}U(t) \tag{3.55}$$

where a is the shape factor, $\alpha = \pi/a^2$. the second time differential of $h(t)$ is

$$\frac{d^2 h(t)}{dt^2} = \left[(4\alpha^2 t^2 - \omega_c^2 - 2\alpha)\sin\omega_c t - 4\alpha\omega_c t \cos\omega_c t\right]e^{-\alpha t^2}U(t) + \omega_c\delta(t) \tag{3.56}$$

substituting (3.56) into (3.22) gives

$$\int_V \left\{ \left[(4\alpha^2\tau^2 - \omega_c^2 - 2\alpha) \sin\omega_c\tau - 4\alpha\omega_c\tau \cos\omega_c\tau \right] e^{-\alpha\tau^2} U(\tau) \right.$$

$$\left. + \omega_c\delta(\tau) \right\} dv' = \frac{\pi r_s}{(\vec{K}\cdot\hat{r})\cos(\beta/2)} H^s(\vec{r}_s,t) \tag{3.57}$$

Using the characteristic function and the properties of the Delta function equation (3,57) can be written as

$$\iiint_{-\infty}^{\infty} \gamma(\vec{r}')\delta(t_s - \hat{r}\cdot\vec{r}') dv' = \frac{2\pi r_s}{(\vec{K}\cdot\hat{r})\cos(\beta/2)\,\omega_c} H^s(r_s,t) -$$

$$\frac{2}{\omega_c}\int_V [(4\alpha^2\tau^2 - \omega_c^2 - 2\alpha)\sin\omega_c\tau - 4\alpha\omega_c\tau\cos\omega_c\tau] e^{-\alpha\tau^2} U(\tau) dv' \tag{3.58}$$

where $t_s = r - t/2$.

It can be seen from equation (3.33) and Fig. 3.3 that the right hand side of (3.58) is the Radon transform of $\gamma(\vec{r}')$. It denotes the projected area function at the plane $t_s = \hat{r}\cdot\vec{r}'$. In polar coordinate system, (3.33) can be written as

$$A(\hat{r},t_s) = \int_0^\infty \int_0^{2\pi} \int_{-\pi/2}^{\pi/2} \gamma(r',\theta',\phi') \delta(t_s - r'[\sin\theta'\sin\theta^i\cos(\phi'-\phi^i) + \cos\theta'\cos\theta^i]) r'^2\sin\theta' d\theta' d\phi' dr \tag{3.59}$$

If the cross-section areas $A(\hat{r},t_s)$ are given for all directions (θ^i,ϕ^i) and for all t_s, then taking the 3-D inverse Radon transform of (3.59), we can obtain the body shape function

43

$$\gamma(r',\theta',\phi') = -\frac{1}{8\pi^2}\int_0^{2\pi}\int_{-\pi/2}^{\pi/2}\frac{\partial^2 A(\hat{r},t_s)}{\partial^2 t_s}\bigg|_{t_s=\hat{r}\cdot\vec{r}'}\sin\theta^i d\theta^i d\phi^i \qquad (3.60)$$

where $t_s = \hat{r}\cdot\vec{r}' = r'[\sin\theta'\sin\theta^i\cos(\phi'-\phi^i)+\cos\theta'\cos\theta^i]$. From (3.58) we have

$$A(\hat{r},\,t_s) = \frac{2\pi r_s}{(\vec{K}\cdot\hat{r})\cos(\beta/2)\omega_c}H^s(\vec{r},t)$$

$$-\int_V\frac{2}{\omega_c}\Big[(4\alpha^2\tau^2-\omega_c^2-2\alpha)\sin\omega_c\tau-4\alpha\omega_c\tau\cos\omega_c\tau\Big]e^{-\alpha\tau^2}U(\tau)dv' \qquad (3.61)$$

Since $\tau = t-2r+2\hat{r}\cdot\vec{r}' = -2t_s+2\hat{r}\cdot\vec{r}'$, and $d\tau = dt = -2dt_s$, the second differential of

$A(\hat{r},t_s)$ with respect to t_s is

$$\frac{\partial^2 A(\hat{r},\,t_s)}{\partial^2 t_s^2}\bigg|_{t_s=\hat{r}\cdot\vec{r}'} = \Bigg\{\frac{8\pi r_s}{(\vec{K}\cdot\hat{r})\cos(\beta/2)\omega_c}\frac{\partial^2}{\partial^2 t}H^s(\vec{r},t)$$

$$-\int_V\frac{8}{\omega_c}\big[(\;\cdots\;)\sin\omega_c\tau+\tau(\;\cdots\;)\cos\omega_c\tau\big]e^{-\alpha\tau^2}U(\tau)dv'$$

$$+8(\omega_c^2+6\alpha)\int\int_{-\infty}^{\infty}\!\!\!\int\gamma(\vec{r}')\delta(t_s-\hat{r}\cdot\vec{r}_s)dv'\Bigg\}\Bigg|_{t_s=\hat{r}\cdot\vec{r}'} \qquad (3.62)$$

$$= \Bigg\{\frac{8\pi r_s}{(\vec{K}\cdot\hat{r})\cos(\beta/2)\omega_c}\frac{\partial^2}{\partial^2 t}H^s(\vec{r},t)+8(\omega_c^2+6\alpha)A(\hat{r},t_s)\Bigg\}\Bigg|_{t_s=\hat{r}\cdot\vec{r}'}$$

Substituting (3.62) into (3.60) gives

$$\gamma(r',\theta',\phi') = \int_0^{2\pi}\int_{-\frac{\pi}{2}}^{\frac{\pi}{2}}\Bigg\{\frac{-r_s}{\pi\omega_c(\vec{K}\cdot\hat{r})\cos(\beta/2)}\frac{\partial^2}{\partial t^2}H^s(\vec{r},t)-\frac{1}{\pi^2}(\omega_c^2+6\alpha)A(\hat{r},t_s)\Bigg\}\Bigg|_{t_s=\hat{r}\cdot\vec{r}'}\sin\theta^i d\theta^i d\phi^i$$

$$(3.63)$$

44

From (3.61), we have

$$A(\hat{r},\ t_s)\big|_{t_s=\hat{r}\cdot\vec{r}'} = \frac{2\pi r_s}{(\vec{K}\cdot\hat{r})\cos(\beta/2)\omega_c} H^s(\vec{r},t)\big|_{t=2r-2\hat{r}\cdot\vec{r}'} \tag{3.64}$$

Substituting (3.64) into (3.63) gives

$$\gamma(r',\theta',\phi') = \frac{-r_s}{(\vec{K}\cdot\hat{r})\cos(\beta/2)\pi\omega_c} \int_0^{2\pi}\int_{-\pi/2}^{\pi/2} \left\{\frac{\partial^2}{\partial t^2}+2(\omega_c^2+6\alpha)\right\} H^s(\vec{r}_s,t)\sin\theta^i d\theta^i d\phi^i \tag{3.65}$$

$$= \frac{-2r_s}{\vec{K}\cdot\hat{r})\cos(\beta/2)\pi\omega_c} \int_0^{2\pi}\int_{-\pi/2}^{\pi/2} \left\{\frac{\partial^2}{\partial t^2}+2(\omega_c^2+6\alpha)\right\} \left(h^s(\vec{r}_s,t)+h_{ci}^s(\vec{r}_s,t)\right)\sin\theta^i d\theta^i d\phi^i$$

where $t = 2r-2r'[\sin\theta'\sin\theta^i\cos(\phi'-\phi^i)+\cos\theta'\cos\theta^i]$.

This is the complete solution to the three dimensional problem of recovering a body from its scattered field; it needs the reflected fields and the correction term from all possible directions. If the correction term is dropped, we can get the three dimensional time-domain PO inverse scattering identity

$$\gamma(r',\theta',\phi')=\frac{-2r}{\pi\omega_c}\int_0^{2\pi}\int_{-\pi/2}^{\pi/2}\left[2(\omega_c^2+6\alpha)+\frac{\partial^2}{\partial^2 t}\right]h^s(\vec{r},t)\bigg|_{t=2r-2\hat{r}\cdot\vec{r}'}\sin\theta^i d\theta^i d\phi^i \tag{3.66}$$

45

CHAPTER 4

TIME-DOMAIN IMAGING OF RADAR TARGETS USING

ALGORITHMS FOR RECONSTRUCTION FROM PROJECTIONS

4.1   Introduction

The basic idea of reconstruction of an image from a series of its projections appears to have been first discussed by Radon [16]. The techniques that exist for reconstruction fall into two directions. The whole operation can be done in frequency space directly, or the equivalent of these expressions can be transformed in the spatial domain. Whether implemented in the spatial domain or in the frequency domain, the reconstruction algorithms can be conveniently interpreted by means of a straightforward and interesting theorem, which is the projection-slice theorem. This theorem states that the Fourier transform of a projection is a center-cross-section of the Fourier transform of the projected object. Most of the modern tomographic systems are based on this theorem.

The algorithm that is currently being used in almost all applications of straight ray tomography is the filtered backprojection algorithm. It has been shown to be extremely accurate and amenable to fast implementation. We will extend this approach to our radar inversion problems. In this chapter we will show how to estimate the shape of a radar target using a short pulse radars. We start with the definition of backprojection and then develop the reconstruction algorithm based on the inverse scattering identities derived in

chapter 3.

4.2 Backprojection

Let (x,y) designate the coordinates of points in the x-y plane and let $\vec{x} = (x, y)$,

$\hat{\xi} = (\cos\phi, \sin\phi)$. Consider an arbitrary function $g(p,\hat{\xi})$ where $p = \hat{\xi} \cdot \vec{x} = x\cos\phi + y\sin\phi$.

The backprojection is defined by [13]

$$G(x,y) = \int_0^\pi g(x\cos\phi + y\sin\phi, \hat{\xi})\,d\phi \tag{4.1}$$

If the replacements $x = r\cos\theta$, $y = r\sin\theta$ are made, then G in polar coordinates becomes

$$G(r, \theta) = \int_0^\pi g[r\cos(\theta-\phi), \phi]\,d\phi \tag{4.2}$$

Observe that if we consider $g(p,\phi)$ is the projection function $F(p,\phi)$ from $f(x,y)$ by the Radon transform, then for fixed ϕ, the incremental contribution $d(G)$ to G at the point (x,y), or (r, θ), is given by $F(p,\phi)d\phi$. The full contribution to G at (x,y) is found by integrating over ϕ as indicated in (4.1). The operation for fixed ϕ is illustrated in fig. 4.1.

4.3 Reconstruction Algorithm

In chapter 3 we have described a method to extract the cross-sectional area function of a radar target from SMEP responses and obtained the thickness function. Here we will illustrate the image reconstruction algorithm.
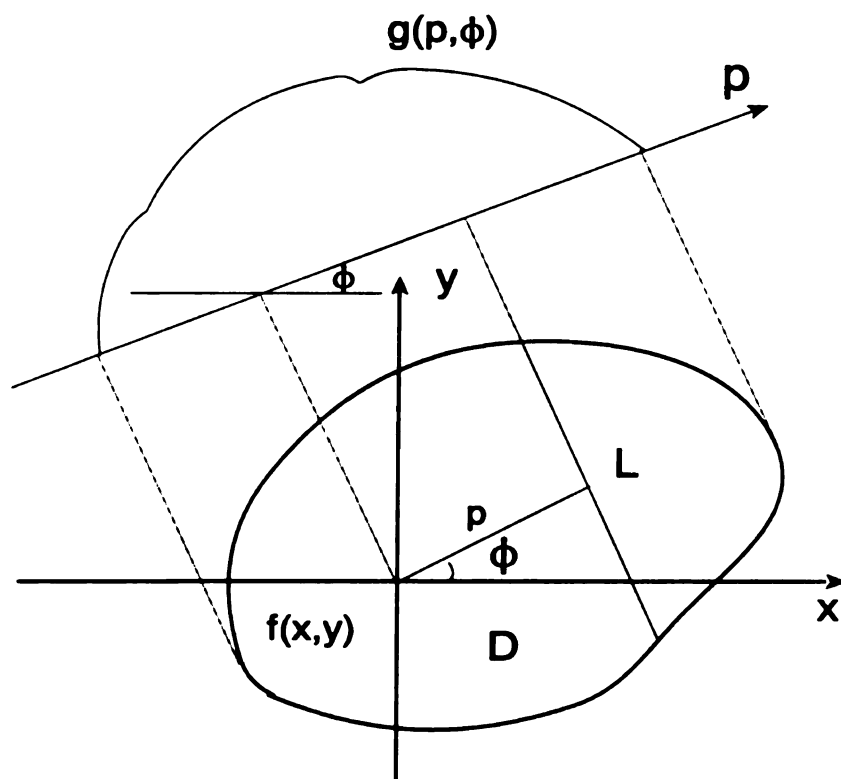
Figure 4.1   Geometry for obtaining the backprojection

Let's start with the thickness function $\Gamma(\bar{\rho}')$. It can be written as

$$\Gamma(\bar{\rho}') = -\frac{1}{2\pi^2}\int_0^\pi\int_{-\infty}^\infty \frac{f(\bar{\rho}',t)\,dt\,d\phi^i}{[t-\rho_{is}+2\rho'\cos(\beta/2)\cos(\phi'-\phi^i+\beta/2)]^2} \qquad (4.3)$$

where

$$f(\bar{\rho}',t) = \frac{4\rho_s\cos(\beta/2)}{(\vec{K}\cdot\hat{\rho})\omega_c}\left[H^s(\bar{\rho}_s',t) + 2\alpha\int_0^t H^s(\bar{\rho}_s',t)dt + (\omega_c^2+\alpha^2)\int_0^t\int_0^t H^s(\bar{\rho}_s',t)dt^2\right] \qquad (4.4)$$

From equation (4.3), we know that the inner integral is the convolution of $f(\rho_{is}-2\rho'\cos(\beta/2)\cos(\phi'-\phi^i+\beta/2))$ and $1/[\rho_{is}-2\rho'\cos(\beta/2)\cos(\phi'-\phi^i+\beta/2)]^2$. Equation (4.3) thus can be written as

$$\Gamma(\bar{\rho}') = \int_0^\pi\int_{-\infty}^\infty \frac{1}{2\pi}|\omega|F(\omega)\exp[j\omega(\rho_{is}-2\rho'\cos(\frac{\beta}{2})\cos(\phi'-\phi^i+\frac{\beta}{2}))]d\omega\,d\phi^i \qquad (4.5)$$

since the Fourier transform of $1/[\rho_{is}-2\rho'\cos(\beta/2)\cos(\phi'-\phi^i+\beta/2)]^2$ is $-\pi|\omega|$, and the

Fourier transform of $f(\rho_{is}-\rho'\cos(\beta/2)\cos(\phi'-\phi^i+\beta/2))$ is $F(\omega)$, and the convolution is the

Fourier transform of a product. We can see from equation (4.5) that the inner integral represents a filtering operation, where the frequency response of the filter is given by

$-\pi|\omega|$. Therefore the inner integral part is called a "filtered projection". The resulting

projections for different angles are then added to form the estimate of $\Gamma(\bar{\rho}')$.

When the projections are bandlimited by the highest frequency B, the projection

data are collected at the Nyquist frequency, with a sampling interval of $a = 1/(2B)$.

Equation (4.5) may be expressed as

$$\Gamma(\bar{\rho}') = \int_0^\pi \int_{-\infty}^\infty Q(\omega) \, F(\omega) \, \exp[j\omega(\rho_{is} - 2\rho'\cos(\beta/2)\cos(\phi' - \phi^i + \beta/2))] \, d\omega \, d\phi^i \quad (4.6)$$

where

$$Q(\omega) = \frac{1}{2\pi} |\omega| \, rect(\omega) \quad (4.7)$$

and

$$rect(\omega) = \begin{cases} 1 & |\omega| < 2\pi B \\ 0 & \text{otherwise} \end{cases} \quad (4.8)$$

$Q(\omega)$, shown in Figure 4.2, represents the transfer function of a filter with which the projections must be processed. The impulse response, q(t), of this filter is given by the inverse Fourier transform of $Q(\omega)$ and is

$$q(t) = \frac{1}{2\pi} \int_{-\infty}^\infty \frac{1}{2\pi} |\omega| \, rect(\omega) \, \exp(j\omega t) \, d\omega$$

$$= 2B^2 sinc(2\pi Bt) - B^2 sinc^2(\pi Bt) \quad (4.9)$$

This function is shown in Figure 4.3. Since the projection data are measured with a sampling interval of $1/(2B)$, for digital processing the impulse response need only be known with the same sampling interval. The samples, $q(n)$, of $q(t)$ are given by

$$q(n) = \begin{cases} \dfrac{1}{4a^2} & n = 0 \\ 0 & n = even \\ -\dfrac{1}{\pi^2 n^2 a^2} & n = odd \end{cases} \quad (4.10)$$

This filter was first discussed by Ramachandran and Lakshminarayanan [17]. We can replace integrals in (4.3) by sums and obtain the approximate reconstruction formula

50

given by

$$\Gamma(x,y) = \frac{a}{2N}\sum_{i=0}^{N-1}\sum_{k=-\infty}^{\infty} f(\phi^i,t_k)\,q(t_k-\rho_{is}+2\rho'\cos(\beta/2)\cos(\phi'-\phi^i+\beta/2)) \qquad (4.11)$$

where there are N angles ϕ^i for which the scattered fields are known.

There are two different reconstruction algorithms that can be used depending on how the filtering is done. If convolution in projection space is used to perform the filtering, the above reconstruction algorithm is referred to as the convolution backprojection technique. If the filtering is performed in Fourier space, however, the algorithm is designated the filtered backprojection technique. Both techniques produce comparable results.

For the convolution backprojection technique, the reconstruction algorithm consists of the following steps:

Step 1.   Create the cross-sectional area function $f(\phi^i,t_j)$ (also called projection) from measured data, i=1, 2, ..., N, j=-∞, ..., -1, 0, 1, ..., +∞.

Step 2.   Convolve the projection with the discrete impulse response of the filter to obtain the filtered projections.

Step 3.   Take the backprojection for the data obtained in step 3.

For the filtered backprojection technique, the reconstruction algorithm consists of the following steps:

Step 1.   The same as step 1 in the convolution backprojection method.

Step 2.   Take 1-D Fourier transforms of the projections obtained in step 1.

Step 3.   Multiply the transformed projections by the frequency response of the filter.

Step 4.   Take the inverse Fourier transform to obtain the filtered projections.

Step 5.   Take the backprojection for the data obtained in step 4.

Since the filtered backprojection and convolution backprojection techniques produce reconstructions of similar quality, we only use the convolution backprojection algorithm in this work.

4.4   Numerical Results and Images for a Metal Sphere

A metal sphere is the simplest target which can be used to validate the formulas developed in the previous sections. We use the SMEP as the incident magnetic field pulse. Figure 4.4 shows the theoretical SMEP generated by taking $\alpha=8\times10^9$ and $f_c=10GHz$ in equation (3.23), and the synthesized SMEP using the frequency band 4-16GHz. The spectrum of the synthesized SMEP is shown in Figure 4.5. Figure 4.6 shows the SMEP response of the sphere obtained using the marching-on-in-time method described in chapter 2. We can see that the solution is unstable. Figure 4.7 shows the results of using the stabilized formula (2.35). The results in Figure 4.7 is obviously much more stable than that in Figure 4.6. Figure 4.8 shows far-zone scattered field of a 14 inch sphere computed by using the Mie series and the marching on in time method, respectively. The cross-sectional areas obtained using equation (3.31) is shown in Figure 4.9. Note in Figure 4.9 that the cross-sectional area $A(\hat{r},t_s)$ is plotted with a time scale such that the cutting plane $t_s = \hat{r}\cdot\vec{r}'$ used to determine $A(\hat{r},t_s)$ moves with $1/(2\cos(\beta/2))$ (one half for the monostatic case) the velocity of the incident SMEP. Figure 4.10 shows the images of the sphere using the time domain identity (4.11) with the PO approximation. Figure 4.11 shows the image of the same sphere when the correction

52

terms are considered. We can see that the correction term provides only a small contribution to the reconstruction.

4.5. Experimental Results and Images for Aircraft

The time-domain identity (4.11) can be used in real time to construct an image from short pulse radar measurements. A simulation of time-domain imaging is carried out using data measured in the Michigan State University free-field scattering range. The field scattered from several aircraft models was measured in the plane of the aircraft wings in the frequency band 4-16GHz at 200 aspect angles from $0°$ (nose-on) to $180°$, using an HP8720B network analyzer. All measured data are bistatic with bistatic angle $\beta=10°$. The data from the non-illuminated side was provided through symmetry. Each scattered field response was first calibrated using a 14 inch diameter sphere as a reference target [see appendix), multiplied by the SMEP window, and then inverse transformed into the time-domain using the FFT to provide a SMEP response. The data we used are the derivative of the measured SMEP response data, and thus a sharpening of the target edges is provided.

Two different frequency truncated SMEPs haven been used in our radar target imaging. Figures 4.12, 4.13 and 4.14 show the images of a 1:48 scale model TR-1 aircraft, a 1:32 scale model F-14 aircraft and a 1:72 scale model B-52 aircraft, respectively, using the monostatic inverse scattering identity (3.40) under PO approximation and the synthesized SMEP shown in Figure 4.4. Figure 4.15, 4.16 and 4.17 shows the images of the same target models TR-1, F-14 and B-52, but using the bistatic identity (3.38) under PO approximation. We can see there are improvements in the images because the measured data are bistatic data. The edges of the aircraft are clearly visible,

with the fuselage and vertical stabilizers producing the largest thickness values, as expected. There is some distortion in the aircraft shapes due to the use of the PO approximation and an inaccurate estimate of target range. The image obtained using data from the restricted range of aspect angles 0-90° is shown in figure 4.18. It can be seen that the shadowed edges of the target are invisible due to the limited view-angles and use of the physical optics approximation. Figure 4.19 shows another theoretical SMEP generated by taking $\alpha=4\times10^9$ and $f_c=10GHz$ in (3.23) and the synthesized SMEP for the frequency band 7-13GHz. Figure 4.20 shows the spectrum of the synthesized SMEP. Figure 4.21 shows the image of the same 1:72 scale model B-52 aircraft obtained by using the second SMEP. We can see that the edges of the aircraft are not as clear as in Figure 4.17 because the pulsewidth is bigger than that of the first SMEP. We can improve the quality of the picture by adding a proper window to the SMEP response data in the time domain. This window is formed by two steps. First, the biggest points in each SMEP response data are found by comparing the values of the data; these biggest points actually are the responses from the scattering centers of the target. Then the values in a small range around the biggest point are set to unity and to 0.5 within the two next biggest point ranges. Note that different data sets have different windows. Figure 4.22 is a SMEP response data set before windowing, and the window produced based on Figure 4.22 is shown in figure 23. Figure 24 is the SMEP response after windowing. The image of the same B52 aircraft model found by using the windowed data is shown in figure 4.25. By using windowing, we have increased the resolution of the SMEP and obtained clear images with highly defined edges.
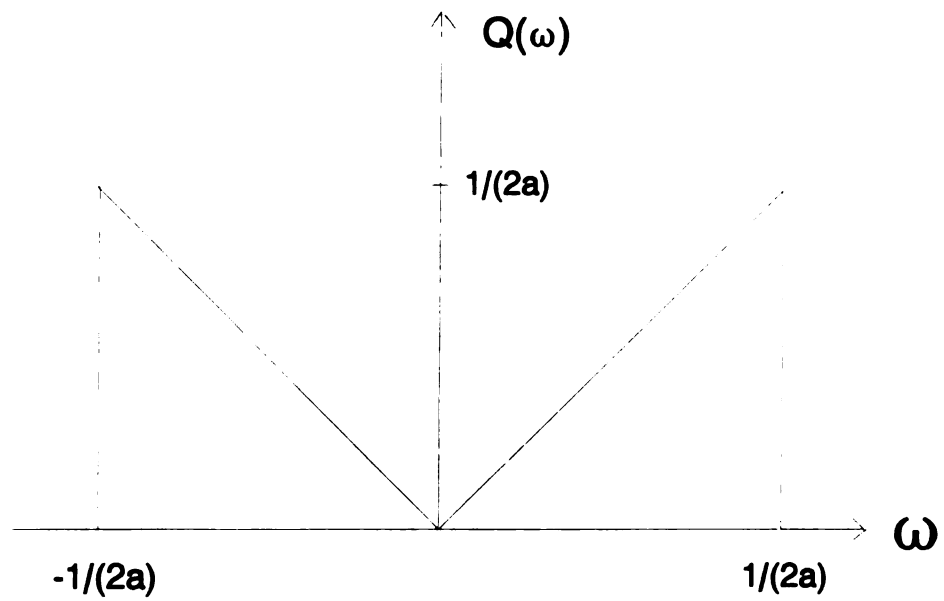
Figure 4.2 The filter response for the filtered backprojection algorithm. It has been bandlimited to 1/2a.
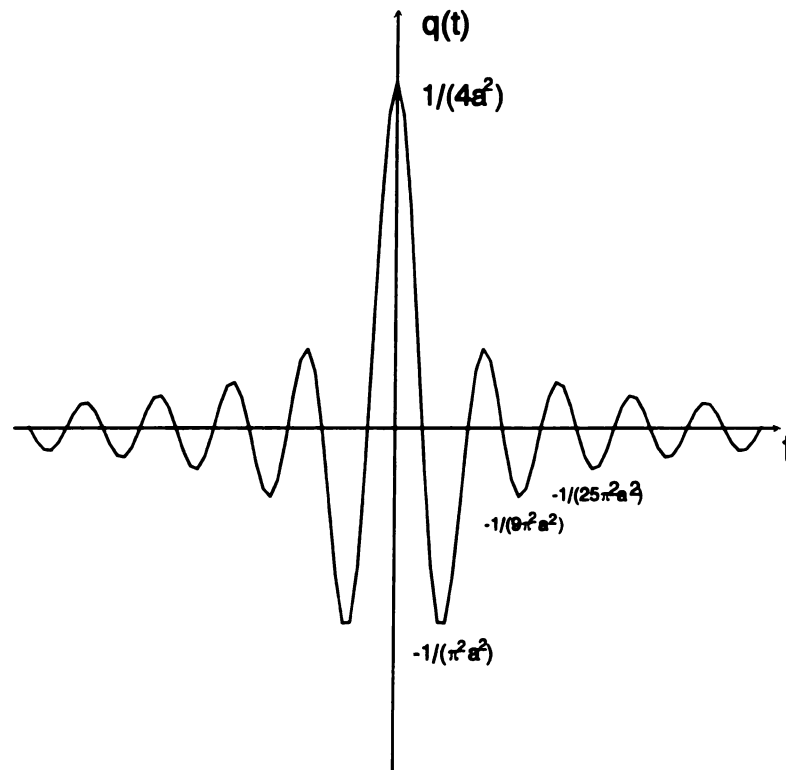
Figure 4.3   The impulse response of the filter shown in Figure 4.2.
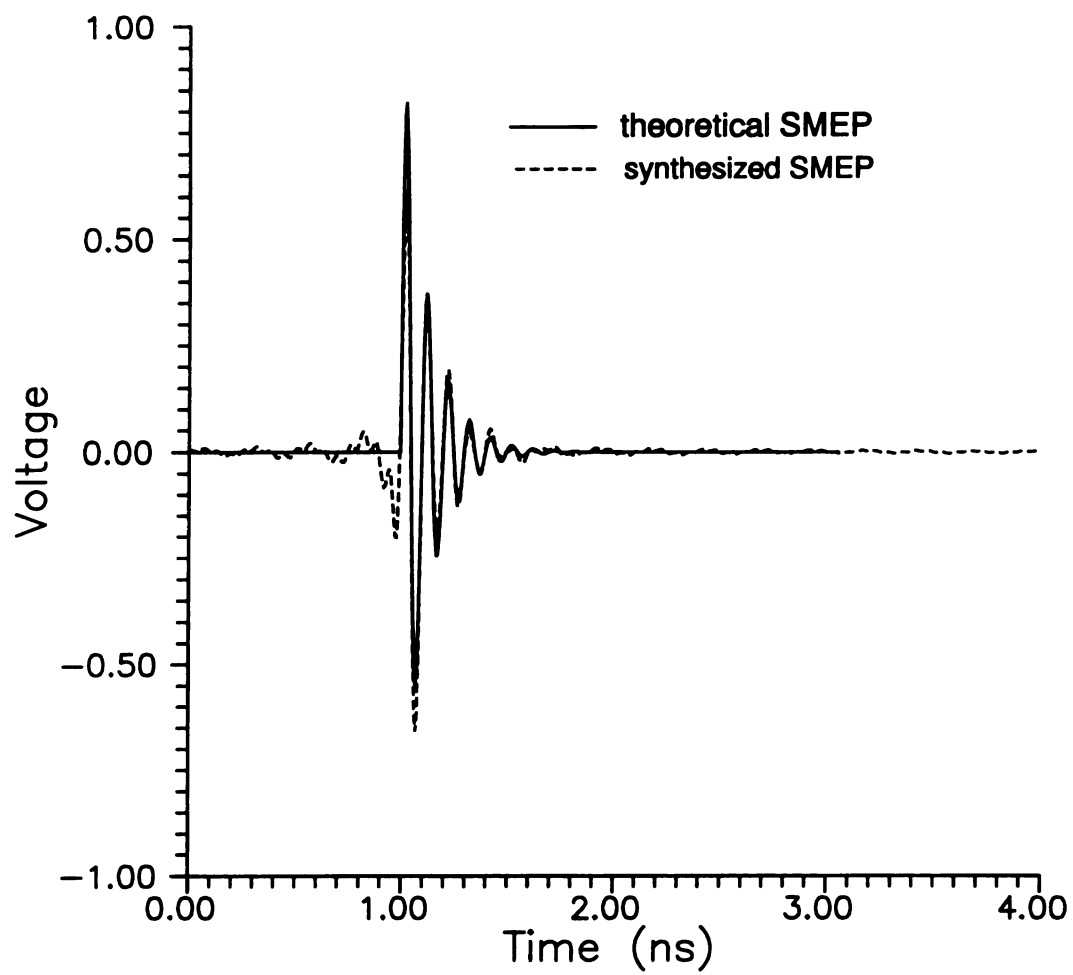
Figure 4.4 Comparison of theoretical ($\alpha=8x10^9$, $f_c=10GHz$ in (3.23)) and synthesized (4-16GHz) SMEP.
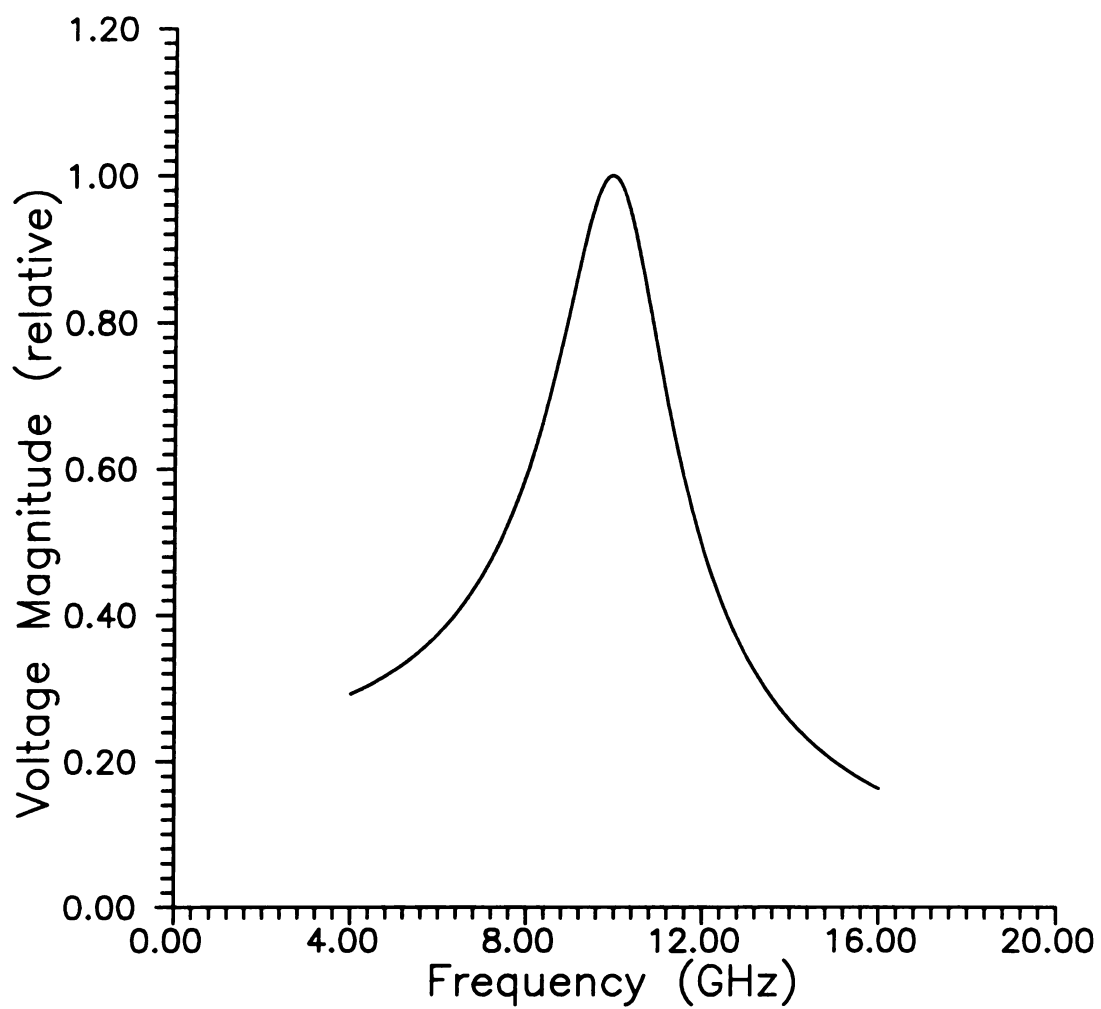
Figure 4.5   Synthesized SMEP spectrum.
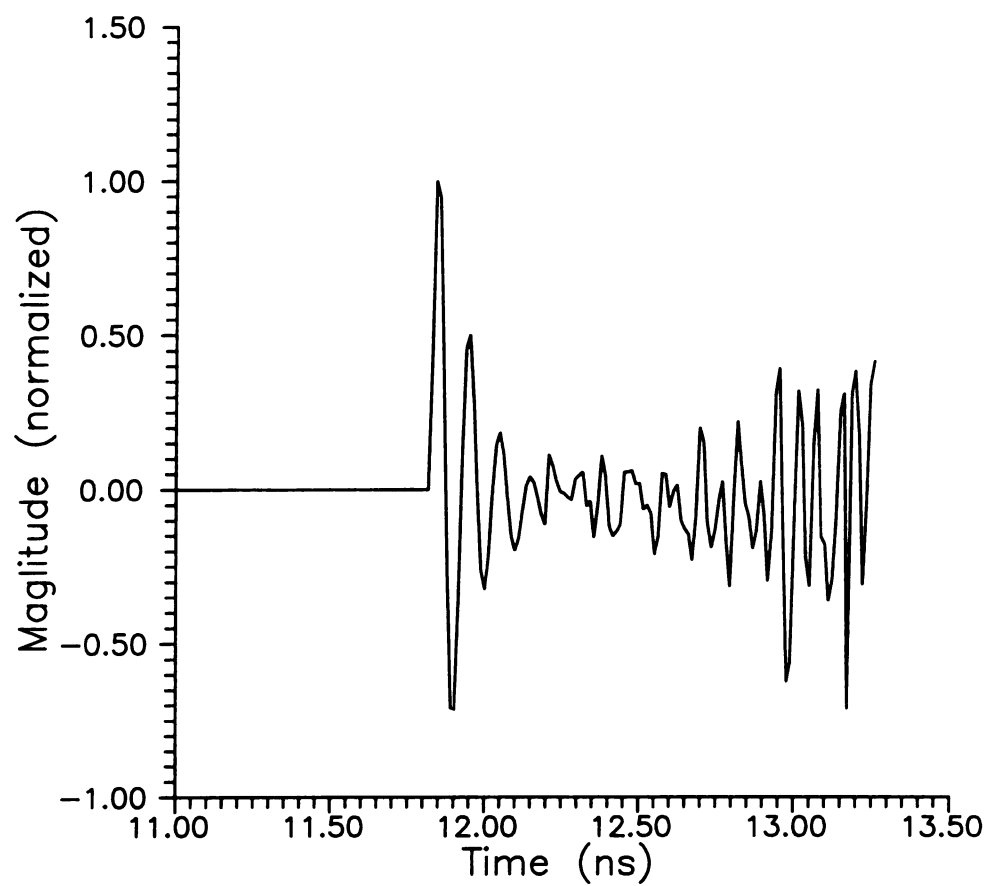
Figure 4.6   Far-zone SMEP response of sphere using marching-on-in-time method.
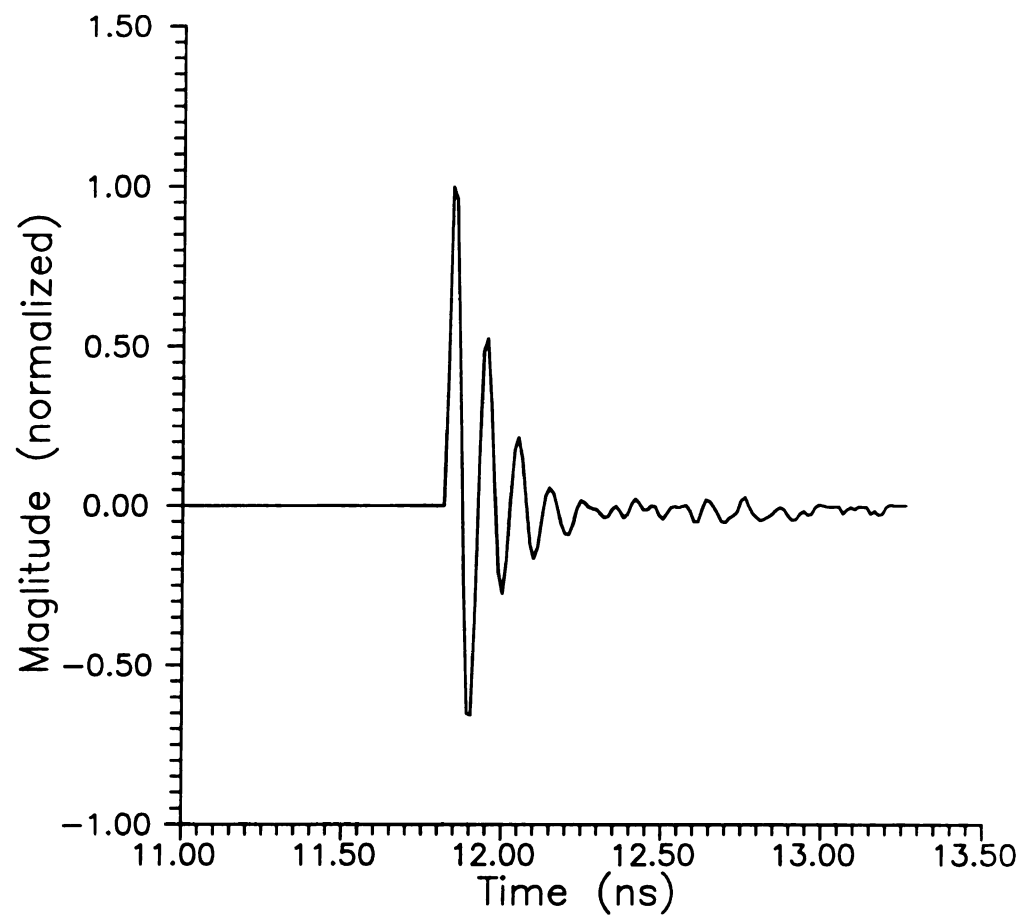
Figure 4.7   Result of using stabilized formula to the scattering field shown in Fig. 4.6.
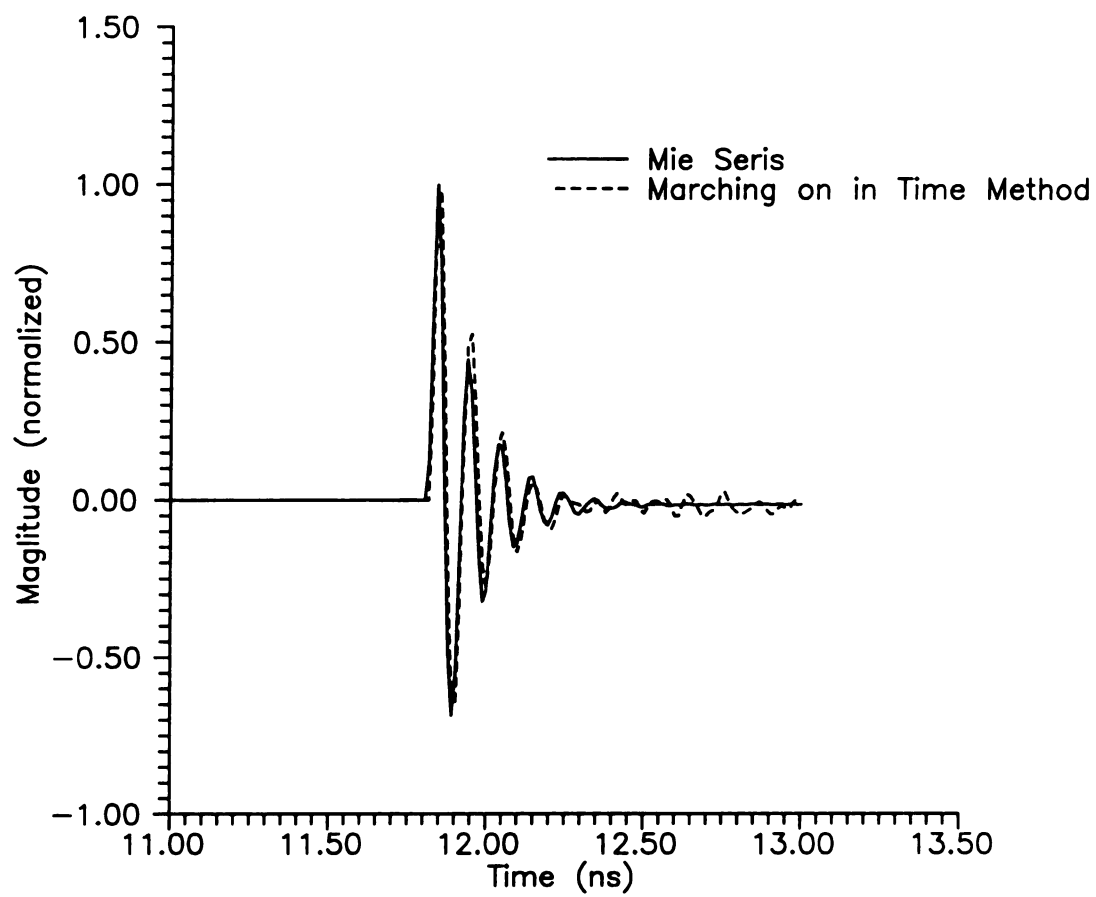
Figure 4.8   Far-zone SMEP scattered field of a 14 inch sphere
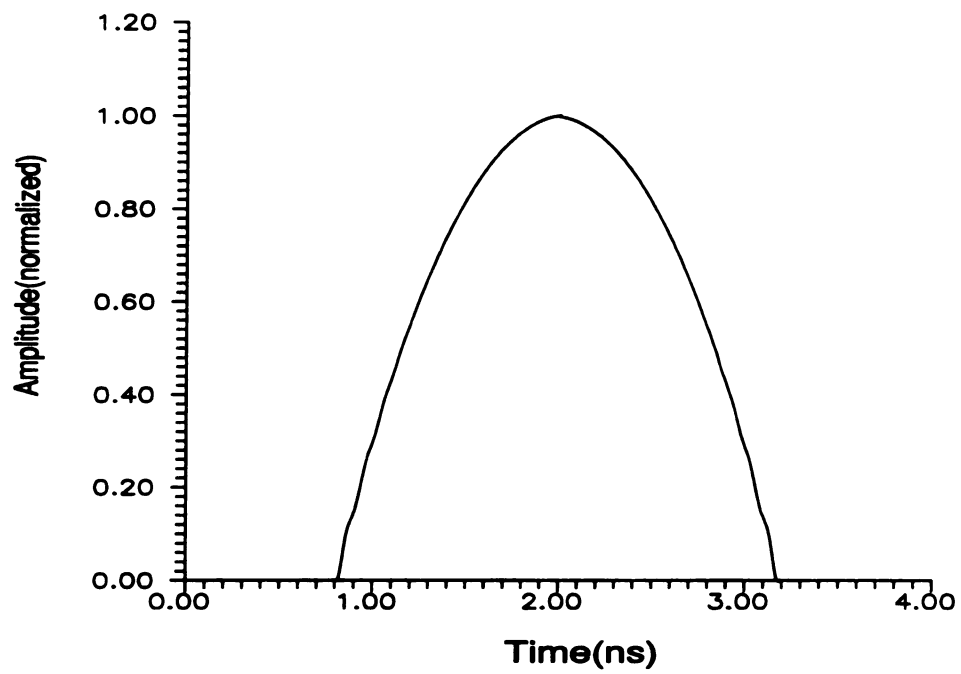
Figure 4.9　　Cross-sectional area function of a sphere 14 inches in diameter
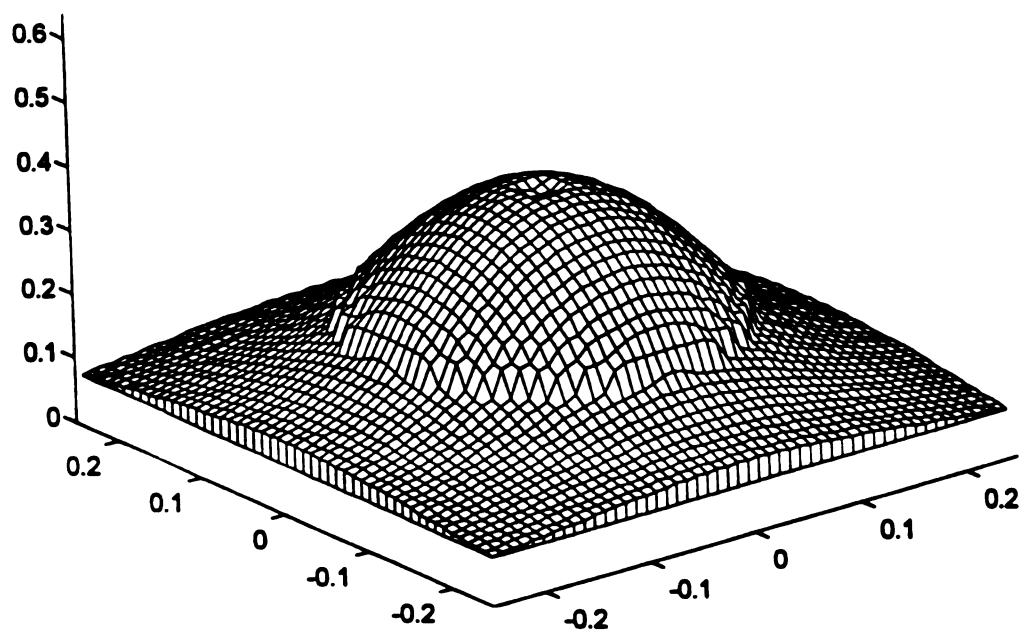
Figure 4.10 Upper surface image of the 14 inch diameter sphere using PO approximation.
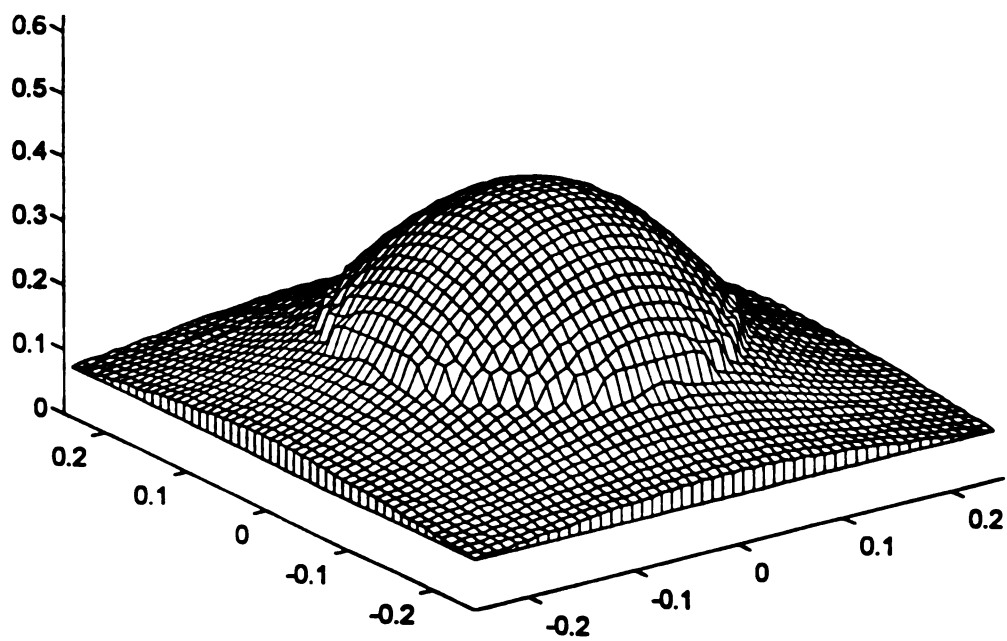
Figure 4.11 Upper surface image of the 14 inch diameter sphere considering the correction terms.
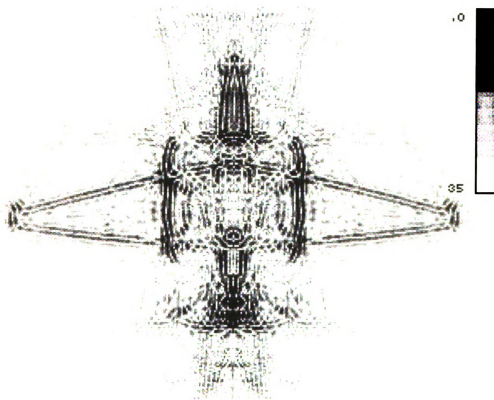
Figure 4.12 Image of TR-1 from 0°-180° data in band 4-16 GHz using monostatic identity.

Figure 4.13 Image of F-14 from 0°-180° data in band 4-16 GHz using monostatic identity.
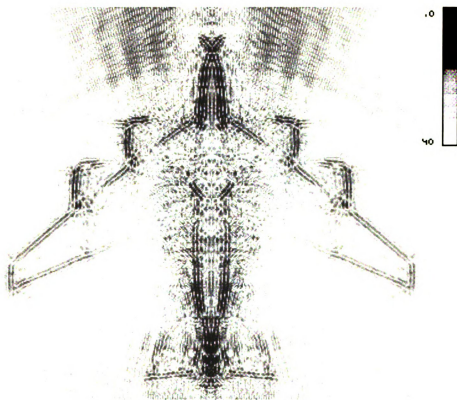
Figure 4.14. Image of B-52 from 0º-180º data in band 4-16 GHz using monostatic identity.
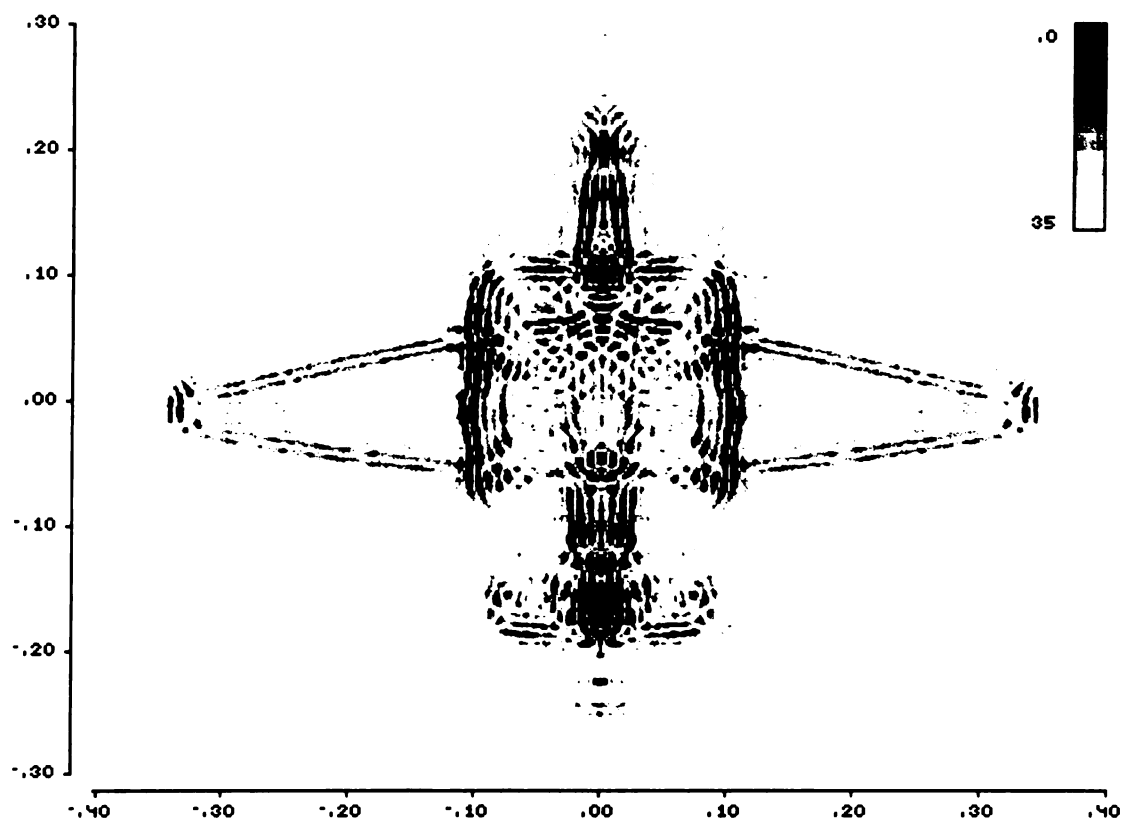
Figure 4.15 Image of TR-1 from 0°-180° data in band 4-16 GHz using bistatic identity.
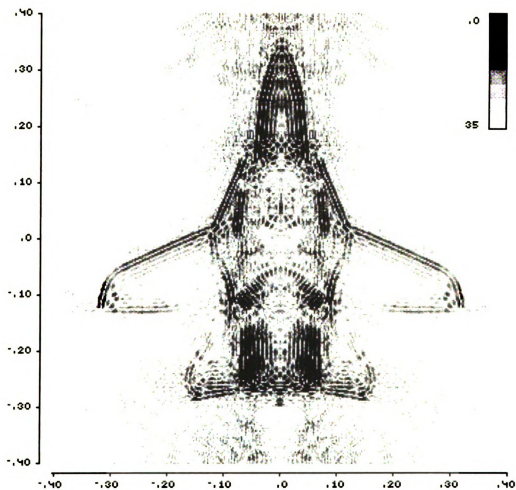
Figure 4.16 Image of F-14 from 0°-180° data in band 4-16 GHz using bistatic identity.
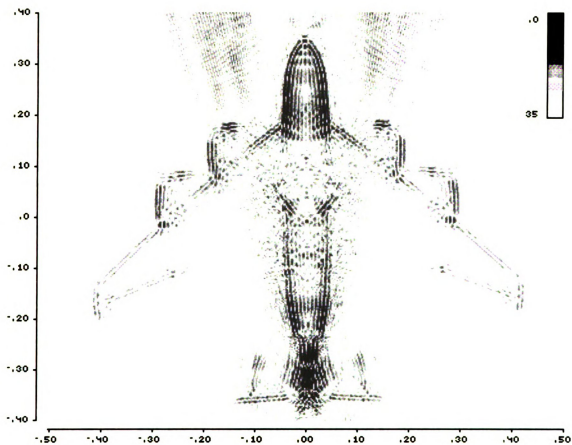
Figure 4.17. Image of B-52 from 0°-180° data in band 4-16 GHz using bistatic identity.
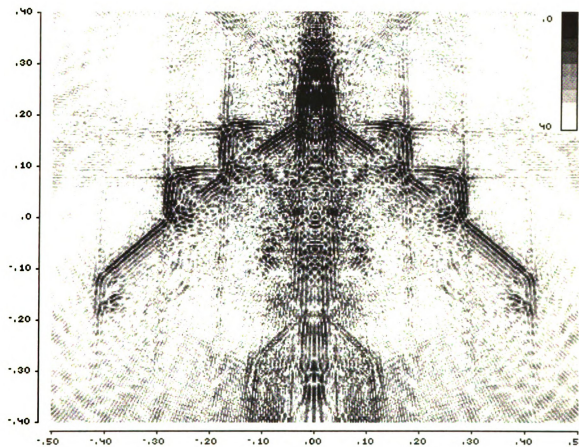
Figure 4.18. Image of B-52 from 0°-90° data in band 4-16 GHz using bistatic identity.
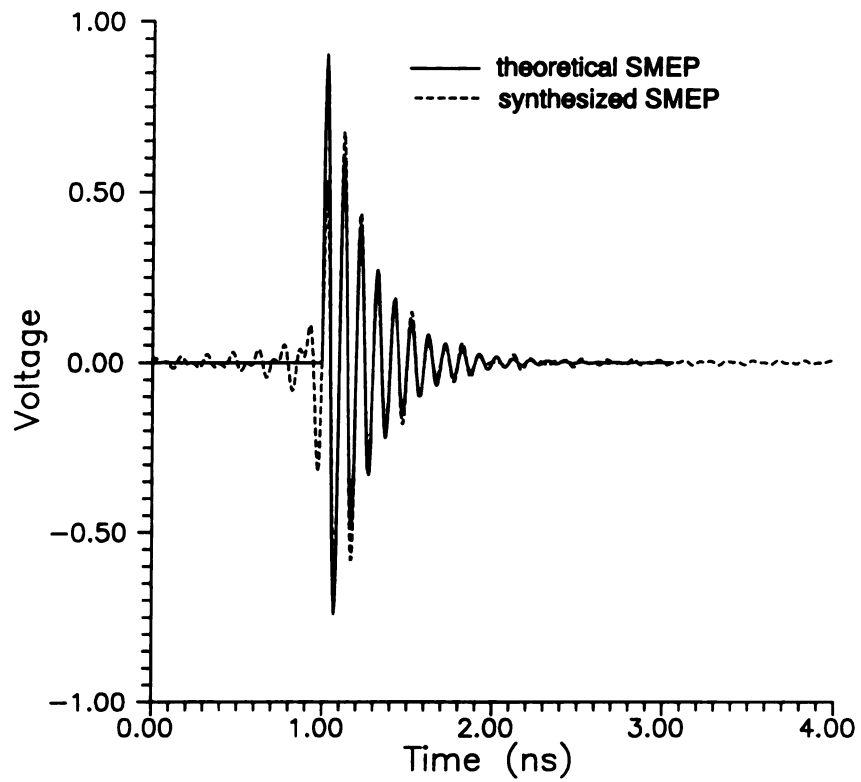
Figure 4.19 Comparison of theoretical ($\alpha=4x10^9$, $f_c=10GHz$ *in* (3.23) and synthesized (7-13GHz) SMEP.
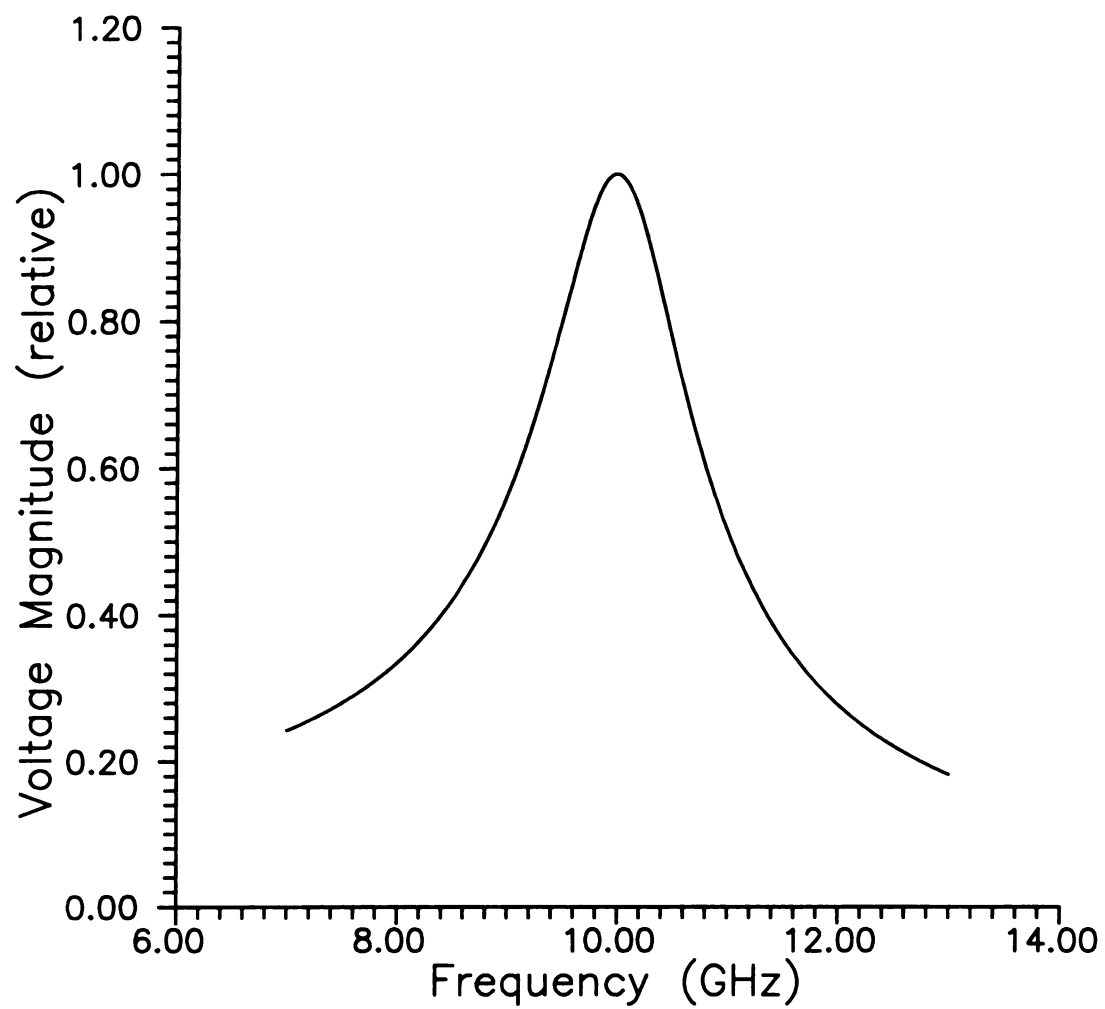
Figure 4.20 The spectrum of the synthesized SMEP.
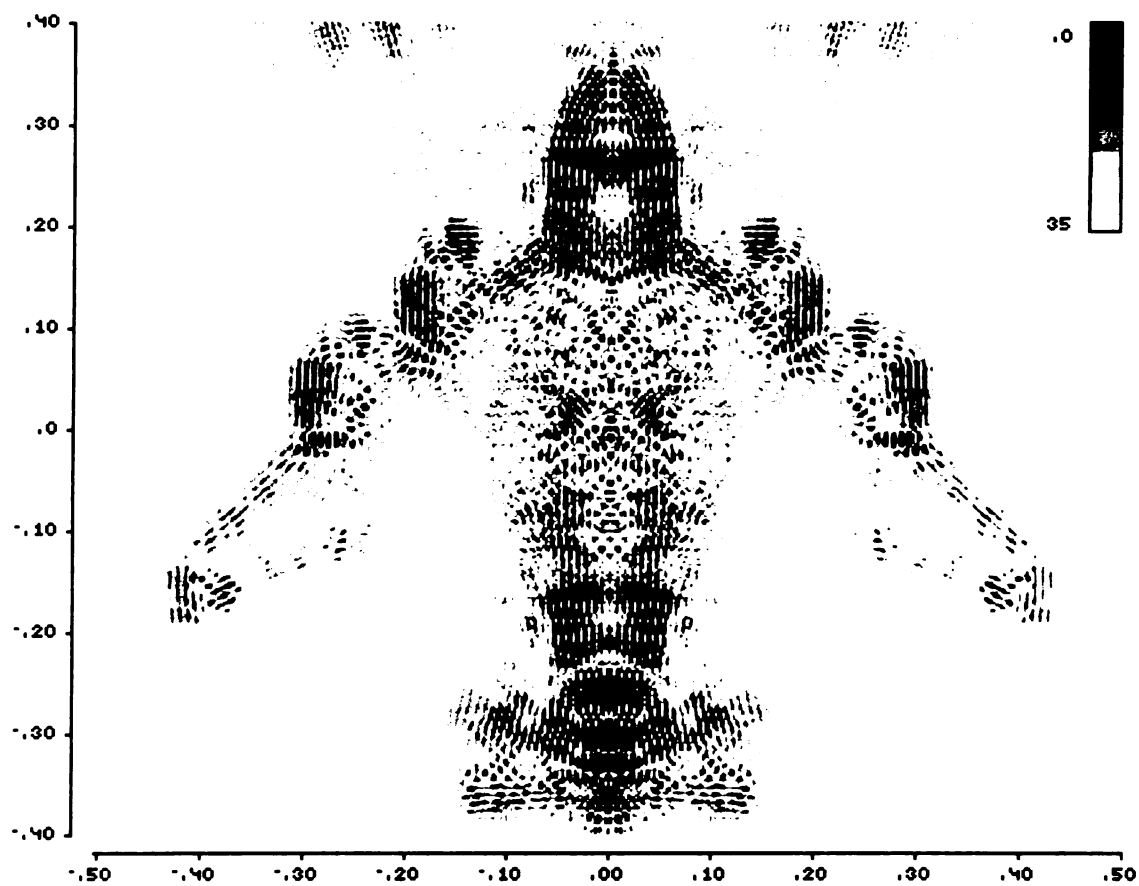
Figure 4.21. Image of B-52 from 0°-180° data in band 7-13 GHz using bistatic identity (before windowing).
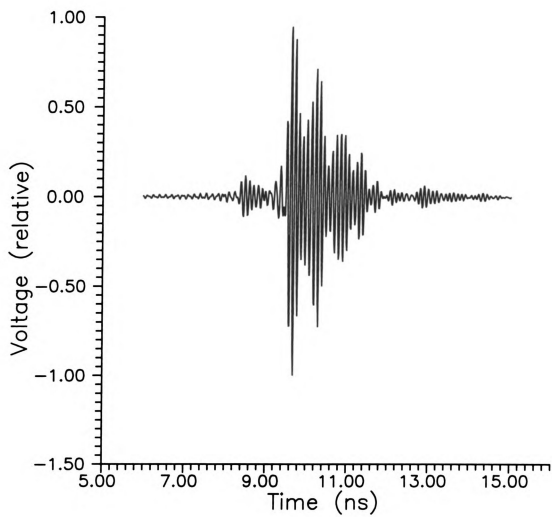
Figure 4.22. B-52 SMEP response (nose-on) before windowing.
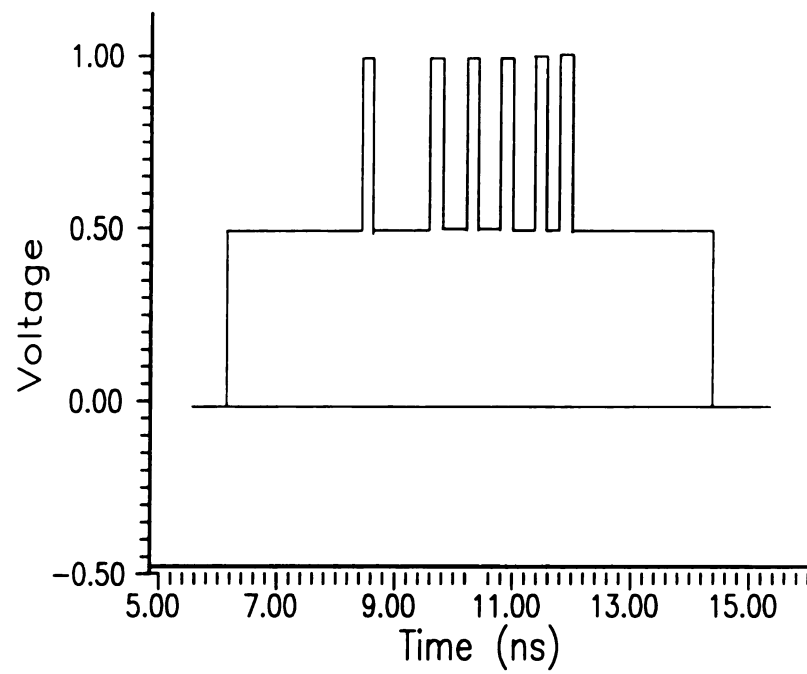
Figure 4.23. Window produced based on Figure 4.22.
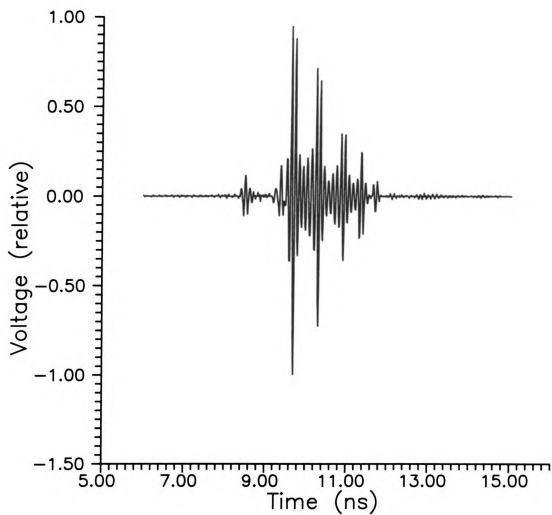
Figure 4.24. B-52 SMEP response (nose-on) after windowing.
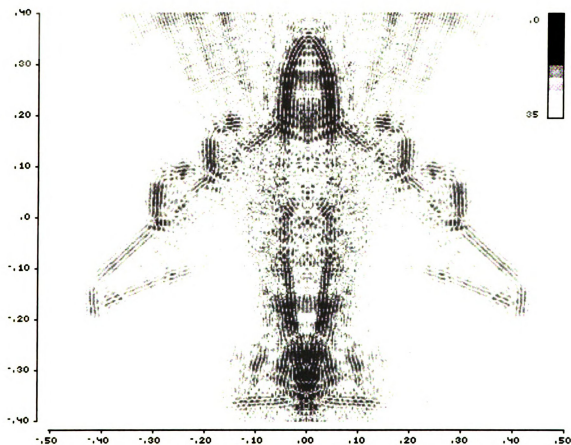
Figure 4.25. Image of B-52 from 0°-180° data in band 7-13 GHz using bistatic identity (after windowing).

CHAPTER 5

IMAGING OF RADAR TARGETS USING LIMITED-VIEW DATA

5.1   Introduction

In Chapter 3 and Chapter 4 we have shown that good images of radar targets may be obtained given enough high quality data over a 180° angular range. When some data are missing, the reconstructed image suffers and may be unsatisfactory. In practical cases, however, it is impossible to obtain enough data over a full 180° angular range. The limited-view problem occurs when the data are available over an angular range less than 180°, and the sparse-angle problem occurs when only a small number of angles evenly space over 180° are available.

The limited-view problems has attracted considerable attention in computed tomography imaging research, and techniques for dealing with it have been proposed. These techniques can be put into two categories: transform techniques that incorporate no a priori information, and finite series expansion methods that may incorporate a priori information as constraints. The transform techniques are usually single-pass, direct reconstructions [18-20], while the finite series expansion methods are usually iterative [21-27]. Projection onto convex sets (POCS) in particular has shown great flexibility in dealing with known geometric constrains and with noise. In Section 5.2, we will extend POCS into radar target imaging.

In addition to the POCS method, we will demonstrate a new reconstruction algorithm for radar imaging in the limited-angle case. The goal of this approach is to recover the sinogram from available measured data using linear prediction. Since the scattered field of a target can be written as a superposition of distinct specular reflections arising from scattering centers on the target, the trace of the scattering centers can be predicted using linear prediction with the change of the observation angle. Thus, the missing data may be predicted before reconstructing the image. This reconstruction algorithm will be described in Section 5.3.

5.2 The Method of Projections Onto Convex Sets (POCS)

The theory of convex projections developed by Bregman [22] and Gubin [23] was first applied to image processing by Youla and Webb [24]. Since then, various researchers has used POCS to restore computed tomography imagery based on incomplete data. To the author's knowledge, this method has not been used in radar imaging. Here we will give a brief review of POCS and apply it to radar imaging.

5.2.1 Basic Ideas

Assume a Hilbert space $\mathcal{H}$ consisting of the set $L_2(\Omega)$ of square-integrable complex-valued functions over $\Omega \in R^2$ (R^2 being the real plane). The inner product and norm in $\mathcal{H}$ are

$$(g,h) = \int\int_\Omega g(x,y) h^*(x,y) dx dy$$

(5.1)

$$\|g\| = [(g,g)]^{1/2}$$

The image to be restored $f(x,y)$ is assumed to be an element of $\mathcal{H}$. Every a priori

80

known property of the unknown $f \in \mathcal{H}$ is formulated as a constraint that restricts f to lie in a closed convex set C_i. If m properties are known, there exist m constraint sets C_i ($i=1,2,...,m$) and $f = \in C_o = \bigcap_{i=1}^{m} C_i$. Then our problem is to find a point in C_o given the sets C_i and the projection operators P_i ($i=1,2,...,m$) projecting onto the various C_i. A recursion relation given by

$$f_{k+1} = P_m P_{m-1} ... P_1 f_k \qquad k=0,1,2,...$$ (5.2)

with f_o being arbitrary, weakly converges to a point of C_o. More generally, various P_i may be relaxed by

$$f_{k+1} = T_m T_{m-1} ... T_1 f_k \qquad k=0,1,2,...$$ (5.3)

where $T_i = I + \lambda_i (P_i - I)$, $0 < \lambda_i < 2$ and I is the identity operator. The λ_i ($i=1,2,...,m$) are relaxation parameters and can be used to accelerate the rate of convergence. The projection operator P_i projecting onto C_i is defined by the minimality criterion

$$\|f - P_i f\| = \min_{g \in C_i} \|f - g\|$$ (5.4)

Equation (5.4) means that the projection $P_i f$ is $g \in C_i$ that minimized $\|f - g\|$. A symbolic representative of a projection is shown in Fig. 5.1.

5.2.2 Convex Projections in Short-Pulse Radar Imaging

In chapter 3 we have shown that the cross sectional area function and the thickness function of a target form a two dimensional Radon transform pair and can be written as
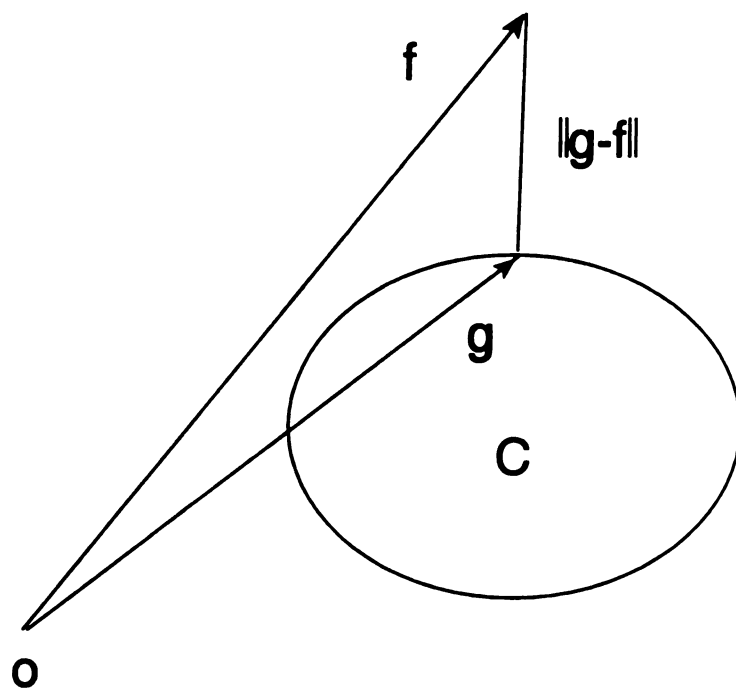
Figure 5.1   A symbolic representation of the projection of f onto C.

$$A_\Gamma(t_s,\phi) = \int\limits_{-\infty}^{\infty} \int \Gamma(x,y)\delta\big(t_s-(x\cos\phi+y\sin\phi)\big)dx\,dy \qquad (5.5)$$

In a discrete case where the thickness function is defined over a cartesian grid of $N_x \times N_y$ pixels, (5.5) becomes

$$A_\Gamma(t_s,\phi) = \sum_{i=1}^{N_x}\sum_{j=1}^{N_y} \Gamma(x_i,y_j)L_k(x_i,y_j) \qquad (5.6)$$

where $L_k(x_i,y_j)$ is the length of the kth line (ray) through pixel (x_i,y_j) as shown in Fig. 5.2. For N views and K lines per view, the total number of discrete cross sectional area functions (call it raysum) is $M=NK$. With a single subscript k ($k=1,2,...,M$), each raysum can be written as

$$A_\Gamma(t_{sk},\phi_k) = A_\Gamma(t_s,\phi) \qquad (5.7)$$

Let C_i be the set of all functions $h\in\mathcal{H}$ such that for a given (t_{sk},ϕ_k) they have given raysum values equal to that of the true thickness value $\Gamma(x,y)$. Denote this value by $A_\Gamma(t_{sk},\phi_k)$. Then

$$C_i = \big\{\, h\!: A_h(t_{sk},\phi_k) = A_\Gamma(t_{sk},\phi_k) \,\big\} \qquad k=1,2,...,M \qquad (5.8)$$

It has been shown that these constraint sets are closed and convex [26]. The projection operators that project onto C_i are given by

$$P_i g(x,y) = \begin{cases} g(x,y) & \text{for } g\in C_i \\[2ex] g(x,y) + \dfrac{A_\Gamma(t_{sk},\phi_k)-A_g(t_{sk},\phi_k)}{\displaystyle\sum_{m=1}^{N_x}\sum_{n=1}^{N_y} L_i^2(x_m,y_n)}L_i(x,y) & \text{for } g\notin C_i \end{cases} \qquad (5.9)$$

Other important constraints that can be used in radar image reconstruction are listed below.

1) Let C_A be the set of all real thickness function Γ's in $\mathcal{H}$ whose amplitudes must lie in a prescribed closed interval $[a,b]$; $a \geq 0$, $b > 0$, $a < b$. So, the amplitude limit constraint set is given by

$$P_A g = \begin{cases} a & g(x,y) < a \\ g(x,y) & a \leq g(x,y) \leq b \\ b & g(x,y) > b \end{cases} \qquad (5.10)$$

2) The bounded support constraint set is defined by

$$C_b = \{ \ h: \ h(x,y) = 0, \ (x,y) \notin A \ \} \qquad (5.11)$$

This means that C_b is the set of all functions in $\mathcal{H}$ that vanish outside a region A. The projection g onto C_b is given by

$$P_B g(x,y) = \begin{cases} g(x,y) & \text{if } (x,y) \in A \\ 0 & \text{if } (x,y) \notin A \end{cases} \qquad (5.12)$$

3) The reference image constraint set

$$C_R = \{ \ h: \ \|h - f_R\| \leq \epsilon_R \ \} \qquad (5.13)$$

In words, The reference image constraint set is used to restrict the reconstructed image to lying within a distance ϵ_R from f_R. The projection operator onto C_R is given by

$$P_R g = \begin{cases} g & \|g - f_R\| \leq \epsilon_R \\ g + \epsilon_R \dfrac{g - f_R}{\|g - f_R\|} & \|g - f_R\| > \epsilon_R \end{cases} \qquad (5.14)$$
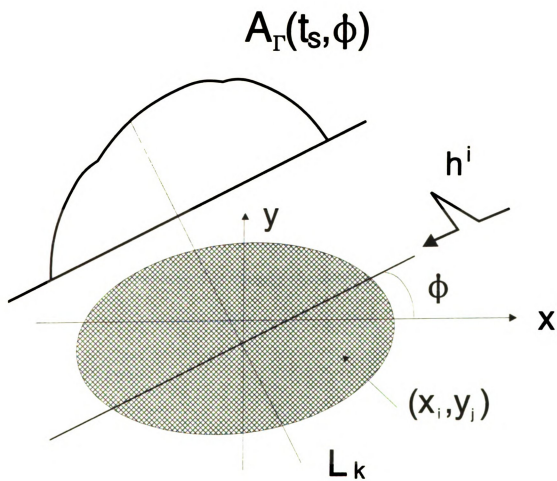
Figure 5.2   Discrete object, $\Gamma(x,y)$, and its projection are shown for an angle ϕ.

See reference [26] for the derivation of equation (5.14). The effectiveness of this constraint strongly depends on ε_R and f_R. It can be used to reduce the size of the feasible solution set C_0.

5.2.3 Experimental Results

The performance of the proposed POCS method was investigated with a 1:32 scale model F-14 aircraft shown in Figure 5.3. The aircraft image $\Gamma(x,y)$ was calculated on a 320×320 grid of rectangularly sampled points in the x-y plane by the cross sectional area function $A(t_s,\phi)$. The cross sectional area function was computed from measured data by equation (3.31) for various angles.

Equation (5.2) defines the general pure projection algorithm used in POCS. The specific POCS algorithm used in this experiment can be written as

$$f_{k+1} = P_R P_B P_A P_M \cdots P_1 f_k \tag{5.15}$$

with an initial point

$$f_0 = 0 \tag{5.16}$$

where P_M, ..., P_1 is the series of N projections onto N closed convex sets C_i (i=1,2,....,M) defined as in (5.9). The other projections in (5.15) have been defined in section 5.2.2.

Figure 5.4 shows the reconstruction image of aircraft model F-14 after 1 POCS iteration without use of reference image constraints in the angular range 0-180° with step angle $\Delta\phi$=0.9°. Figure 5.5 shows the reconstruction image of the same model after 5 POCS iterations using the same constraints as in Fig. 5.4. As seen in Figure 5.5, the iteration does little to improve the reconstructions.

To demonstrate the power of using a priori constraints in the POCS approach. we

need to consider reconstruction in the limited-view case. Figure 5.6 shows reconstruction images after 5 POCS iterations using Figure 5.5 as the reference image in the angular range $\phi=45°-135°$ with step angle $\Delta\phi=0.9°$. For convenience, an image obtained with the convolution backprojection directly on the incomplete data is shown in Figure 5.7. We can see that a significant improvement of reconstruction was achieved by the POCS algorithm.

5.3 Radar Image Reconstruction Using Sinogram Restoration and Linear Prediction

Image reconstruction from incomplete projections can be formulated as a sinogram-recovery problem. The sinogram recovery problem is to find a complete sinogram $A(t_s, \phi)$ based on the measured incomplete sinogram $A'(t_s, \phi)$ and a priori knowledge about the sinogram. Once an estimation of the complete sinogram is obtained, image reconstruction by the ordinary convolution backprojection is possible.

In this section, we will describe a sinogram-recovery method using linear prediction. In Section 5.3.1 we define the sinogram. In Section 5.3.2 the method of linear prediction is briefly reviewed and a solution to the sinogram-recovery problem is provided. In Section 5.3.3 we present experimental results that demonstrate the performance of the proposed method.

5.3.1 Sinograms

Projection data (cross-sectional area functions) used for image reconstruction can be arranged in a two-dimensional map in which one of the coordinates is the distance of
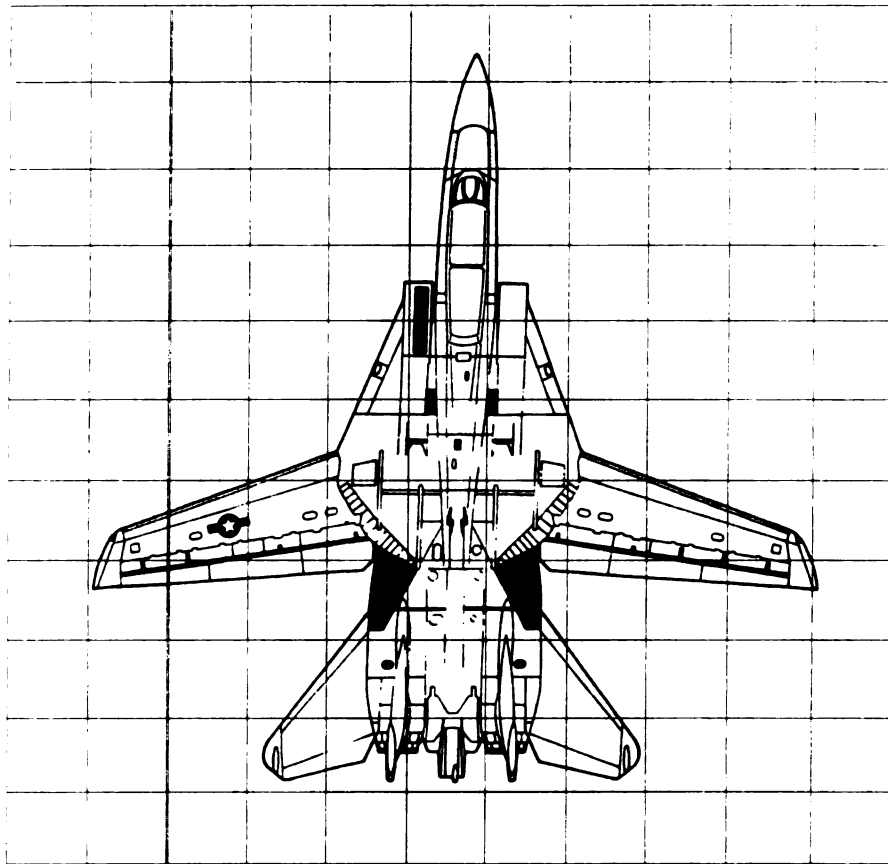
Figure 5.3   Geometry of discrete test image to be reconstructed.
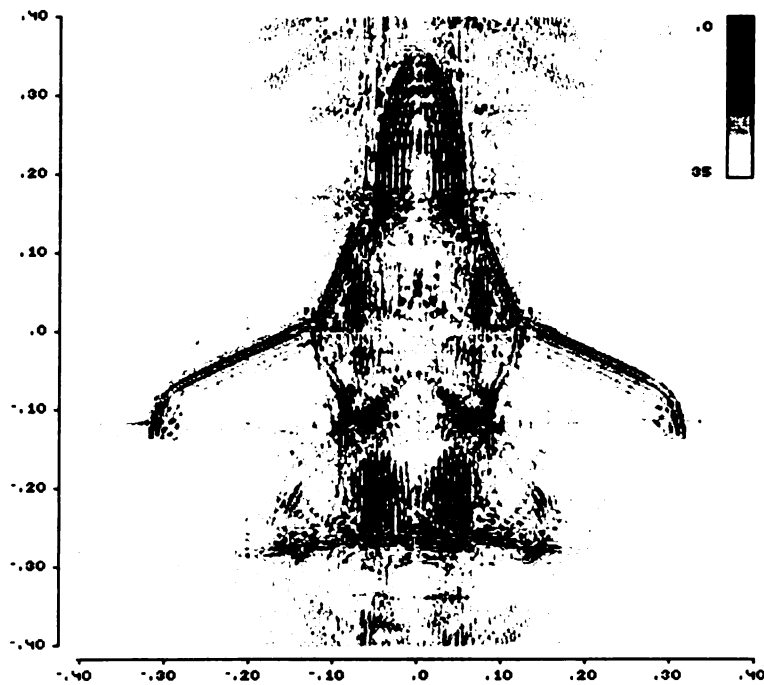
Figure 5.4 Image of F-14 from 0°-180° data in band 4-16 GHz using POCS after 1 iteration.
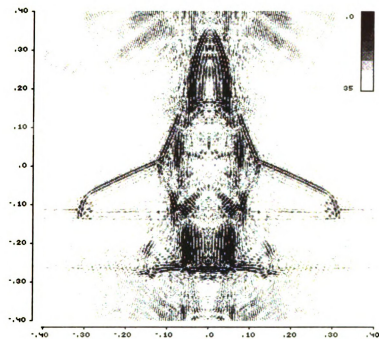
Figure 5.5 Image of F-14 from 0°-180° in band 4-16 GHz using POCS after 5 iterations.
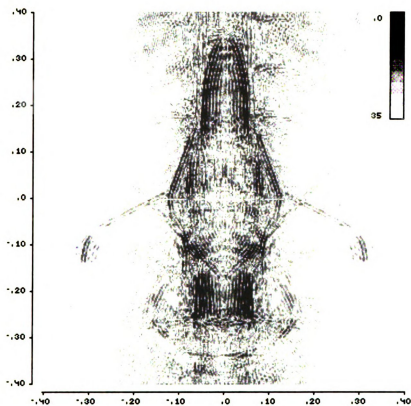
Figure 5.6 Image of F-14 from 45°-135° data in band 4-16 GHz using POCS after 5 iterations.
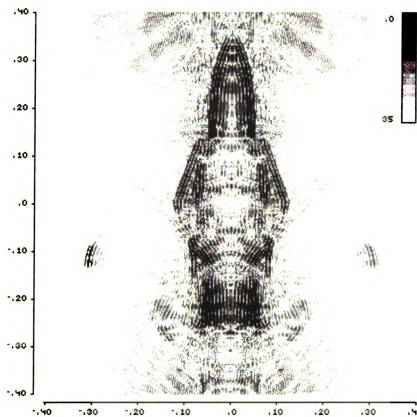
Figure 5.7 Image of F-14 from 45°-135° data in band 4-16 GHz using convolution backprojection algorithm.

the wave along which the line integral is taken from the center of the rotation of the projection system, and the other coordinate is the angle of the wave. In this map, waves through a fixed point in the object correspond to a sinusoidal curve, which is why a display of this map is called a sinogram [28].

Referring to the geometry of Figure 5.8, we have defined the 2-D Radon transform by equation (3.35) in chapter 3. In this section, we assume $\Gamma(x,y)$ to be a real function defined on the disk of radius T centered at the origin. A sinogram is an image of the 2-D Radon transform, where t_s and ϕ form the horizontal and vertical axes, respectively, of a cartesian coordinate system. Because of the periodicity of the 2-D Radon transform and because of the assumed domain of $\Gamma(x,y)$, the sinogram can be defined over the complete domain

$$\eta = \{(t_s,\phi) \mid t_s \in [-T,T], \ \phi \in [0,\pi] \} \tag{5.17}$$

For the limited-view problem, the sinogram is measurable over a domain ζ, where ζ is assumed to be a subset of η, i.e., $\zeta \in \eta$. ζ can be written as

$$\zeta = \{ (t_s,\phi) \mid t_s \in [-T,T], \ \phi \in [\phi_L, \pi - \phi_L] \} \tag{5.18}$$

where ϕ_L is a constant that represents the data's missing angular range. In Fig. 5.9 we illustrate the measurement domains ζ given by (5.18).

Figure 5.10 and Figure 5.11 show a 1:48 scale model TR-1 aircraft and its sinogram. Note that the sinogram is formed not from the cross sectional function but from the SMEP responses of the target. We can see from the sinogram that most of the 'lines' looks sinusoidal. Those lines actually are the traces of the scattering centers on the target. This motivates the idea of predicting the traces of the scattering centers using linear prediction. The following sections give a more detailed presentation of the approach.
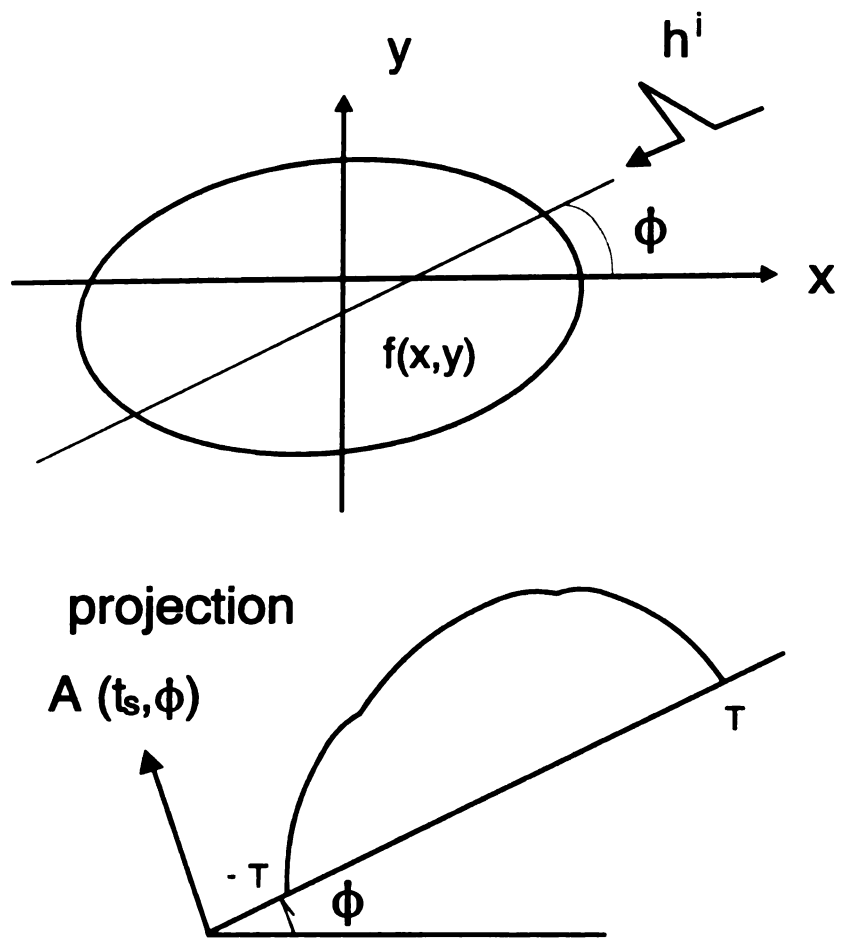
Figure 5.8   The geometry of the 2-D Radon transform.
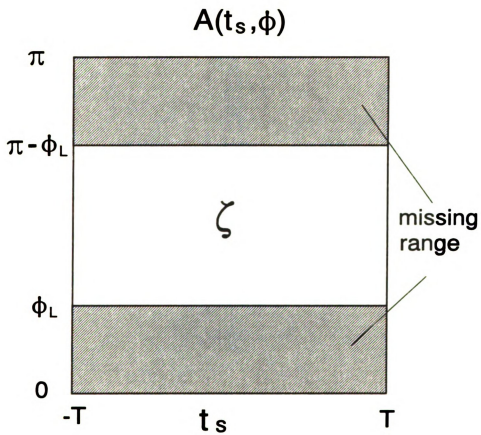
Figure 5.9 Domain ζ over which the sinogram is measurable in the limited-view problem
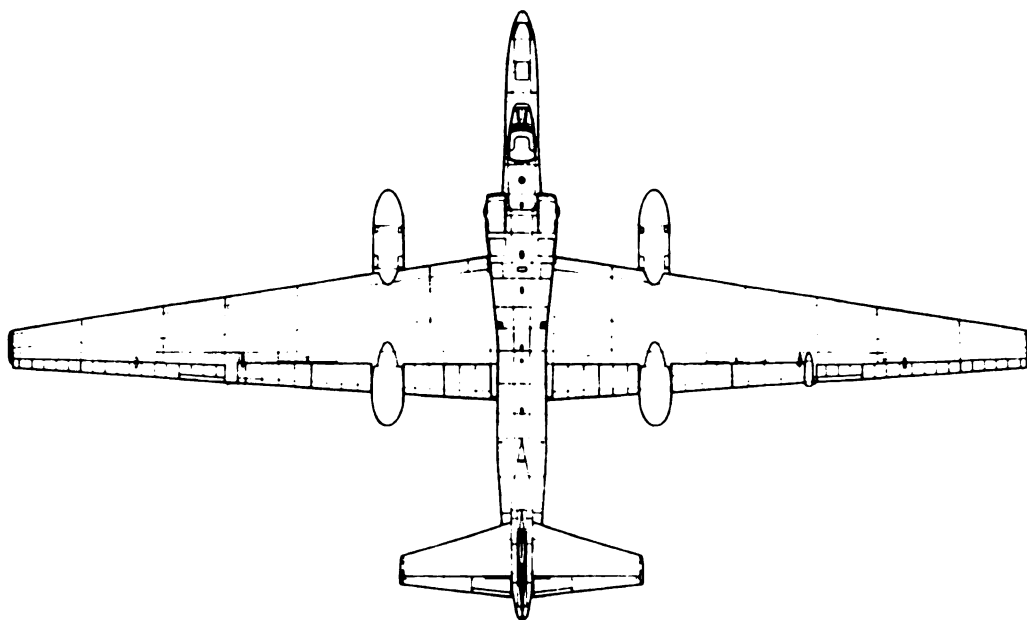
Figure 5.10 A 1:48 scale model TR-1 aircraft.

$\phi=180^{\circ}$

$\phi=0^{\circle}$

.0

40

Figure 5.11 The sinogram of TR-1 aircraft. 35 dB range, 1112 colors.

5.3.2 Linear Prediction

Linear prediction is a particularly important topic in digital signal processing with applications in a variety of areas, such as speech signal processing, image processing, and noise suppression in communication systems [29, 30]. In digital signal processing, the signal y_n is modeled as a linear combination of its past values and some input x_n

$$y_n = -\sum_{j=1}^{N} b_j y_{n-j} + x_n \qquad (5.19)$$

Equation (5.19) shows that the signal y_n is predictable from linear combinations of past outputs. We can consider x_n as the discrepancy of the prediction at time step n, i.e. the amount which must be added to the predicted value (the sum) to give the true value y_n.

Equation (5.19) can also be specified in the frequency domain by taking the z transform on both sides of (5.19). If $H(z)$ is the transfer function of the system, then we have from (5.19)

$$H(z) = \frac{Y(z)}{X(z)} = \frac{1}{1 + \sum_{j=1}^{N} b_j z^{-j}} \qquad (5.20)$$

where

$$Y(z) = \sum_{n=-\infty}^{\infty} y_n z^{-n} \qquad (5.21)$$

is the z transform of y_n, $X(z)$ is the z transform of x_n, and $H(z)$ in (5.20) is the all-pole model (autoregressive model). This model is shown in Fig. 5.12 in the time and frequency domains. Given a particular signal y_n, the problem is to determine the predictor coefficients b_j in some manner. The derivations will be given using the least squares

$$H(z) = \frac{1}{1 + \sum_{j=1}^{N} b_j z^{-j}}$$

(a)

$$y_n$$

$$x_n \xrightarrow{+} \Sigma$$

linear predictor
of order N

$$y_{n-1}$$

$$z^{-1}$$
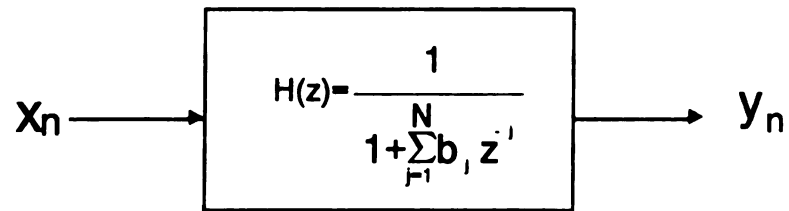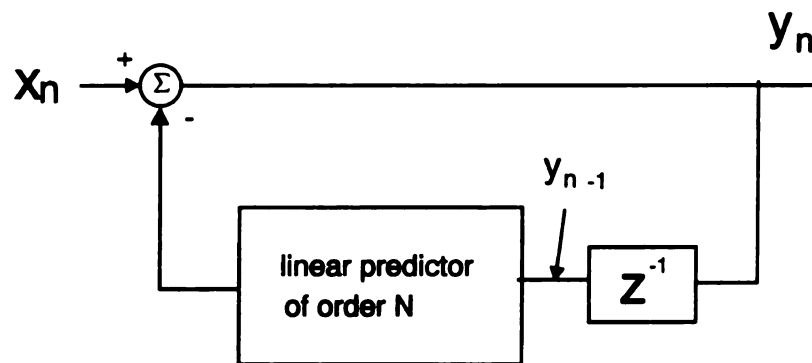
(b)

Figure 5.12 (a) Discrete all-pole model in the frequency domain. (b) Discrete all-pole model in the time domain.

approach.

The prediction error x_n can be written as

$$x_n = y_n + \sum_{j=1}^{N} b_j y_{n-j} \qquad (5.22)$$

In the method of least squares, the parameters b_j are obtained as a result of the minimization of the mean with respect to each of the parameters. The total squared error E is

$$E = \sum_n e_n^2 = \sum_n \left(y_n + \sum_{j=1}^{N} b_j y_{n-j} \right)^2 \qquad (5.23)$$

The minimization of E given by setting

$$\frac{\partial E}{\partial b_j} = 0 \qquad j=1,2,...,N \qquad (5.24)$$

leads to the set of linear equations

$$\sum_{j=1}^{N} b_j \sum_n y_{n-j} y_{n-k} = -\sum_n y_n y_{n-k} \qquad k=1,2,1,...,N \qquad (5.25)$$

Letting $\gamma_y(k) = \sum_n y_n y_{n-k}$, (5.25) can be simplified as

$$\gamma_y(k) = -\sum_{j=1}^{N} b_j \gamma_y(k-j) \qquad k=1,2,...,N \qquad (5.26)$$

These are called the normal equations for the coefficients of the linear predictor. The minimum mean-square prediction error is simply

$$E_N = \gamma_y(0) + \sum_{j=1}^{N} b_j \gamma_y(-j) \qquad (5.27)$$

by expanding (5.23) and substituting (5.26), the normal equations may be expressed in

the compact form

$$\sum_{j=0}^{N} b_j \gamma_y(k-j) = 0 \qquad j=1,2,...,N \text{ with } b_0=1 \qquad (5.28)$$

The resulting minimum mean-square prediction error is given by (5.27). If we augment (5.27) by the normal equations given by (5.28), we obtain the set of augmented normal equations, which may be expressed as

$$\sum_{j=0}^{N} b_j \gamma_y(k-j) = \begin{cases} E_n & j=0 \\ 0 & j=1,2,...,N \end{cases} \qquad (5.29)$$

or

$$\begin{bmatrix} \gamma_y(0) & \gamma_y(1) & \cdots & \gamma_y(N-1) \\ \gamma_y(1) & \gamma_y(0) & \cdots & \gamma_y(N-2) \\ \vdots & & & \vdots \\ \gamma_y(N-1) & \gamma_y(N-2) & \cdots & \gamma_y(0) \end{bmatrix} \begin{bmatrix} 1 \\ b_1 \\ \vdots \\ b_N \end{bmatrix} = \begin{bmatrix} E_N \\ o \\ \vdots \\ 0 \end{bmatrix} \qquad (5.30)$$

The matrix in (5.30) is a symmetric Toeplitz matrix, i.e. one whose elements are constant along diagonals. There are several computationally efficient algorithms for solving the normal equations [30]. In this work we use the Levinson-Durbin algorithm.

After solving for the linear prediction coefficients b_j, the next issue which needs to be considered is stability. The condition that (5.19) be stable as a linear predictor is that the characteristic polynomial in equation (5.20), i.e.

$$z^N - \sum_{j=1}^{N} b_j z^{N-j} = 0 \qquad (5.31)$$

has all N of its roots inside the unit circle, $|z| \leq 1$. There is no guarantee that the coefficients produced by the Levinson-Durbin algorithm will satisfy this condition. When instability is a problem, we have to modify the linear prediction coefficients. We do this

101

by the following three steps:

1)   Solving (numerically) equation (5.31) for its N complex roots.

2)   Moving the roots which lie outside unit circle to an appropriate position inside or

on the unit circle.

3)   Reconstituting the modified linear prediction coefficient.

Another consideration is the choice of N, the number of poles. One should choose

N to be as small as practicable for you. We choose N between 5 and 15, depending on

the number of data used.

5.3.3   Experiment Results

Consider the sinogram of the TR-1 aircraft model shown in Fig. 5.11. When only

part of the sinogram (domain ζ) as shown in Fig. 5.13 (for example $45°{\le}\phi{<}135°$) is

measurable, then the reconstructed image may be seriously distorted if we simply let the

missing data be zero. Our goal is to restore the complete sinogram (domain η) using

linear prediction techniques before reconstructing the image by the convolution

backprojection algorithm. The techniques which we proposed can be summarized as the

following steps:

Step 1.   Given a set of measured data $P_{\phi_i}(t_j)$ ($\phi_L{\le}\phi_i{<}\pi{-}\phi_L$), i=1, 2, ..., N_ϕ, j=1, 2, ...,

N_t, where N_ϕ is the number of views and N_t is the number of samples in

each view, find the biggest point (the darkest points in Fig. 5.11) in each

SMEP responds by comparing the values of the data in each view. These

biggest points are actually the positions of the scattering centers of the

target. Those points with large amplitude form a new sinogram. Fig. 5.14

102

shows the measurable sinogram of the TR-1 formed by these points, and Fig. 5.15 gives the complete sinogram of the TR-1 formed by these points.

Step 2.   From the new sinogram, find the traces of the scattering centers. Then one obtains a set of functions, each function designating the movement of a scattering center with the change of view. In Fig 5.15, for example, number 3 and number 4 denote the movements of the tail and the head of the aircraft model, respectively, number 1 and number 2 denote the movements of two wings, and number 5 denotes the movement of the engines.

Step 3.   Predict the movement of the scattering centers over the whole sinogram region η using linear prediction techniques. Fig. 5.16 shows the predicted traces of the scattering centers. Fig. 5.17 gives the trace of the tail with measured and predicted data, and Fig. 5.18 shows the traces of the engines with measured data and predicted data.

Step 4.   Predict the amplitude of the scattered field at the positions of the scattering centers. We use linear prediction twice, once for the traces of the scattering centers, and once for the amplitude of the scattered filed at the scattering centers. Fig. 5.19 and Fig. 5.20 gives the measured and predicted amplitudes of the scattered field at the positions of the tail and the engines.

Step 5.   Reconstruct the sinogram of the target over the domain η. For each view over the missing region, find those predicted scattering centers. Then make a small window (rectangular, Gaussian, or cosine taper window, we use rectangular window in this work) around each scattering point and multiply the window by a SMEP defined in (3.23). Then the predicted SMEP

103

responses are found for this view. Fig 5.21 shows the measured data and the predicted data for observation angle ϕ=40.5°.

Step 6. After predicting all the SMEP responses over the missing data region in domain η, we can restore the complete sinogram over domain η. The restored sinogram is shown in Fig 5.22.

Step 7. Reconstruct the image by convolution backprojection using the restored sinogram. Fig 5.23 gives the image of TR-1 aircraft model using the restored sinogram, and Fig 5.24 gives the image of TR-1 using the original incomplete sinogram shown in Fig. 5.13. We can see that there is a big improvement in the quality of the reconstructed images by using the sinogram restoration techniques.

5.4   Conclusions

For the limited-view problem, we have proposed two techniques to handle this practical situation. One of the approaches is the method of projections onto convex sets (POCS). The basic principle of POCS is that each piece of a priori knowledge must be represented by a convex set onto which the current image estimate can be projected. It has been shown that if the intersection of these convex sets is nonempty then the sequence of cyclic projections will converge weakly to a point in this intersection. We extend this approach to radar imaging for the first time and show some useful results. Another approach which we have demonstrated is to process the available measured projections in order to generate an estimate of the full set of projections, an image which is called a sinogram. The goal of this approach is to recover the sinogram from the available measured data using linear prediction. Since the scattered field of a target can

104

be written as a superposition of distinct specular reflections arising from scattering centers on the target, the position and strength of the scattering centers can be predicted using linear prediction with the change of the observation angle. Thus, the missing data can be predicted before reconstructing the image. A big improvement in image reconstruction has been achieved using this technique, and some useful results have been provided.
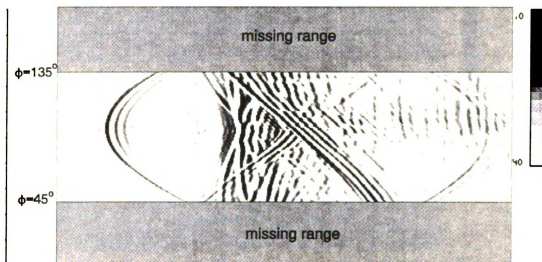
Figure 5.13 Measurable part of the sinogram of TR-1 aircraft.

106
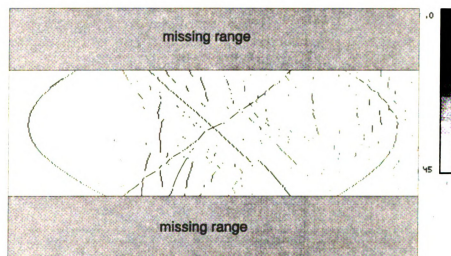
Figure 5.14 Measurable part of the sinogram of TR-1 formed by the positions of the scattering centers.
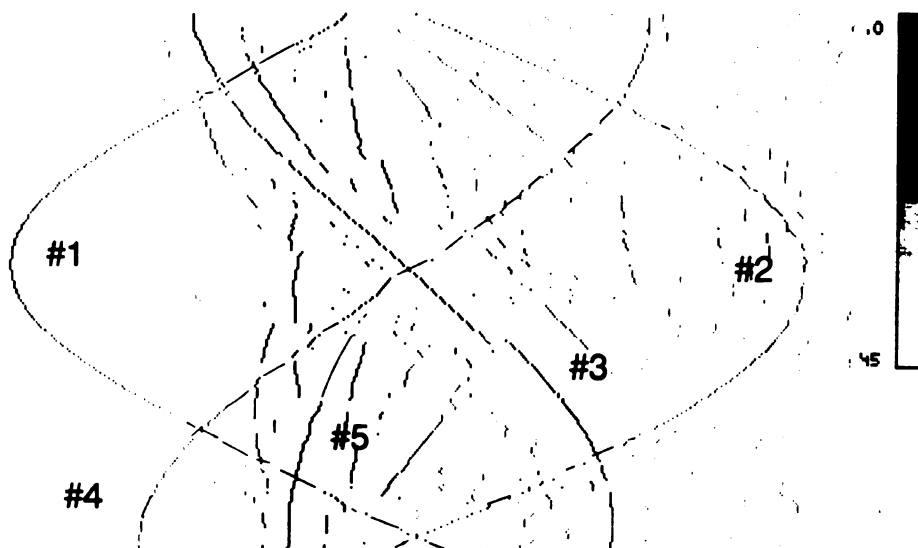
Figure 5.15 Sinogram of TR-1 formed by the positions of the scattering centers.

Figure 5.16 Sinogram of TR-1 formed by the predicted positions of the scattering centers.
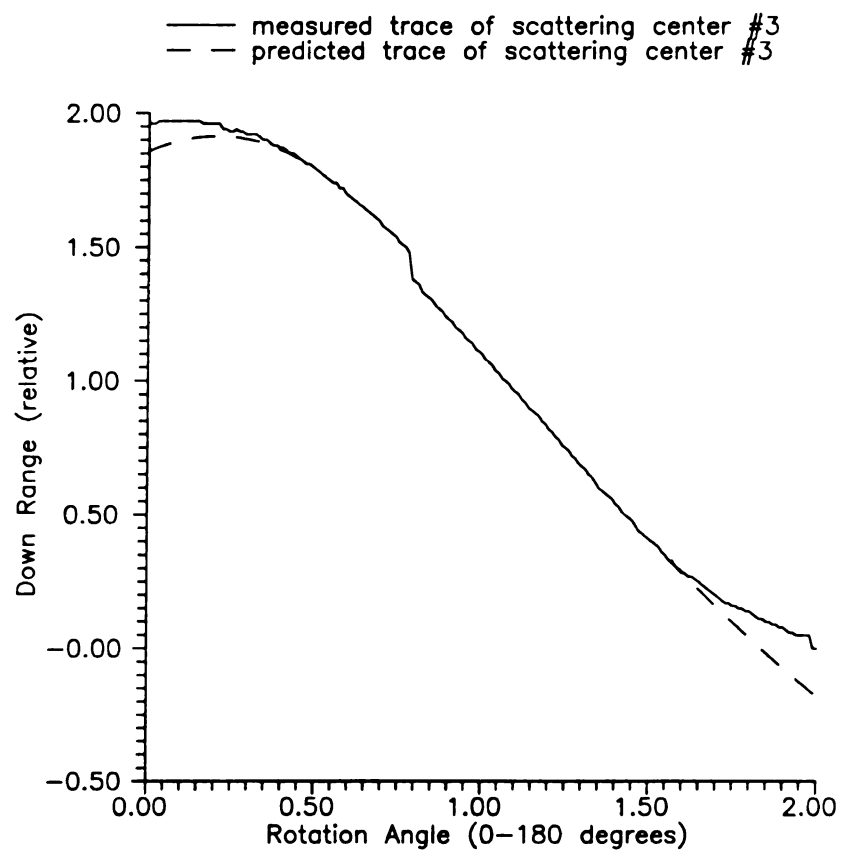
Figure 5.17 Measured and predicted positions of the tail of the TR-1 aircraft.
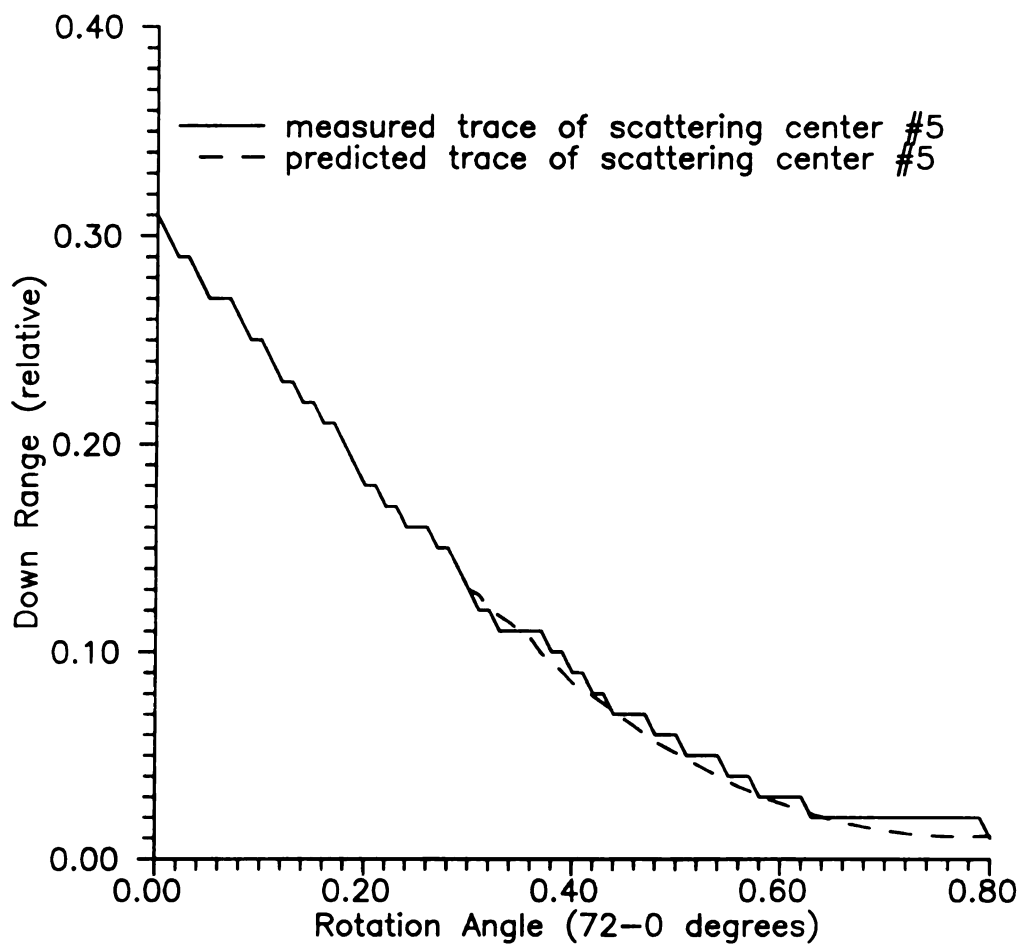
Figure 5.18 Measured and predicted positions of the engines of the TR-1.

111
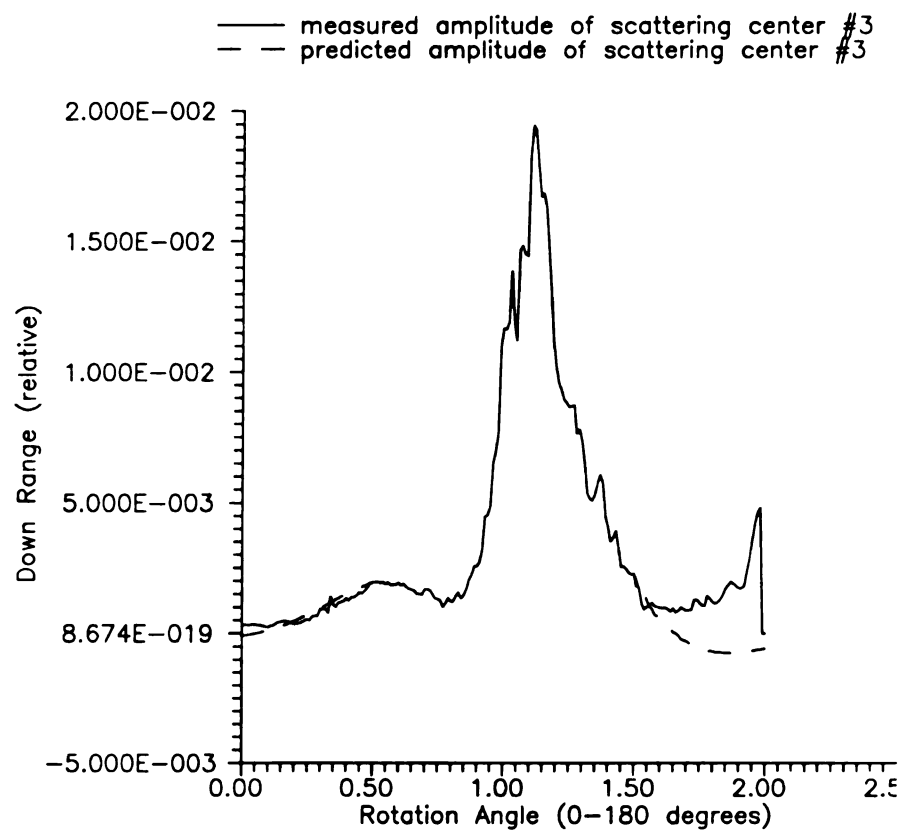
Figure 5.19 Measured and predicted amplitude of the scattered field in the positions of the tail of the TR-1.
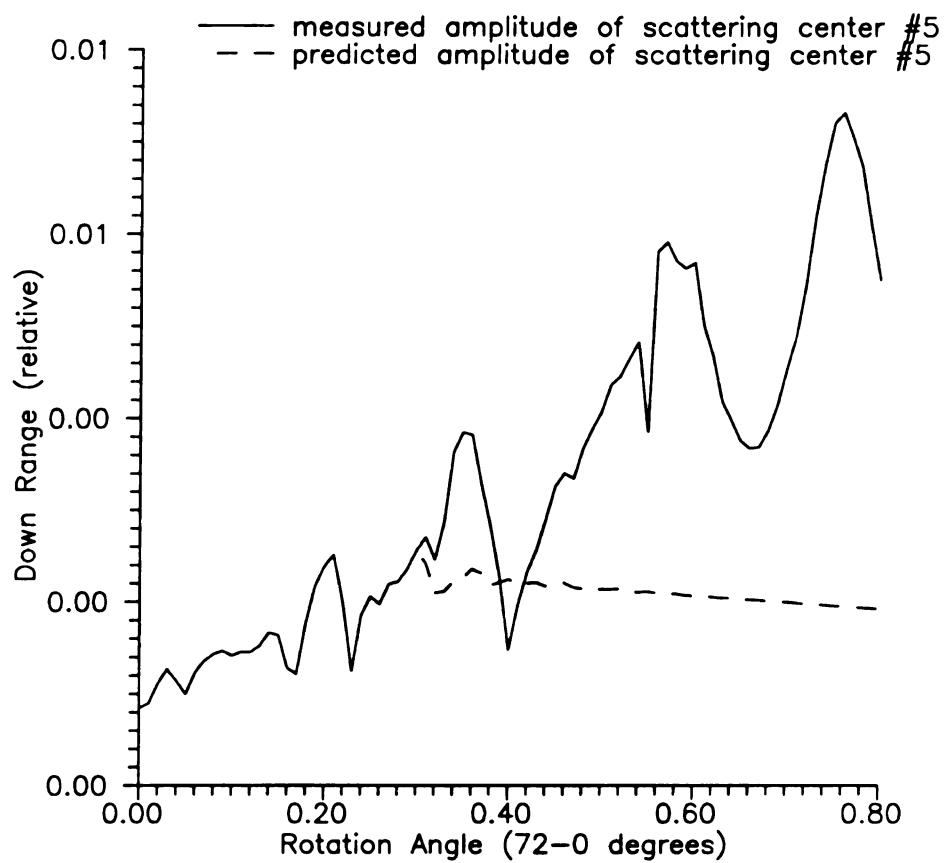
Figure 5.20 Measured and predicted amplitude of the scattered filed in the positions of the engines of the TR-1.
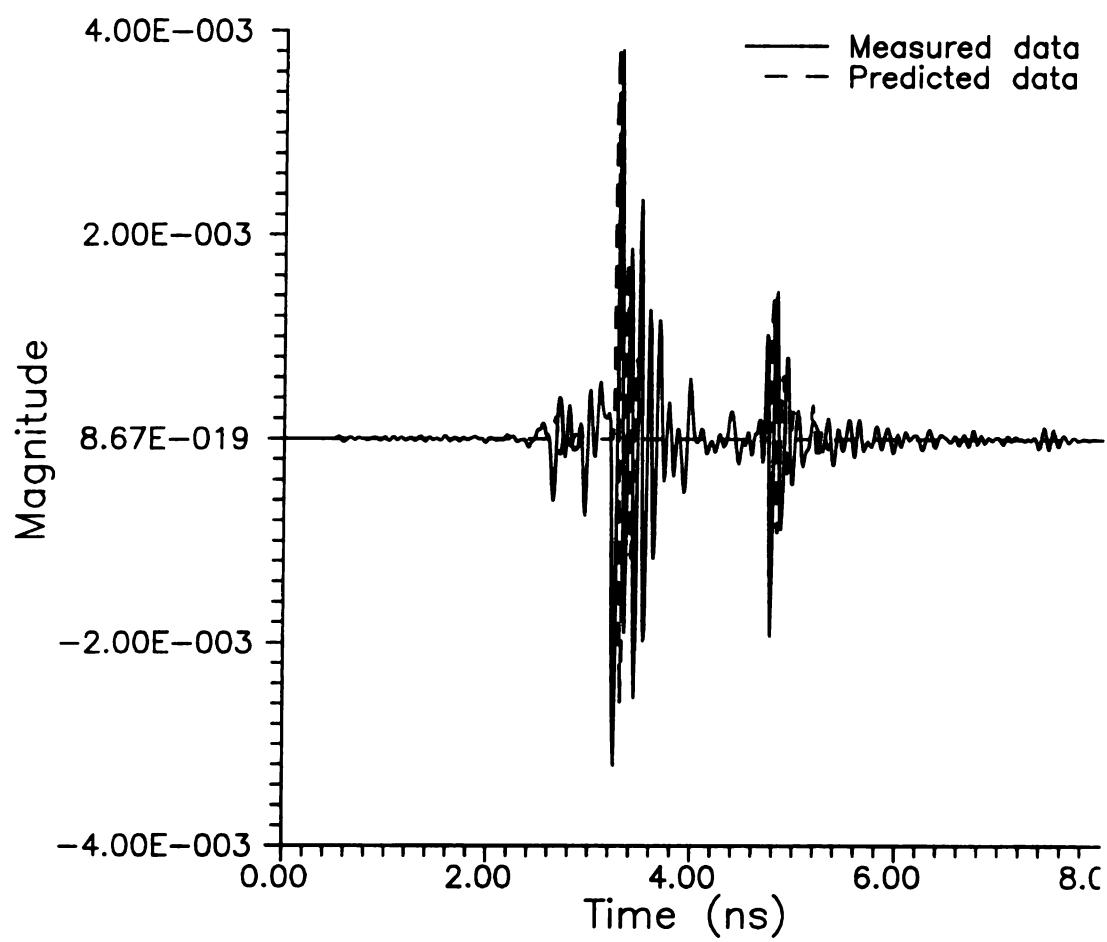
Figure 5.21   Measured and predicted data of the TR-1 for ϕ=40.5°.
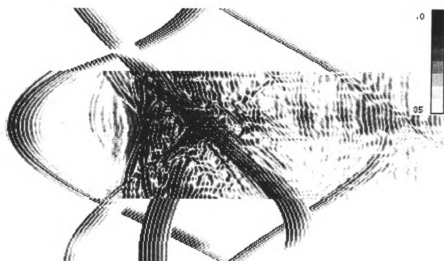
Figure 5.22 Restored sinogram of the TR-1 by linear prediction method.
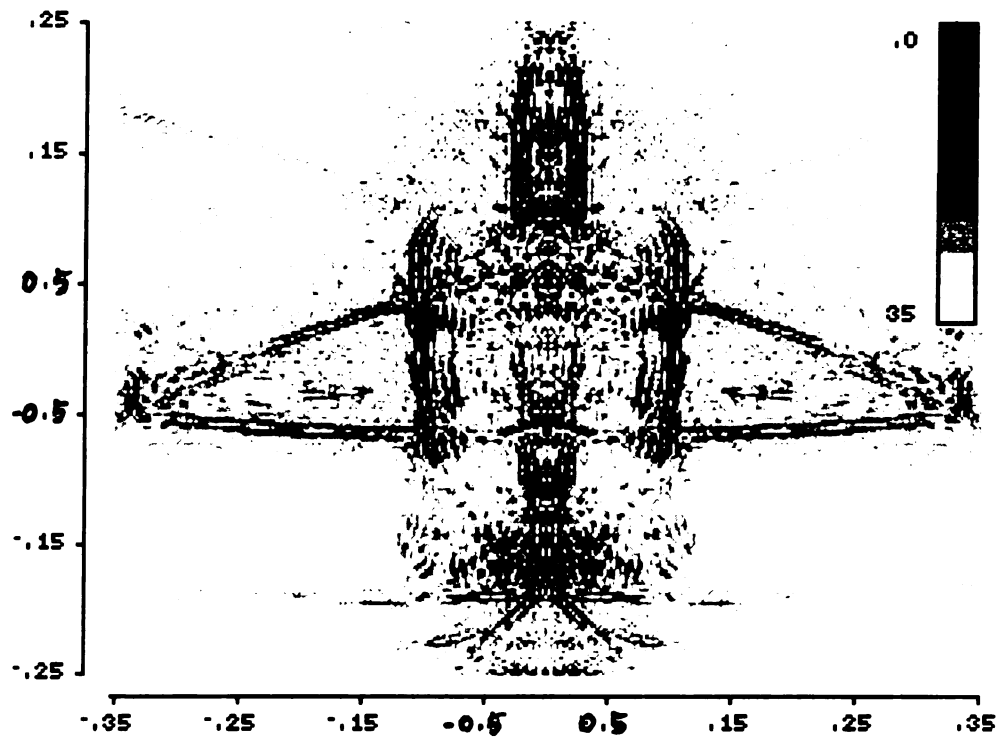
Figure 5.23 Image of the TR-1 using restored sinogram.

116
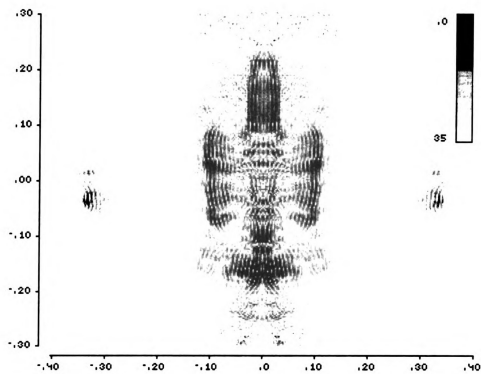
Figure 5.24 Image of the TR-1 from 45°-135° data using convolution backprojection algorithm.

117

CHAPTER 6

IMAGING UNDERSTANDING AND MODIFICATION USING

HIGH FREQUENCY APPROXIMATION METHODS

6.1 Introduction

Time-domain imaging is an imaging technique that uses the impulse response or

SMEP responses of the object to get the shapes or constitutive characteristics of the object

[31,10]. In the laboratory implementation of this imaging system, an object is seated on

a rotating pedestal and is illuminated by a plane wave. For each aspect angle a set of

pulses at different frequencies is transmitted and its echoes received. The object is then

rotated and the measurement is repeated to obtain the multiaspect stepped frequency

response of the scattering object. Each scattered field response is deconvolved using a 14

inch diameter sphere as a reference target, and inverse transformed into the time domain

using the FFT to provide a band-limited impulse response [10], or multiplied by the

SMEP window first and then inverse transformed into the time domain to get a SMEP

response [31].

In this time domain imaging technique, the physical optics approximation may be

used to model the scattering field of an aircraft [10, 31]. However, the PO approximation

is inadequate for scattering problems of a complex shaped conducting object such as an

aircraft. At high frequency, edge diffractions, multiple reflections, creeping waves, and

surface travelling waves may also be important scattering mechanisms [32], [53].

Additionally, the spectral and angular windows for data are usually restricted by practical constraints. Therefore, the time domain image of an aircraft may be different from its geometrical shape.

In this chapter, we will investigate time domain imaging of aircraft employing SMEP responses, and interpret the reconstructed image from a new approach, based on analysis of the scattering mechanisms and the back-projection algorithm utilized in image retrieval. In section 6.2 we will interpret the scattering mechanisms of aircraft using the ray method. The Explicit expression for equivalent currents, and the scattered fields from those currents are derived in section 6.3. The time-domain inverse scattering identity with the incorporation of Geometrical Theory of Diffraction (GTD) is derived in section 6.4. In section 6.5, we will compare the images of an object consisting of two plates using the PO approximation and GTD. Images of an aircraft model will be shown in Section 6.6.

6.2. Scattering Field Understanding Using Ray Method

Consider an aircraft illuminated by a source field from an initial reference surface A. The field from a source point p' at an observation point p can be tracked along a ray that passes through p and originates at point p'. It is possible that several rays pass through p as shown in Figure 6.1. In that event, the total field at p is synthesized by the sum of the fields reaching p along the various rays.

The field along a pencil of rays can be calculated from a knowledge of the initial field value and the ray geometry by [33]

$$u(\vec{r}) = u_A \sqrt{\frac{\rho_1^i \rho_2^i}{(\rho_1^i + s^i)(\rho_2^i + s^i)}} \, e^{-jks^i} \tag{6.1}$$
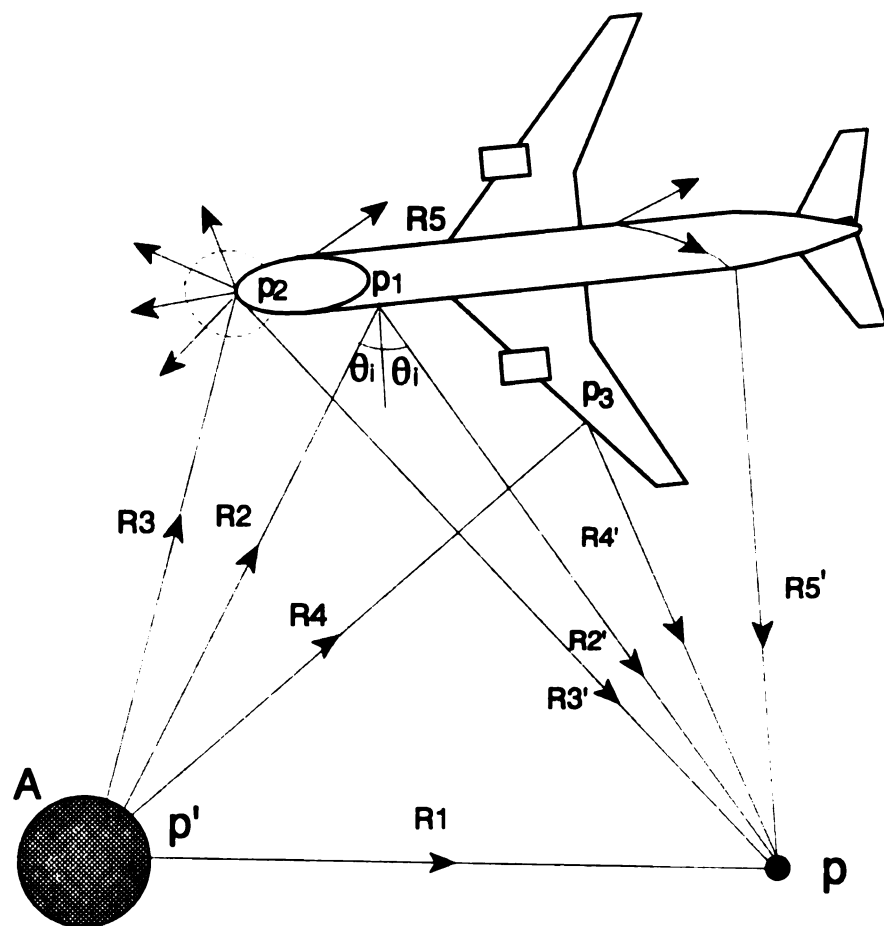
Figure 6.1   Scattering by an aircraft model (composite obstacle).

where ρ_1^i and ρ_2^i are the radii of curvature of the initial wavefront, s^i is the distance between the initial and the observation wavefront, and u_A is the initial field.

For the incident field in fig. 6.1 the initial values on A can be calculated from a known source distribution. The reflected field is caused by the incident rays (ray R2 in Fig. 6.1) reflected at the object surface. The reflected laws for the fields on a curved surface are the same as for plane waves on an infinite plane surface tangent to the curved surface at the point of impact of the incident ray (the canonical problem). Thus, the incident and reflection angles θ_i are equal. The initial value of the reflection field at p_I is given by the incident field at p_I multiplied by the plane wave reflection coefficient $R(\theta_i)$ descriptive of the reflecting properties of the boundary surface. The amplitude variation along ray $R2'$ involves the surface curvature at p_I, the curvature parameters for the incident wavefront, and the angle coordinates specifying the directions of the reflected and incident rays. Therefore, the reflected contribution to the field at p is given by

$$u_{2'} = u_2 R(\theta_i) \sqrt{\frac{\rho_1^r \rho_2^r}{(\rho_1^r + R_2')(\rho_2^r + R_2')}} e^{jkR_2'}$$

$$u_2 = u_{A2} \frac{e^{-jkR_2}}{kR_2}$$

(6.2)

where u_{A2} is the initial field for ray 2 on surface A.

The incident field along ray $R3$ striking the conical tip of the aircraft in Fig. 6.1 excites a spherical wave front and therefore a family of rays centered at the tip. The canonical problem for the tip diffracted field is that of a plane wave incident on an infinite conical obstacle. That solution provides the diffraction coefficient D^V, by which the incident ray field is modified upon emerging from the conical tip. Thus, the

contribution at p due to the field along ray $R3'$ is

$$u_{3'} = D^V \frac{e^{-jkR'_3}}{kR'_3} u_3, \qquad u_3 = u_{A3} \frac{e^{-jkR_3}}{kR_3} \qquad (6.3)$$

where u_{A3} is the initial field for ray $R3$ on surface A.

When an incident wave along ray $R4$ hits an edge of an aircraft wing, a family of diffracted rays is excited. Those rays must obey the *law of edge diffraction*. A diffracted ray and the corresponding incident ray make equal angles with the edge at the point of diffraction, provided that they are both in the same medium. They lie on opposite sides of the plane normal to the edge at the point of diffraction. When the two rays lie in different media, the ratio of the sines of the angles between the incident and diffracted rays and the normal plane is the reciprocal of the ratio of the indices of refraction of the two media. An edge-diffracted ray from a point P' to a point P is a curve which has stationary optical length among all curves from P' to P with one point on the edge (Fermat's principal for edge diffraction). The contribution at P due to the edge-diffracted wave along ray $R4'$ is [34]

$$u_{4'} = D^d \sqrt{\frac{\rho_1}{(\rho_1 + R_4)R_{4'}}} u_4, \qquad u_4 = u_{A4} \frac{e^{-jkR_4}}{kR_4} \qquad (6.4)$$

where D^d is the diffraction coefficient, u_{A4} is the initial field for ray $R4$ on surface A, and ρ_1 is the distance from the edge to the caustic of the diffracted rays.

Tip diffraction due to incident ray $R3$ also excites a diffracted surface ray (also called a creeping ray) that travels along a geodesic on the shadowed surface and sheds energy continuously. The launching amplitude L_s of a surface ray field and its amplitude

122

variation $M(R_s)$ along its geodesic path $R5$ are determined from the canonical problem. Therefore, the surface wave contribution to the field at p along ray $R5'$ is

$$u_{5'} = u_3 D_s M(R_s) e^{-jkR_s} L_s \frac{e^{-jkR_{s'}}}{kR_{s'}} \qquad (6.5)$$

where u_3 is given in (6.3), and R_s denotes the geodesic length along ray $R5$ from the tip to the shedding point p_4.

The total ray-optical field at point p in fig. 6.1 is now given by

$$u = u_1 + u_{2'} + u_{3'} + u_{4'} + u_{5'} \qquad (6.6)$$

where

$$u_1 = u_{AI} \frac{e^{-jkR_1}}{kR_1} \qquad (6.7)$$

denotes the field along the direct ray from the source. The remaining contributions, given by (6.2)-(6.5), are due to the presence of the scatterer.

The result in (6.6) contains only the dominant contribution from each of the ray fields. Generally, each ray field has, in addition to this leading term, a series of higher-order terms that decay inversely with k. Validity of the leading term alone implies that the higher-order terms, in particular the second term, are small in comparison with the first.

By the very construction of the field in (6.6), it is evident that the ray method decomposes a complicated composite scattering problem into a sequence of simpler canonical problem via the following steps:

(1)   Determination of the incident field over an initial surface A.

(2)   Determination of the reflected and diffracted ray fields that contribute at an observation point p.

(3)   Identification of canonical problems that treat separately each of the ray reflection and diffraction problems. The solutions of these problems furnish the initial amplitudes along various species of reflected and diffracted rays.

(4)   Synthesis of a composite scattering problem by interaction (along rays) between canonical constituents.

6.3.   High Frequency Approximation Methods

Diffraction problems of the type schematized in fig. 6.1 can be formulated in various ways. The second field generated by the induced surface currents can be represented in terms of the direct radiation from the elementary currents distributed over the aircraft surface A'.

In the illuminated region A' on a perfectly conducting object away from surface singularities (such as edges, tips, or corners) and from strongly curved regions (where the radius of curvature is not large compared to wavelength), one may approximate the induced surface currents by their "physical optics" values. The physical optics currents $\vec{J}_p$ are based on the local behavior of high-frequency fields described in the previous section and are taken at any point p on A' to have the same value as on an infinite perfectly conducting plane tangent to A' at p. Thus

$$\vec{J}_p(\vec{r}) = \begin{cases} 0 & \vec{r} \notin A' \\ 2\hat{n} \times \vec{H}^i(\vec{r}) & \vec{r} \in A' \end{cases} \tag{6.8}$$

where $\vec{H}^i$ is the incident vector magnetic field. The secondary field generated by the

124

physical optics current gives the correct geometric-optical reflected field and the diffracted field near the shadow boundaries. It does not provide, however, good results for the diffracted field away from the shadow boundaries.

Even on a smoothly curved convex object with large radius of curvature, the physical optics currents becomes invalid near the shadow boundaries. One may therefore attempt to add to $\vec{J}_p$ a correction $\vec{J}^f$, named the "fringe current" by Ufimtsev [35], so that the sum equals the exact current value. The correction term is due to all other effects not included in PO, such as edges. Because of the validity of the physical optics currents well inside the illuminated region, and away from edges or corners, the fringe currents are confined to the vicinity of those portions on A ' that lie near shadow boundaries or surface singularities.

6.3.1 Equivalent Edge Currents for Arbitrary Aspect of Observation

The method of equivalent currents is a powerful technique in the analysis of the scattering of electromagnetic fields. In addition to predicting the scattered fields in the direction of a caustic, the method allows us to calculate the diffracted fields from an edge of finite length and for observation angles away from the cone of diffracted rays. In the following section, we will introduce Michaeli's equivalent edge currents for arbitrary aspects of observation since his formula is more general and rigorous than those of other researchers [36].

According to the method of equivalent currents, the diffracted field $\vec{E}^d$ due to an edge discontinuity C is given for the Fresnel and far zones by the radiation integral [4]

$$\vec{E}^{d} \sim jk\int_{C}\left[ZI(\vec{r}')\hat{s}\times(\hat{s}\times\hat{t}) + M(\vec{r}')\hat{s}\times\hat{t}\right]G(\vec{r}',\vec{r})\,dl \qquad (6.9)$$

where k is the wavenumber of the incident wave, $Z=\sqrt{\mu/\varepsilon}$ is the impedance of the medium, ε and η are the permittivity and permeability of the medium, respectively, $\vec{r}$ and $\vec{r}'$ are the position vectors of the point of observation and a point on C, respectively, $dl = |\vec{dr}'|$ is the increment of arc length l along C; $\hat{t} = \vec{dr}'/dl$ is the tangent unit vector, $\hat{s} = \vec{s}/s = (\vec{r}-\vec{r}')/|\vec{r}-\vec{r}'|$ is the direction of observation of the radiating edge element at $\vec{r}'$, $G(\vec{r}',\vec{r}) = \exp(-jks)/4\pi s$ is the 3-D Green's function, and $\vec{I}(\vec{r}') = I(\vec{r}')\hat{t}$ and $\vec{M}(\vec{r}') = M(\vec{r}')\hat{t}$ are the electric and magnetic equivalent currents respectively.

Consider a plane electromagnetic wave propagating in the $\hat{s}'$ direction and incident on a perfectly conducting infinite wedge with an exterior angle $N\pi$, $0<N<2$. Our aim is to obtain explicit expressions for I and M at a point O on the edge for an arbitrary direction of observation $\hat{s}$. The geometry of the problem is depicted in Fig. 6.2. The point O in question is chosen as the origin. The x axis is directed along the normal to the edge, and the y axis coincides with the external normal to the face. The z axis is directed along the edge, so as to form a right-hand system. The angles between the $\hat{s}$ and $\hat{s}'$ directions and the edge are

$$\beta = \cos^{-1}(\hat{s}\cdot\hat{z}), \qquad \beta' = \cos^{-1}(\hat{s}'\cdot\hat{z}) \qquad (6.10)$$

The angle between the "upper" face and the edge-fixed plane of incidence containing the vectors $\hat{s}'$ and $\hat{z}$ is ϕ'. The corresponding angle for the edge-fixed plane

126
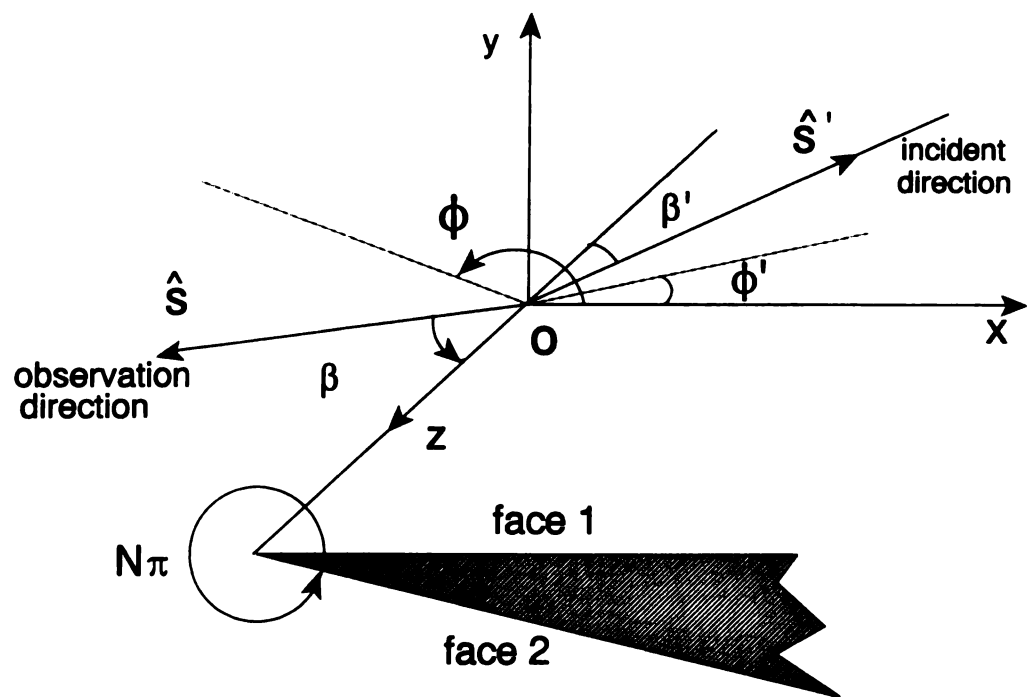
Figure 6.2   Wedge scattering geometry.

of observation is ϕ.

The expressions for I and M are given by [36]

$$M = H_{z0}^i \frac{2jZ(1/N)}{k\sin\beta\sin\beta'} \left\{ \frac{\sin\phi}{\sin\alpha_1} \frac{\sin[(\pi-\alpha_1)/N]}{\cos[(\pi-\alpha_1)/N]-\cos(\phi'/N)} + \frac{\sin(N\pi-\phi)}{\sin\alpha_2} \frac{\sin[(\pi-\alpha2)/N]}{\cos[(\pi-\alpha_2)/N]+\cos(\phi'/N)} \right\}$$

$$I = -E_{z0}^i \frac{2jY(1/N)\sin(\phi'/N)}{k\sin^2\beta'} \left\{ \frac{1}{\cos[(\pi-\alpha_1)/N]-\cos(\phi'/N)} + \frac{1}{\cos[(\pi-\alpha_2)/N]+\cos(\phi'/N)} \right\}$$

$$-H_{z0}^i \frac{2j(1/N)}{k\sin\beta'} \cdot \left\{ \frac{\mu_1\cot\beta'-\cot\beta\cos\phi}{\sin\alpha_1} \frac{\sin[(\pi-\alpha_1)/N]}{\cos[(\pi-\alpha_1)/N]-\cos(\phi'/N)} \right.$$

$$\left. -\frac{\mu_2\cot\beta'-\cot\beta\cos(N\pi-\phi)}{\sin\alpha_2} \frac{\sin[(\pi-\alpha_2)/N]}{\cos[(\pi-\alpha_2)/N]+\cos(\phi'/N)} \right\}$$

(6.11)

where $\alpha_1 = \cos^{-1}\mu_1$, $\mu_1 = \sin\beta\cos\phi/\sin\beta'$, $Y=1/Z$, $\mu_2 = \sin\beta\cos(N\pi-\phi)/\sin\beta'$, and

$\alpha_2 = \cos^{-1}\mu_2$. In another paper [37], Michaeli shows that I and M can be split into PO

components and fringe components

$$I = I^{PO}+I^f, \qquad M = M^{PO}+M^f \qquad (6.12)$$

where the PO components are the contribution from the surfaces, while the fringe

components are the contribution from the edge. The fringe components for an edge in a

half plane are [37]

$$I^f = E_{z0}^i \frac{2jY}{k\sin^2\beta'} \frac{\sqrt{2}\sin(\phi'/2)}{\cos\phi'+\mu}[\sqrt{1-\mu}-\sqrt{2}\cos(\phi'/2)]+H_{z0}^i \frac{2j}{k\sin\beta'} \frac{1}{\cos\phi'+\mu}$$

$$\cdot \left[\cot\beta'\cos\phi'+\cot\beta\cos\phi+\sqrt{2}\cos(\phi'/2)(\mu\cot\beta'-\cot\beta\cos\phi)(1-\mu)^{-\frac{1}{2}} \right] \qquad (6.13)$$

$$M^f = H_{z0}^i \frac{2jZ\sin\phi}{k\sin\beta\sin\beta'} \frac{1}{\cos\phi'+\mu}\left[1-\frac{\sqrt{2}\cos(\phi'/2)}{\sqrt{1-\mu}} \right]$$

where

$$\mu = \left[\sin\beta'\sin\beta\cos\phi + \cos\beta'\cos\beta - \cos^2\beta'\right]/\sin^2\beta' \qquad (6.14)$$

6.3.2 Scattered Field from Equivalent Fringe Currents of a Finite Edge

The far-zone radiation field maintained by the equivalent sources of an edge with finite length L in the edge-fixed coordinate system is given by [38]

$$\vec{E} = -j\omega\vec{A}_T + \frac{jk}{\epsilon}\hat{r}\times\vec{F} \qquad \vec{H} = (\hat{r}\times\vec{E})/\eta \qquad (6.15)$$

where $\eta = \omega\mu/k$ and

$$\vec{A}_T(\vec{r}) = \frac{\mu}{4\pi}\frac{e^{-jkr}}{r}\vec{a}_T(\theta,\phi), \qquad \vec{F}(\vec{r}) = \frac{\epsilon}{4\pi}\frac{e^{-jkr}}{r}\vec{\mathscr{F}}_T(\theta,\phi) \qquad (6.16)$$

where

$$a_{\theta'}(\theta',\phi') = \oint_s\left[\cos\theta'\cos\phi'I_{x'}(\vec{r}') + \cos\theta'\sin\phi'I_{y'}(\vec{r}') - \sin\theta'I_{z'}(\vec{r}')\right]e^{jk\hat{r}\cdot\vec{r}'}ds$$

$$= -\int_{-L/2}^{L/2}\sin\theta'I_{z'}(\vec{r}')e^{jk\hat{r}\cdot\vec{r}'}dr'$$

$$a_{\phi'}(\theta',\phi') = \oint_s\left[-\sin\phi'I_{x'}(\vec{r}') + \cos\phi'I_{y'}(\vec{r}')\right]e^{jk\hat{r}\cdot\vec{r}'}ds' = 0$$

$$\qquad (6.17)$$

$$\mathscr{F}_{\theta'}(\theta',\phi') = \oint_s\left[\cos\theta'\cos\phi'M_{x'}(\vec{r}') + \cos\theta'\sin\phi'M_{y'}(\vec{r}') - \sin\theta'M_{z'}(\vec{r}')\right]e^{jk\hat{r}\cdot\vec{r}'}ds'$$

$$= -\int_{-L/2}^{L/2}\sin\theta'M_{z'}(\vec{r}')e^{jk\hat{r}\cdot\vec{r}'}dr'$$

$$\mathscr{F}_{\phi'}(\theta',\phi') = \oint_s\left[-\sin\phi M_{x'}(\vec{r}') + \cos\phi'M_{y'}(\vec{r}')\right]e^{jk\hat{r}\cdot\vec{r}'}ds' = 0$$

Choosing the local phase reference to be at the center of the wedge and assuming

the equivalent currents are constants over the length of the wedge, (6.17) reduces to

$$a_\theta(\theta',\phi') = -\int_{-L/2}^{L/2}\sin\theta' I_z(\vec{r}')e^{j\vec{k}\cdot\vec{r}'}dr' = -I(0)\sin\theta'\int_{L/2}^{L/2}e^{j2k\xi\cos\theta'}d\xi$$

$$= -I(0)L\sin\theta' sinc(kL\cos\theta') \qquad (6.18)$$

$$\mathcal{F}_{\theta'}(\theta',\phi') = -\int_{L/2}^{L/2}\sin\theta' M_{z'}(\vec{r}')e^{j\vec{k}\cdot\vec{r}'}dr' = -M(0)L\sin\theta' sinc(kL\cos\theta')$$

where $sinc(x) = \sin(x)/x$. From (6.15)-(6.18), the backscattered field can be express as

$$\vec{E}(\vec{r}) = -j\omega A_t + \frac{jk}{\epsilon}\hat{r}\times\vec{F} = j\omega\mu_0 L sinc(kL\cos\theta')\sin\theta'\frac{e^{-jkr}}{4\pi r}\left[I(0)\hat{\theta}' - \frac{M(0)}{\eta}\hat{\phi}'\right]$$

$$\vec{H}(\vec{r}) = \frac{\hat{r}\times\vec{E}}{\eta} = jkL sinc(kL\cos\theta')\sin\theta'\frac{e^{-jkr}}{4\pi r}\left[I(0)\hat{\phi}' + \frac{M(0)}{\eta}\hat{\theta}'\right] \qquad (6.19)$$

At a specific aspect, the contribution to the total backscattered field from the wedge diffraction in time-domain is obtained by Fourier Transforming the frequency response.

6.4 Time-Domain Inverse Scattering Identity with The Incorporation of Edge Diffractions

The time-domain inverse scattering identity based on the Radon transform and the space-time magnetic field integral equation has been derived for real-time use in short pulse radar systems in chapter 3. In that formula, even though the correction term has been added to the PO term, the contributions from the correction term is hard to evaluate for a complex scatterer. Here we will investigate a new approach. Since the physical optics currents work well inside the illuminated region, and away from edges or corners, the fringe currents are confined to the vicinity of those surface singularities and shadow

boundaries. Because there are big diffractions from the edges of an aircraft, we only add the edge fringe currents to the PO currents in the inverse scattering identity.

For an aircraft, there may be several edges which contribute to the diffraction field. To a first order approximation, the diffraction field can be considered as a summation of the contributions from each "visible" edge. Thus, For N "visible" edges, the total diffracted field is given by

$$\vec{H}^d(\vec{r}) = \sum_{i=1}^{N} jkL_i sinc(kL_i cos\theta_i') sin\theta_i' \frac{e^{-jkr_i}}{4\pi r_i}\left[I_i^f(0)\phi_i' + \frac{M_i^f(0)}{\eta}\theta_i'\right] \qquad (6.20)$$

The SMEP diffraction response is obtain by multiplying the frequency response (6.20) by the SMEP window $Q(\omega)$, and then inverse transforming into the time-domain using the FFT as

$$h^d(\vec{r}_s,t) = \mathscr{F}^{-1}\left(Q(\omega)\vec{H}^d(\vec{r}_s)\cdot\hat{h}^i\right) \qquad (6.21)$$

where $\hat{h}^i$ denotes the polarization direction of the incident magnetic field. The far-zone backscattered field can be written as

$$h^s(\vec{r},t) = \frac{1}{2\pi r}\int_s \hat{n}'\cdot\hat{r}\frac{\partial h^i(\vec{r}',\tau)}{\partial\tau}A(\hat{r},\hat{n})ds' + h^d(\vec{r},t) \qquad (6.22)$$

The first term of the right hand side in (6.22) represents the contribution from the PO currents, while the second term of the right hand side denotes the contribution from the diffraction fringe currents. Assuming the incident magnetic field is a SMEP, the same procedure can be applied as in chapter 3 and the "thickness function" of the target in the z-direction can be written as

131

$$\Gamma(\bar{\rho}') = -\frac{2\rho}{\pi\omega_c}\int_0^{2\pi}\int_{-\infty}^{\infty}\left\{\left[2\alpha^2+2\alpha\frac{\partial}{\partial t}\right][h^s(\bar{\rho}',t)-h^d(\bar{\rho}',t)]\right.$$

$$\left.+(\omega_c^2+\alpha^2)\int_0^t[h^s(\bar{\rho}',t)-h^d(\bar{\rho}',t)]dt\right\}\frac{dt\,d\phi^i}{t-2\rho+2\rho'\cos(\phi'-\phi^i)}$$

(6.23)

This is the complete solution to the two-dimensional problem of recovering a body from its scattered field; it requires the scattered fields and the diffraction terms from all possible directions in the x-y plane. The next step is to solve equation (6.23). We can first neglect the diffraction terms in (6.23). This is the time domain physical optics inverse problem. We can thus obtain an initial estimate of $\Gamma_1(\bar{\rho})$, then find all the edges of the image and use (6.20) to evaluate the total edge diffracted field $h^d(\bar{r},t)$. Finally, $h^d(\bar{r},t)$ is added to (6.23) to obtain the modified $\Gamma(\bar{\rho})$.

6.5   Images of an Object Consisting of Conducting Plates

Consider an object consisting of two conducting plates placed on a rotating pedestal as illustrated in Figure 6.3. Points P_1 and P_2 are two vertices of one plate and the line P_1P_2 forms an edge of the plate. In the laboratory coordinate system, define the z-axis as the direction of the rotational axis, and the x-axis to be in the observation direction. At the starting angle, the polar coordinates of the end points P_1 and P_2 are (r_1, θ_1, ϕ_1) and (r_2, θ_2, ϕ_2), respectively. As the plate is rotated with an angle ϕ, the coordinates of P_1 and P_2 become $(r_1, \theta_1, \phi_1+\phi)$ and $(r_2, \theta_2, \phi_2+\phi)$, respectively.

Next we define an edge-fixed coordinate for edge P_1P_2 of the object. Let the z'-axis be in the direction of the edge P_1P_2, and the x'-axis be normal to the edge and lying
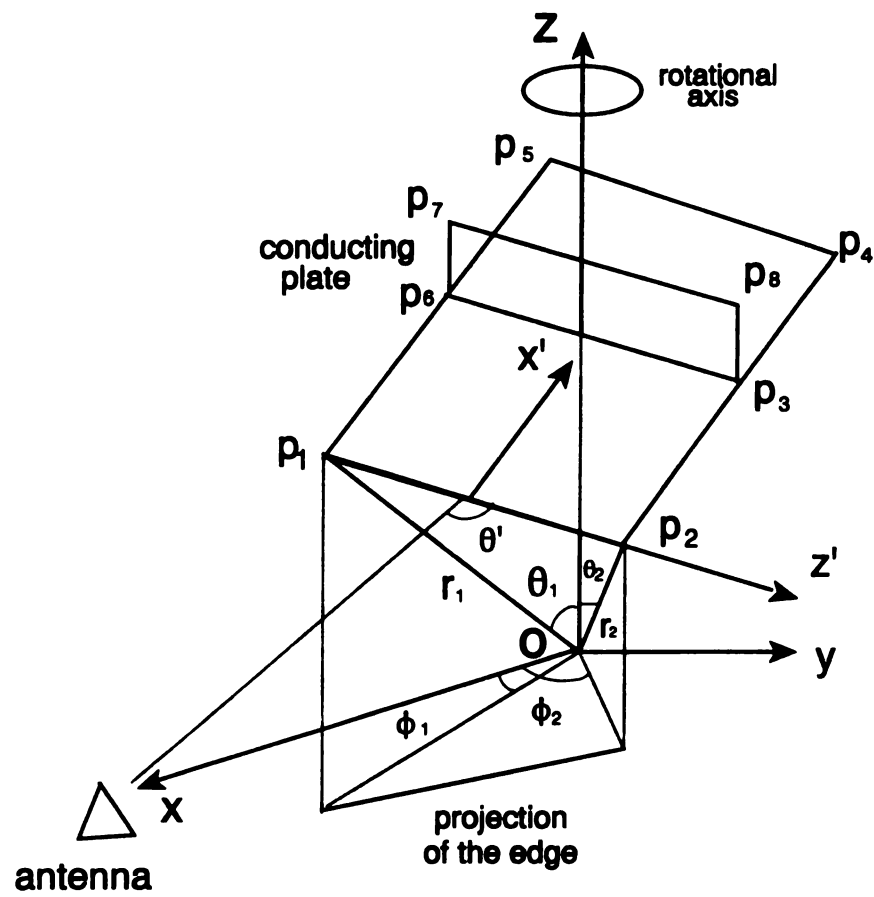
Figure 6.3 Geometry of a conducting plate in the laboratory coordinate system and edge-fixed coordinate system.

133

on the plate surface. The corresponding inclination angle of the transmitter/receiver to the edge-fixed coordinate system is θ' (φ=0°). As the plane is rotated through an angle φ, the corresponding inclination angle for the edge-fixed coordinate system becomes θ'(φ). It is noted that θ' is not only a function of φ, but also a function of the orientation of the plate and the edge.

Assuming that the transmitting and the receiving antennas are inside the x'-z' plane such that θ=π-θ' (β=π-β' in (6.13)), for the backscattered case. In our laboratory system, let the polarization direction of the electrical field be along the y-axis, and the polarization direction of the magnetic field be along the z-axis. In the following part, we calculate the edge diffracted field and the PO field of the object and compare the images of the object with and without the incorporation of edge diffractions.

6.5.1 Edge Diffracted Field

There are a total of eight vertices of the object which form eight edges of the object. The equivalent edge electric and magnetic currents for each edge have different forms depending on orientation and wedge angle. For edges P_1P_2, P_2P_4, P_4P_5 and P_5P_1, the equivalent currents will have similar formulas in their own edge-fixed coordinate systems. Since $\phi = \phi' = 180°$ and $H_{z0}^i = 0$, from (6.13) we have

$$I_i^f(0) = -E_{z0}^i \frac{jY2\sqrt{2}}{k\sin^2\theta_i\sqrt{1-\mu_i}} \qquad M_i^f(0) = 0 \qquad i=1,2,3,4 \qquad (6.24)$$

where $\mu_i = -1-2\cot^2\theta_i$. The incident field at the center o of the edge is

$$\bar{E}^i(0) = E_0 e^{-jk0}\hat{\theta}_i = E_0[\hat{x}_i\cos\theta_i\cos\phi_i+\hat{y}_i\cos\theta_i\sin\phi_i-\hat{z}_i\sin\theta_i] \qquad (6.25)$$

Then (6.24) becomes

134

$$I_i^f(0) = -E_{z0}^i \frac{jY2\sqrt{2}}{k\sin^2\theta_i\sqrt{1-\mu_i}} = E_0\sin\theta_i \frac{jY2\sqrt{2}}{k\sin^2\theta_i\sqrt{2+2\cot^2\theta_i}} = \frac{j2E_0}{\omega\mu} \qquad (6.26)$$

Substituting (6.26) into (6.19) yields the total diffraction fields from these four edges

$$E_\theta^{1-4}(\bar{r}) = -2E_o\sum_{i=1}^{4} \frac{e^{-jkr_i}}{4\pi r_i}L_i\sin\theta_i sinc(kL_i\cos\theta_i)$$

$$H_\phi^{1-4}(\bar{r}) = -\frac{2E_0}{\eta}\sum_{i=1}^{4} \frac{e^{-jkr_i}}{4\pi r_i}L_i\sin\theta_i sinc(kL_i\cos\theta_i) \qquad (6.27)$$

For edges P_6P_7 and P_3P_8, since $\theta = \theta' = 90^o$, $\mu = \cos\phi$, and the equivalent current can

be written as

$$I^f(0) = 0 \qquad M^f(0) = E_o\frac{j}{k}\frac{\sin\phi-1}{\cos\phi} \qquad (6.28)$$

Thus, the total diffraction fields from edges P_6P_7 and P_3P_8 are (in edge-fixed coordinates)

$$E_\phi^{5-6}(\bar{r}) = \sum_{i=5}^{6}L_i\frac{e^{-jkr_i}}{4\pi r_i}\frac{\sin\phi_i-1}{\cos\phi_i} \qquad H_\theta^{5-6}(\bar{r}) = \frac{1}{\eta}\sum_{i=5}^{6}L_i\frac{e^{-jkr_i}}{4\pi r_i}\frac{\sin\phi_i-1}{\cos\phi_i} \qquad (6.29)$$

For edge P_6P_3, $\phi=\phi'=0$ or 90°. From (6.11) we have $I(0)=0$, $M(0)=0$, so there is no

contribution from edge P_6P_3. For edge P_7P_8, $\phi=90^o$, $\mu=-2\frac{\cos^2\beta}{\sin^2\beta}$. From (6.13) we have

$$I^f(0) = -E_0\frac{jY}{k}\frac{\sqrt{1+\cos^2\theta}-\sin\theta}{\cos^2\theta} \qquad M^f(0) = 0$$

The diffracted field from edge P_7P_8 is

$$E_\theta^8(\bar{r}) = E_0L_8\frac{e^{-jkr_8}}{r_8}sinc(kL_8\cos\theta_8)\sin\theta_8\frac{\sqrt{1+\cos^2\theta_8}-\sin\theta_8}{\cos^2\theta_8} \qquad H_\phi^8(\bar{r}) = \frac{E_\theta^8(\bar{r})}{\eta} \quad (6.31)$$

135

The total diffraction fields from this object can be considered as a summation of the contributions from each "visible" edge. Thus, the total diffracted field is given by

$$E_\theta^d(\vec{r}) = -2E_o\sum_{i=1}^{4} \frac{e^{-jkr_i}}{4\pi r_i}L_i\sin\theta_i sinc(kL_i\cos\theta_i) + E_0\sum_{i=5}^{6} L_i\frac{e^{-jkr_i}}{4\pi r_i}\frac{\sin\phi_i - 1}{\cos\phi_i}$$

$$+ E_0 L_8\frac{e^{-jkr_8}}{4\pi r_8}sinc(kL_8\cos\theta_8)\sin\theta_8\frac{\sqrt{1+\cos^2\theta}-\sin\theta_8}{\cos^2\theta_8}$$

(6.32)

Equation (6.32) can be used to obtain the frequency responses over the finite bandwidth 4-16GHz, multiplied by a SMEP window, and then inverse transformed into the time-domain using the FFT to provided a SMEP response. Figure 6.4 shows the diffracted SMEP response of the object at $\phi=45°$ using the SMEP shown in Fig 4.4. The response shows that there are two peaks located at range about $\pm(L_i/2)\cos\theta_i$ for each edge, which are at the differential ranges of the end points of the edge. At the rotation angle ϕ such that $\theta_i = 90°$, as shown in Fig. 6.5, the SMEP response gives a single peak with strong amplitude for each visible edge because the two end points of the edge have the same differential ranges and all the points on the edges are equidistant to the observation point.

6.5.2 Scattering Field Under Physical Optics Approximations

Consider the same object illuminating by a plane wave defined by

$$\vec{E}^i(\vec{r}) = \hat{e}E_o e^{-j\vec{k}^i\cdot\vec{r}} \qquad \vec{H}^i(\vec{r}) = \frac{\hat{k}^i\times\hat{e}}{\eta}E_o e^{-j\vec{k}^i\cdot\vec{r}}$$

(6.33)

The far-zone scattered field can be written as

$$\vec{E}^{s}(\vec{r}) = j\frac{\eta k}{4\pi}\frac{e^{-jkr}}{r}\hat{r}\times(\hat{r}\times\vec{a}) \qquad (6.34)$$

where $\vec{a}(\vec{r}) = \int_{s}\vec{J}(\vec{r}')e^{-jk\hat{r}\cdot\vec{r}'}ds'$ is the directional weighting function. Using the PO

approximation, the induced current can be written as (in the illuminating region)

$$\vec{J}(\vec{r}) \approx 2\hat{n}(\vec{r}')\times\vec{H}^{i}(\vec{r}') \qquad (6.35)$$

Rewrite the scattered field as

$$\vec{E}_{p}^{s}(\vec{r}) = \hat{e}j\frac{E_{o}}{2\pi}\frac{e^{-jkr}}{r}\int_{s}\hat{r}\times(\hat{r}\times[\hat{n}\times(\vec{k}^{i}\times\hat{e})])e^{-j2\vec{k}^{i}\cdot\vec{r}'}ds' \qquad (6.36)$$

For the backscatter case, $\hat{r} = -\hat{k}^{i}$, and

$$\hat{r}\times(\hat{r}\times[\hat{n}\times(\vec{k}^{i}\times\hat{e})]) = -\hat{k}^{i}\times[(\hat{k}^{i}\times\hat{e})(\hat{n}\cdot\vec{k}^{i})] = \hat{e}(\hat{n}\cdot\vec{k}^{i}) \qquad (6.37)$$

so

$$\vec{E}_{p}^{s}(\vec{r}) = \hat{e}j\frac{E_{o}}{2\pi}\frac{e^{-jkr}}{r}\int_{s}\hat{n}'\cdot\vec{k}^{i}e^{-j2\vec{k}^{i}\cdot\vec{r}'}ds' = -\hat{\theta}j\frac{E_{o}}{2\pi}\frac{e^{-jkr}}{r}\int_{s}k\cos\theta e^{j2k\sin\theta}ds$$

$$= -\hat{\theta}j\frac{kE_{o}L_{5}L_{8}}{2\pi}\frac{e^{-jkr}}{r}\cos\theta sinc(kL_{8}\sin\theta) \qquad (6.38)$$

where L_{5} and L_{8} are the lengths of edge $P_{6}P_{7}$ and edge $P_{7}P_{8}$.

Fig. 6.6 and Fig. 6.7 show the numerical SMEP responses of the object at two different angles. The response shows that there are two peaks located at range about $\pm(L_{5}/2)\cos\theta_{i}$ for each horizontal edge which are at the differential ranges of the end points of the edge. At the rotation angle $\phi = 0°$, as shown in Fig. 6.6, the SMEP response gives a single peak with strong amplitude for the vertical plate because all the points on the

137

plate have the same differential ranges and are equidistant to the observation point.

6.5.3 Images of The Plates

The total scattered fields of the plates can be considered as the combination of the edge diffracted field and the PO scattered field. They can be written as

$$\vec{E}^{s}(\vec{r}) = \vec{E}_{p}^{s}(\vec{r}) + \vec{E}_{d}(\vec{r}) \tag{6.39}$$

where $\vec{E}_{p}(\vec{r})$ denotes the PO scattered field and $\vec{E}_{d}(\vec{r})$ denotes the total edge diffracted field. Substituting (6.39) into (6.23) without subtracting the edge diffracted field we may create the image of the plates. This is usually the practical case since the measured field is usually the total field, and the edge diffracted field is very difficult to obtain for a complicated target. Figure 6.8 gives the image of the plates shown in fig. 6.3. We can see they match very well. Because equation (6.23) is derived under the PO approximation, we may use the PO scattered field in (6.23). This gives the true image of the plates under the PO approximation. The image is given in Fig 6.9. Comparing with Fig 6.8, we can see that the PO approximation is inadequate for an object consisting of conducting plates where the edge diffractions may be the dominant contributors to the scatted field. Thus, the image of a metallic object might be different from its geometrical shape using the PO approximation.

6.6 Images of an Aircraft Model

A simulation of time-domain imaging is carried out using data measured in the Michigan State University free-field scattering range. We use the same measured data as used in chapter 4. Figure 6.10 show the images of a 1:72 scale model B-52 aircraft. Since

we use the PO approximation in (6.23), and did not subtract the diffraction contribution, the edges of the aircraft are clearly visible, and the surface contribution nearly neglectable compared to the edge diffraction. This shows that edge diffractions are dominant contributors to the scattered field when the scatterers consist of conducting plates. Next, we can obtain the edges from Fig. 6.10 and use (6.20) to evaluated the total edge diffracted field from all the "visible edges". Fig 6.11 shows the image of the main edges of the aircraft model. Subtracting the edge diffraction field from the total measured scattered field yields the PO component and the corresponding image is shown in Fig. 6.12. We can see that the wing edges are not as visible as in Fig. 6.10. Theoretically, the wings should vanish after subtracting the edge diffracted fields, but since the scattered field oscillates at high frequency, and the diffraction field from surface singularities such as tips, corners, and multiple reflections, creeping waves and surface travelling waves are not taken into account and they may also be big contributors to the scattered fields. Since they may also distort the reconstructed image, the results are not as good as expected.

6.7   Conclusions

In this chapter, we have shown that in the high-frequency region, the scattered field can be attributed to a combination of different canonical problems. This idea has been used in developing a new time-domain inverse scattering identity and interpreting the reconstructed image from a new approach, based on analysis of the scattering mechanisms and the backprojection algorithm utilized in image retrieval. In this approach, we added the edge diffracted field to the physical optics field so that the total is equal to the exact scattered field value. We also showed that for those objects consisting of conducting plates, edge diffractions are dominant contributors to the scattered field. The

139

total edge diffracted field is the summation of the diffracted field from each "visible" edge. Several numerical and experimental examples have been included to validate the formulas developed in this chapter.
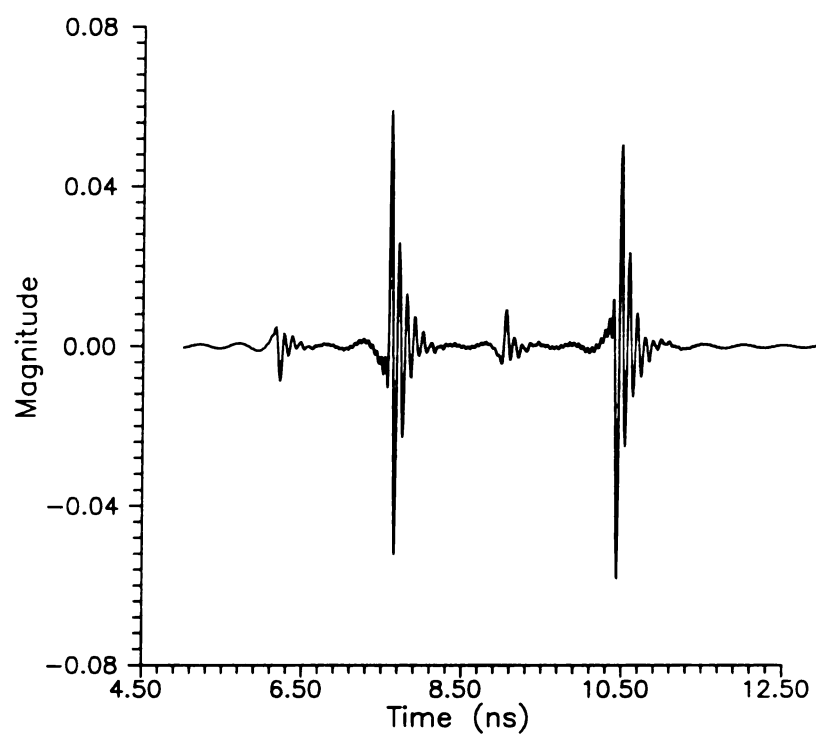
Figure 6.4   Diffracted SMEP response of the object with rotational angle $\phi=45°$.
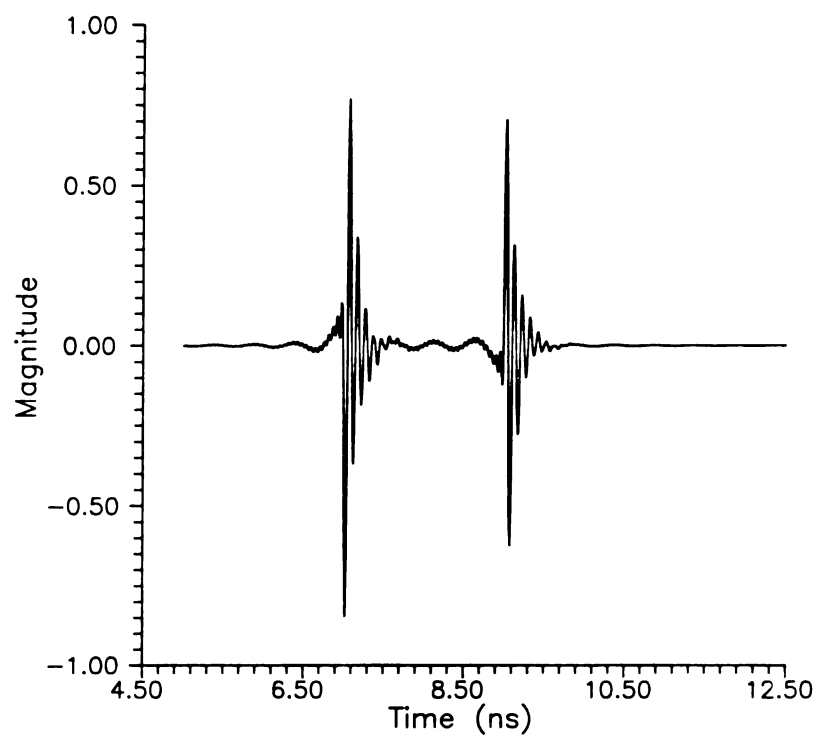
Figure 6.5 Diffracted SMEP response of the object with rotational angle φ=0°.
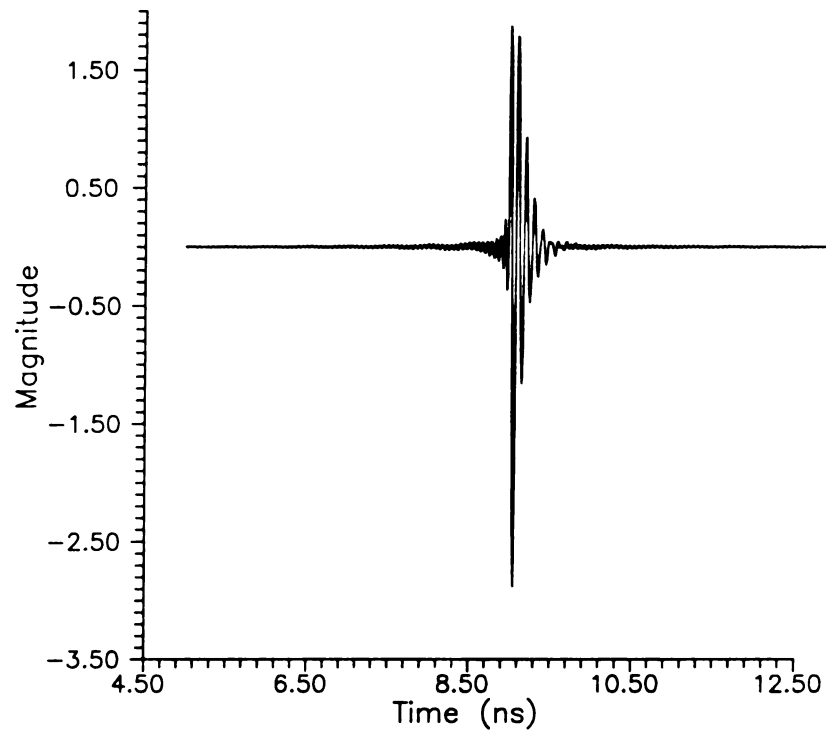
Figure 6.6 SMEP response of the object with rotational angle $\phi=0°$ under PO approximation.
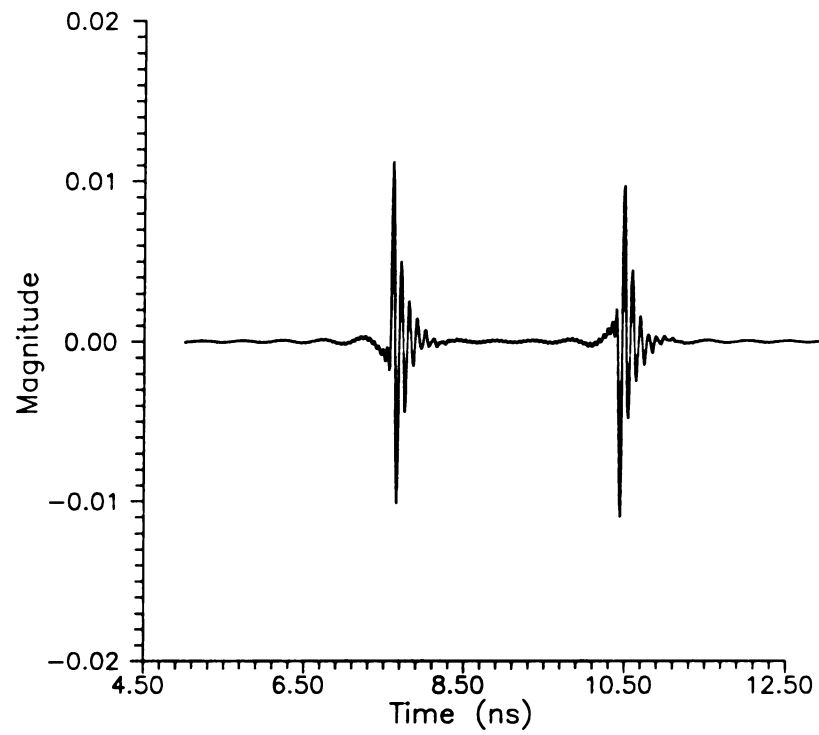
Figure 6.7   SMEP response of the object with rotational angle $\phi=45°$ under PO approximations.
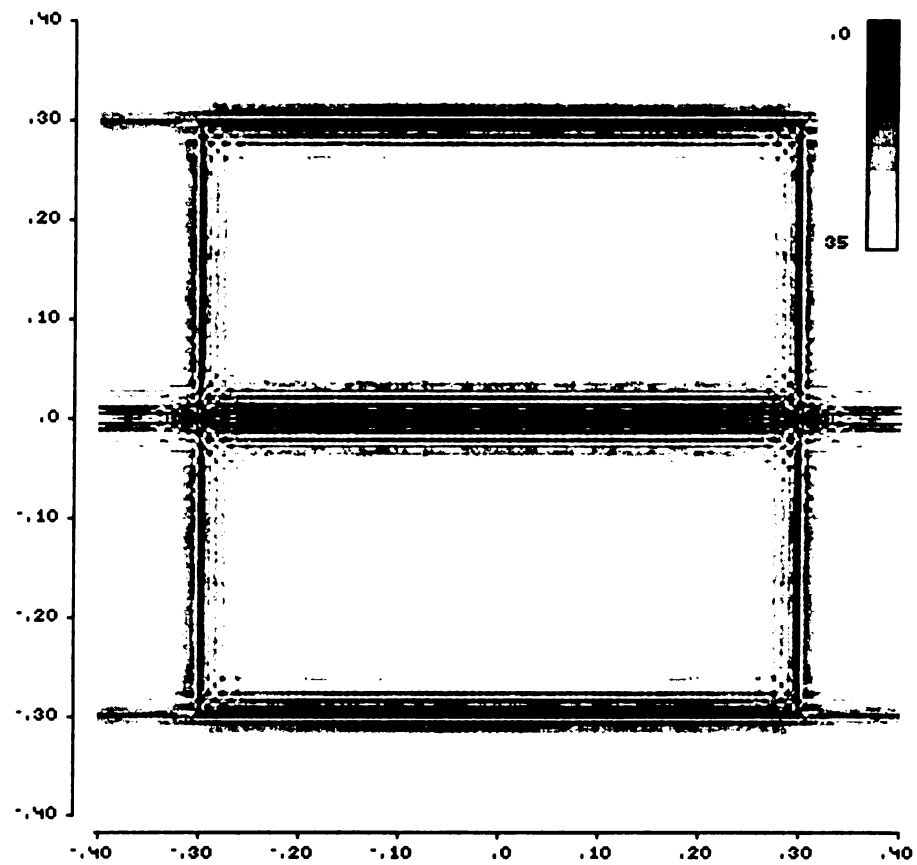
Figure 6.8 Image of the object from 0°-180° data in band 4-16GHz using the total scattered field.

145
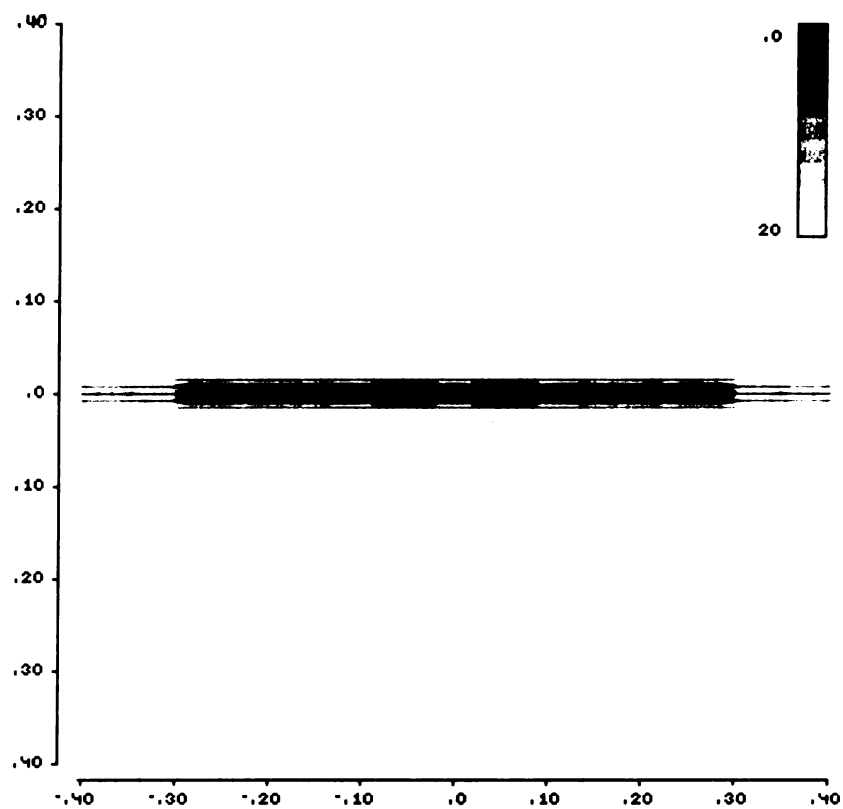
Figure 6.9. Image of the object from 0°-180° data in band 4-16 GHz under PO approximation.
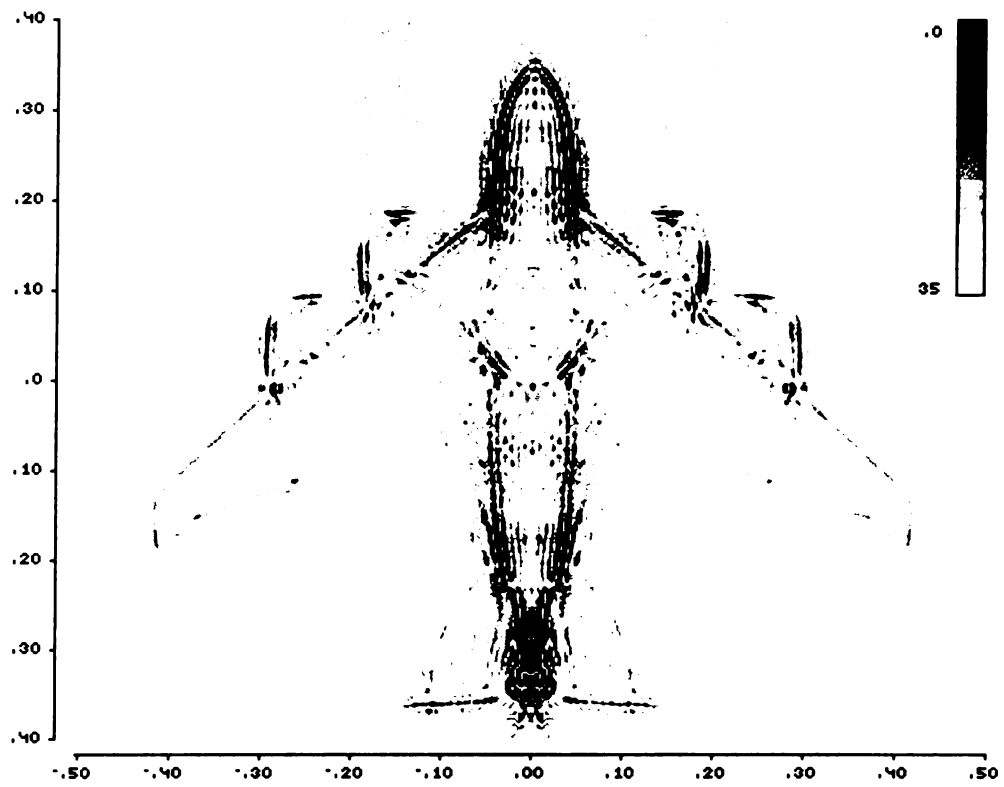
Figure 6.10. Image of B-52 from 0°-180° data in band 4-16 GHz using measured data.
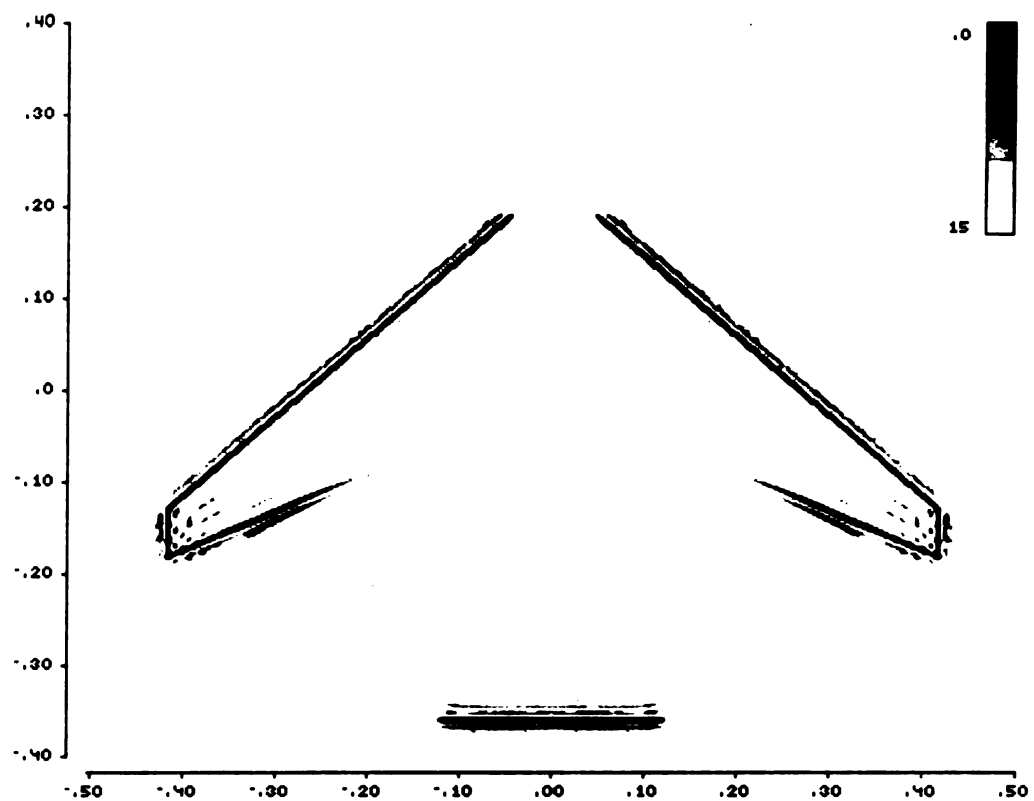
Figure 6.11. Image of main edges of B-52 from 0°-180° data in band 4-16 GHz using theoretical edge diffraction field
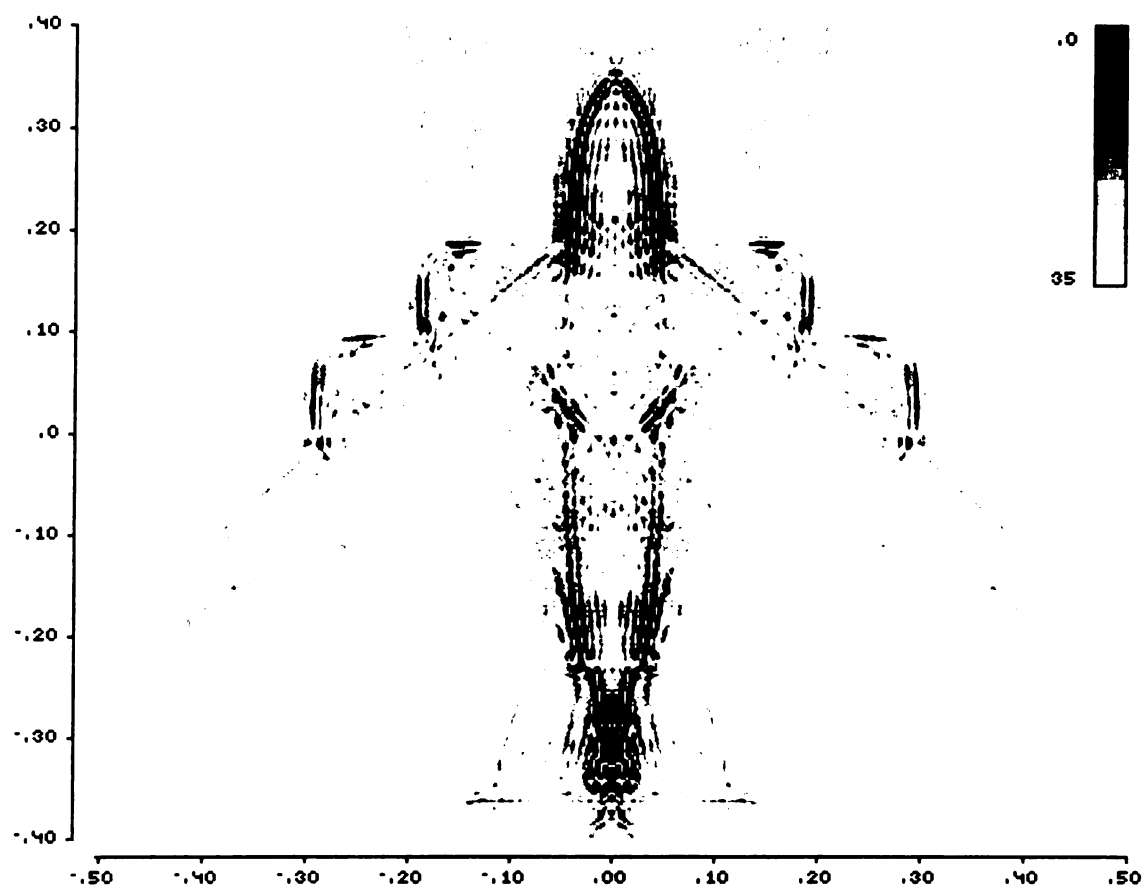
Figure 6.12. Image of B-52 from 0°-180° data in band 4-16 GHz with the incorporation of edge diffraction.

149

CHAPTER 7

CONCLUSIONS

This chapter summarizes what is achieved in this thesis and points out what remains to be studied further.

7.1   Summary of The Thesis

The most significant contribution of this thesis, from the view of the writer, is the development and the implementation of a time-domain radar imaging technique. In this technique, starting with the exact space-time magnetic field integral equation, and by using Radon's theory and a SMEP as the incident pulse, we obtain the complete inverse scattering identity which considers both illuminated and shadowed range contributions. We have developed the inverse scattering identities for both monostatic and bistatic cases, for special cases such as rotationally symmetric targets, for flying object, and for the 3-D case. The entire derivation is carried out directly in the time domain, and the incident magnetic field waveform is general. We can see from equation (3.22) that when the incident magnetic field is an impulse, step, or ramp, previous inverse scattering identities can be obtained. The reason why we chose the SMEP is its band-limited property and its ease of synthesis in the frequency domain.

In chapter 3 we have shown that the size and shape of an object (thickness

150

function) can be obtained from its cross sectional area functions, and the problem can be reduced to the classical Radon problem. Since the cross sectional area function can be estimated from the scattered field when the incident field is a SMEP, we can reconstruct the thickness function of the object using backprojection techniques which have been widely used in computed tomography, radio-astronomy, and geophysics. Chapter 4 gives two reconstruction algorithms. One is a time-domain approach called convolution backprojection. Another is the frequency-domain approach called filtered backprojection. Both approaches provide similar quality reconstructions. By using synthesized SMEP response data and the reconstruction algorithm, we have obtained very good images of several aircraft models. A simulation based on stepped-frequency, multi-aspect measurements of aircraft models produces clear images with highly-defined edges.

Chapter 5 deals with the limited-view problem. We have proposed two techniques to handle this practical situation. One approach is the method of projections onto convex sets (POCS). The basic principle of POCS is that each piece of a priori knowledge must be represented by a convex set onto which the current image estimate can be projected. It has been shown that if the intersection of these convex sets is nonempty then the sequence of cyclic projections will converge weakly to a point in this intersection. We extend this approach to radar imaging for the first time and show some useful results. Another approach which we have demonstrated is to process the available measured projections in order to generate an estimate of the full set of projections, an image which is called a sinogram. The goal of this approach is to recover the sinogram from the available measured data using linear prediction. Since the scattered field of a target can be written as a superposition of distinct specular reflections arising from scattering centers on the target, the position and strength of the scattering centers can be predicted using

linear prediction with the change of the observation angle. Thus, the missing data can be predicted before reconstructing the image. Big improvements in image reconstruction have been achieved using this technique, and some useful results have been shown in chapter 5.

In chapter 6 we point out that the PO approximation is inadequate for scattering problems of a complex shaped conducting object such as an aircraft. At high frequency, edge diffractions, multiple reflections, creeping waves, and surface travelling waves may also be important scattering mechanisms. Additionally, the spectral and angular windows for data are usually restricted by practical constraints. Therefore, the time domain image of an aircraft may be different from its geometrical shape. In chapter 6 we have investigated time domain imaging of aircraft employing SMEP responses, and interpret the reconstructed image from a new approach, based on analysis of the scattering mechanisms and the back-projection algorithm utilized in image retrieval. The time-domain inverse scattering identity with the incorporation of Geometrical Theory of Diffraction (GTD) is derived and some interesting experimental results are provided.

7.2   Suggestions for Further Studies

From the view of the writer, the following points are the suggestions for future research:

1).   At present the reconstruction has been limited to the 2-D case, so the next logical step is to extend the reconstruction algorithms to a 3-D object. The time-domain inverse scattering identity for 3-D cases has been derived in chapter 3 using a half Gaussian pulse modulated sine as an incident field. The well-developed reconstruction algorithms in other fields for the 3-D case can be extended and

applied to the 3-D inverse scattering problem.

2).   In addition to the SMEP, impulse, step, and ramp, other types of incident field waveforms may be used to obtain the cross-sectional area function.

3).   In sinogram restoration for the limited-view problem, 1-D linear prediction has been used to fill in the missing data. It is more efficient and may be more accurate if we use 2-D linear prediction, since the sinogram is a 2-D map.

APPENDIX A

APPENDIX A

ANECHOIC CHAMBER MEASUREMENTS

A.1 Introduction

There are two different schemes for performing transient measurements. The first method uses traditional time domain reflectometry methods [39], [40], [41], [42] while the second one utilizes a Fourier synthesis approach [43], [44], [45]. The time domain reflectometry method has the important advantages of time-gating and rapid speed of measurement, but suffers the disadvantage of limited dynamic range and equipment instability which leads to timing jitter. In this dissertation, we do not exploit this method.

A vector network analyzer is capable of measuring both the magnitude and phase of the S-parameters of two port network over a very wide frequency band. This capability gives the vector network analyzer the ability to synthesize the transient response of a target via the inverse discrete Fourier transform. Measurements using this configuration take longer than with time domain systems. Note that the sampling interval constraint limits the use of the network analyzer system when the antennas are used on a ground plane since the reflections from the edges of the ground screen and the laboratory ceiling cause alaising.

A typical free-field dual antenna frequency-domain measurement system is shown in Figure A.1. A measurement of S_{21} produces a measure of scattering from port 1 to port 2 from both the scatterer and the environment. Amplifiers are added to the transmit
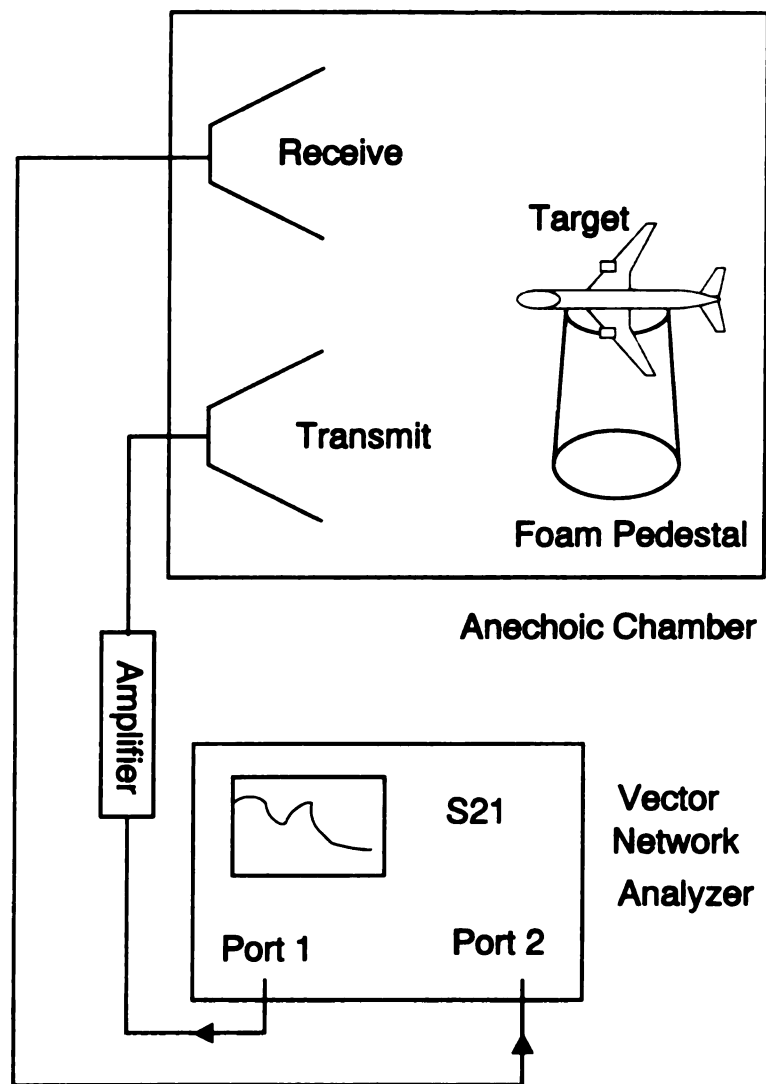
Figure A.1 Dual antenna free-field frequency-domain transient measurement system.

channel to help boost the dynamic range of the measurements. With the addition of wide-band horn antennas, the frequency range of the system has been extended from the band 1-7 GHz to the band 2-18 GHz. Also, a computer-controlled rotator allows measurements to be made automatically at a 0.15^0 aspect angle increment.

This Appendix reviews the calibration and deconvolution method of the measurement system developed by Ross [45]. Examples of measured spectral responses of calibration targets (i.e. sphere) are presented and compared with theory. Various methods which improve the measurements of aircraft models are described briefly and summarized.

A.2 Calibration Procedure

Ross made a significant contribution to automatic measurements in the anechoic chamber at the MSU EM lab. The size of chamber is 24 ft in length, 12 ft in width, and 12 ft in height. Here we will review the calibration procedure. To take full advantage of the wide frequency sweep available with a network analyzer, the clutter and system transfer function must be removed from the measurement. That is, all repeatable systematic errors associated with anechoic chamber clutter, antennas, and transmission lines should be removed from the raw measurement.

First, the background response measured when the chamber is empty is subtracted from the raw target measurement. Figure A.2 shows the spectral response of a 14 inch metal calibration sphere measured at 2-18 GHz. Other possible calibration targets include a thin wire. One of the difficulties with the wire is that the wire response is strongly aspect-dependent. It is very hard to determine the incident angle exactly. After the spectral response is zero-padded and transformed to the time domain, any interaction

156

terms and noise that are sufficiently delayed beyond the end of the calibration target response can be eliminated. The spectral response obtained by transforming the time-domain response using the FFT becomes much smoother than before as shown in Figure A.3. Next the system function can be found by dividing this response by the theoretical value.

The theoretical scattered field response of a sphere was first solved by Mie in 1908 [46]. It has also appeared in many books [47], [48]. The notation used in the course notes by Chen [49] is used here.

Consider a plane wave incident on a perfectly conducting sphere as illustrated in Figure A.4. The incident electric field is given by

$$\vec{E}^{inc}(\vec{r}) = \hat{x} E_0 \exp(-jkz) \tag{A.1}$$

The far zone scattered electric field is obtained by approximating the spherical vector wave functions in Mie series [48]

$$E^s_\theta = -jE_0 \frac{\exp(-jkR)}{kR} \sum_{n=1}^{\infty} \frac{2n+1}{n(n+1)} \left\{ a_n \frac{P_n^1(\cos\theta)}{\sin\theta} + b_n \left[\frac{\partial}{\partial\theta} P_n^1(\cos\theta) \right] \right\} \cos\phi \tag{A.2}$$

$$E^s_\phi = jE_0 \frac{\exp(-jkR)}{kR} \sum_{n=1}^{\infty} \frac{2n+1}{n(n+1)} \left\{ b_n \frac{P_n^1(\cos\theta)}{\sin\theta} + a_n \left[\frac{\partial}{\partial\theta} P_n^1(\cos\theta) \right] \right\} \sin\phi \tag{A.3}$$

where a_n and b_n are found using the boundary conditions and are given by

$$a_n = \frac{j_n(ka)}{h_n^{(2)}(ka)} \qquad b_n = \frac{\frac{\partial}{\partial R}(Rj_n(kR))|_{R=a}}{\frac{\partial}{\partial R}(Rh_n^{(2)}(kR))|_{R=a}} \tag{A.4}$$

For the back-scatter case, the following relations are used to the evaluation of the Mie series in equation (A.2) and (A.3)

157

$$P_n^1(\cos\theta) \Big|_{\theta=\pi} = -\frac{(-1)^n}{2} n(n+1) \qquad\qquad \text{(A.5)}$$

$$\frac{\partial}{\partial\theta} P_n^1(\cos\theta) \Big|_{\theta=\pi} = -\frac{(-1)^n}{2} n(n+1) \qquad\qquad \text{(A.6)}$$

The expressions shown in (A.2) and (A.3) are programmed with the use of widely available generalized Bessel function subroutines. These subroutines are very accurate and efficient.

Figure A.5 shows the theoretical waveform obtained using the above Mie series. The system transfer function obtained using this theoretical response is shown in Figure A.6. To provide verification of the calibration process, a second sphere 3 inches in diameter is used. Figure A.7 shows a comparison of the measured and theoretical spectral responses of the smaller sphere. The agreement is very good except in the high frequency region. This is probably due to the hole in the sphere and effects of windowing of extraneous system noise from the measured response.
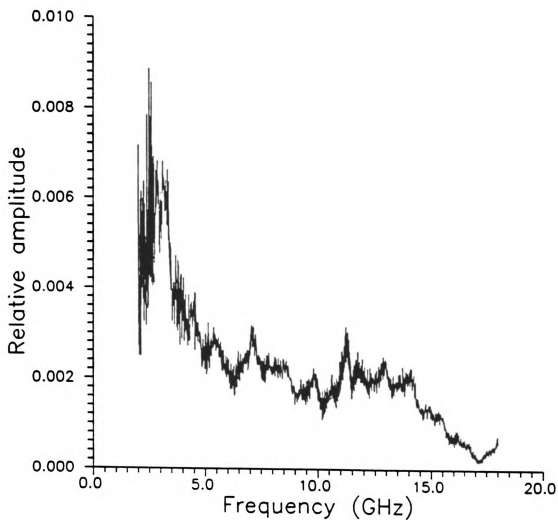
Figure A.2 Spectral response of 14 inch metal calibration sphere, measured using frequency domain system in MSU anechoic chamber.
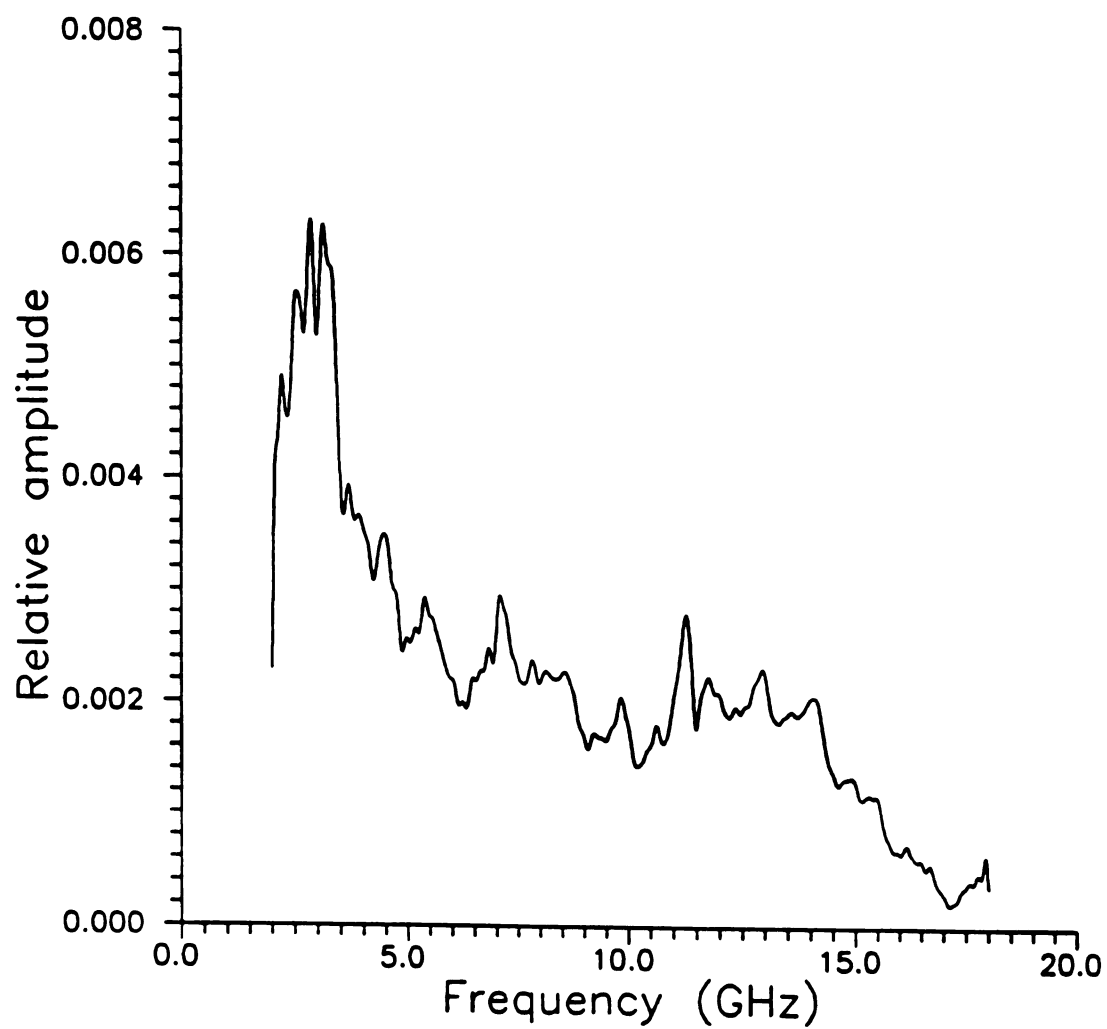
Figure A.3 Spectral response of 14 inch metal calibration sphere after time-domain filtering. Measured using frequency domain system in MSU anechoic chamber.
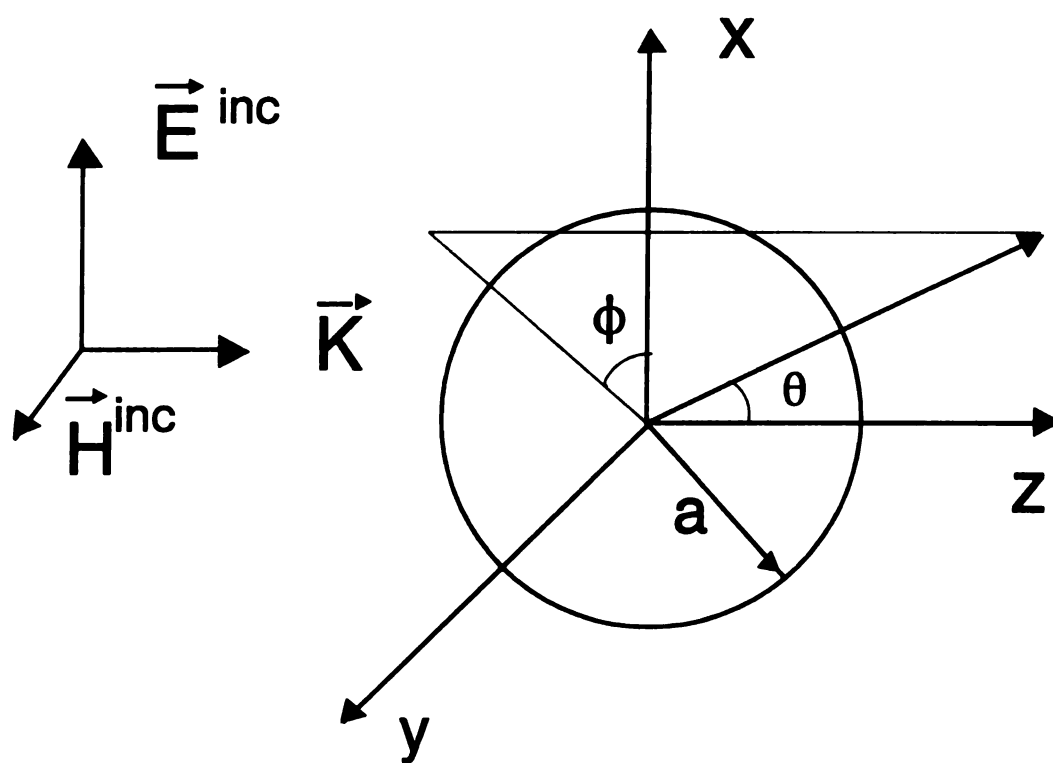
Figure A.4 Geometry for sphere scattering problem.
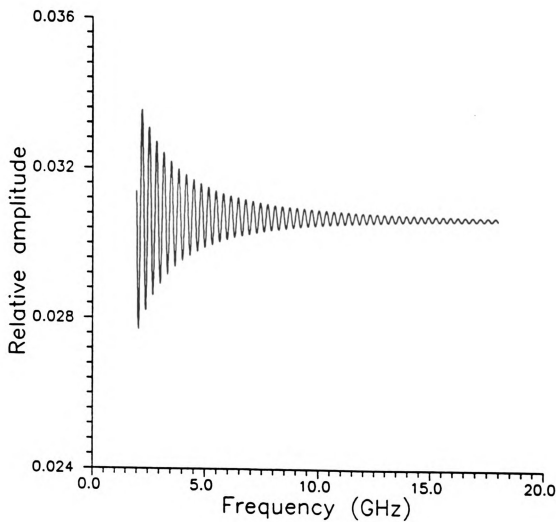
Figure A.5   Theoretical response of 14 inch metal calibration sphere calculated using Mie series for MSU anechoic chamber configuration.
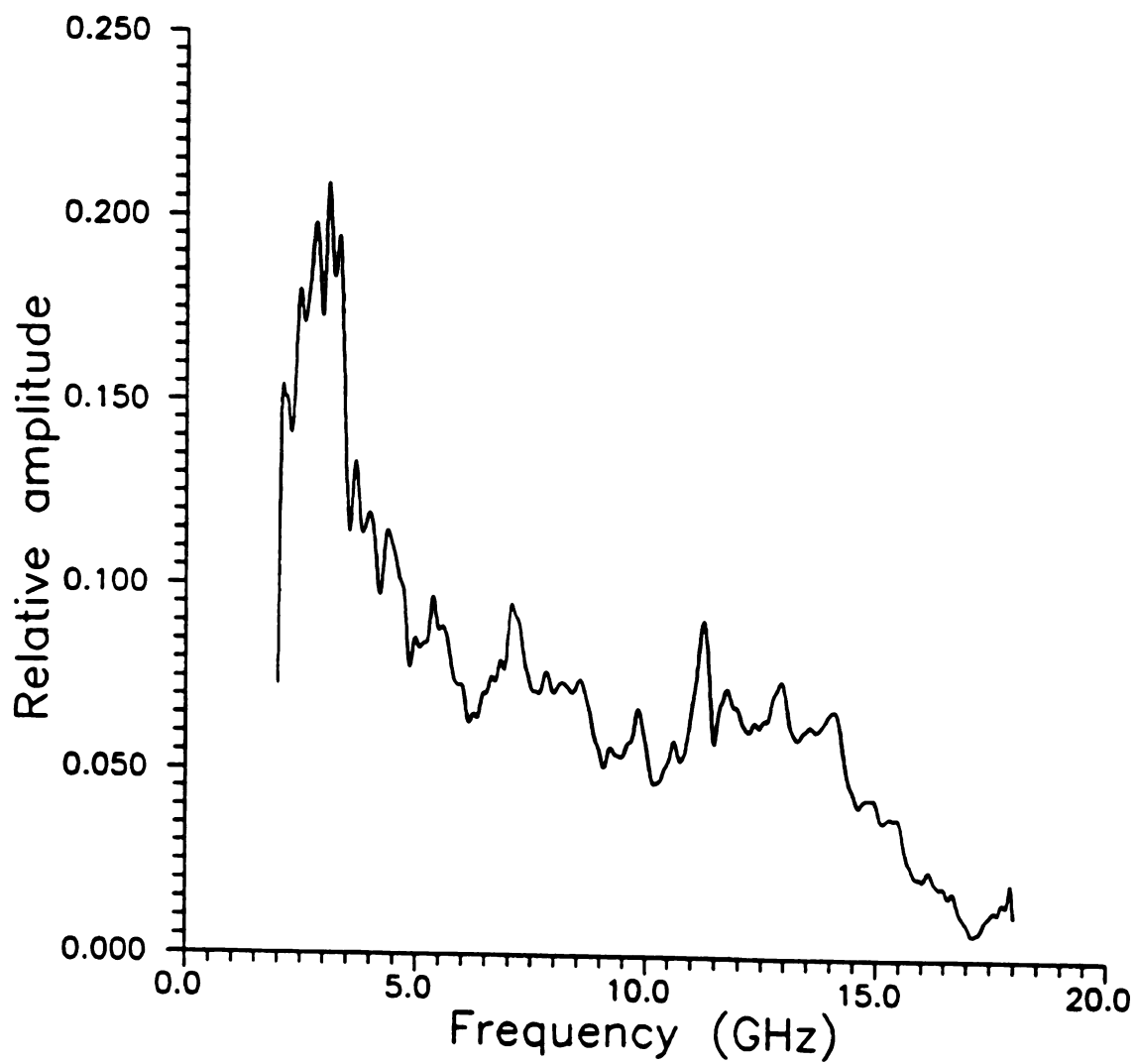
Figure A.6 Transfer function of frequency domain system obtained using 14 inch diameter sphere as calibration standard.

Figure A.7   Comparison of theoretical and experimental frequency responses of a 3 inch diameter sphere. Measurements performed using frequency domain system in MSU anechoic chamber.

APPENDIX B

APPENDIX B

EXPERIMENTAL EQUIPMENT

This appendix summarizes the apparatus used for the experimental portion of the research. The equipment used in the frequency domain scattering measurements is listed in Table B.1. There have been three different configurations used at EM lab in MSU so far. The "low-band" configuration uses a the PPL-5812 amplifier to amplify the signal fro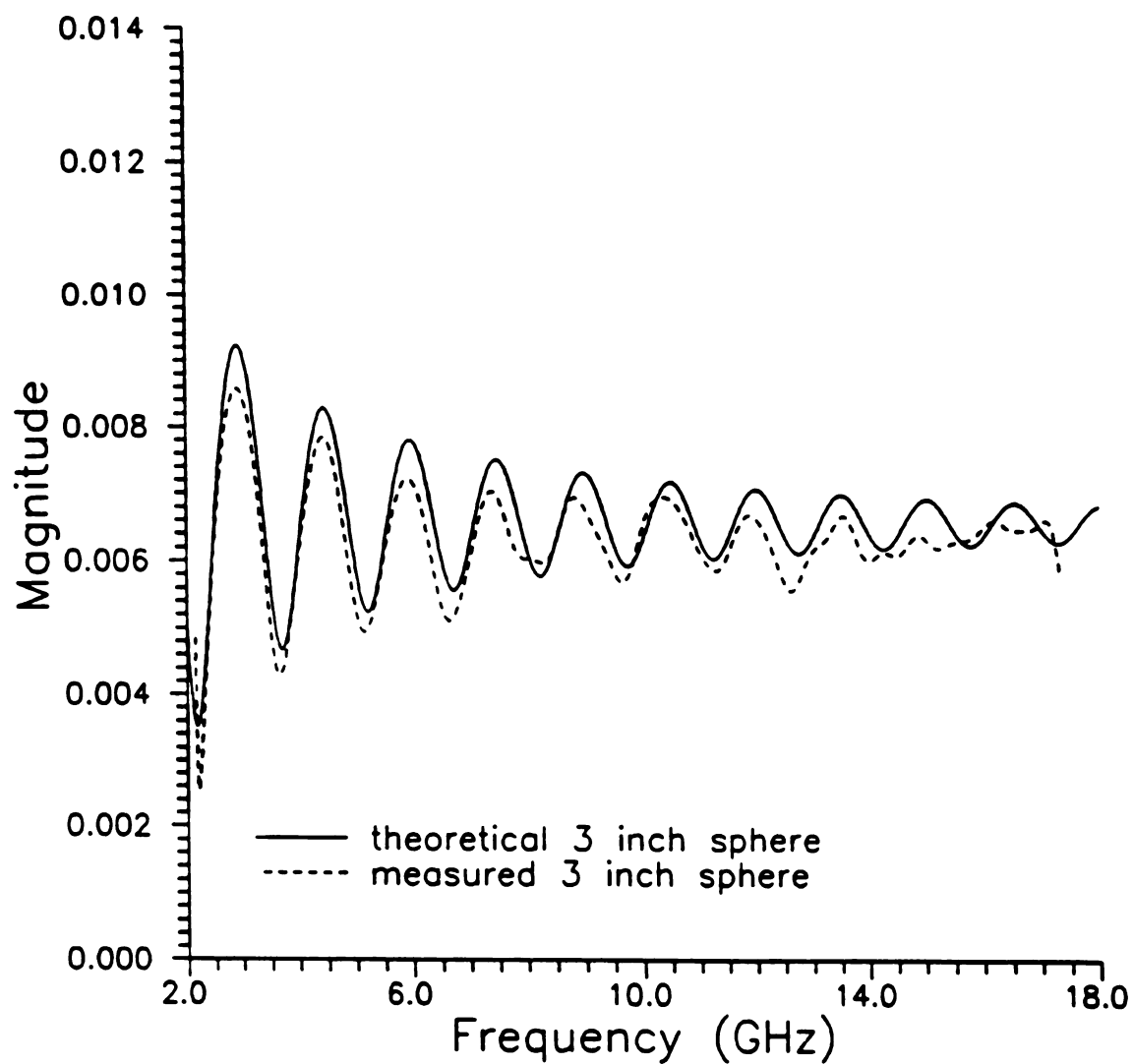m port 1 of the network analyzer. The parameters used in this configuration are shown in Table B.2. The "high-band" configuration uses the HP-8349B amplifier to amplify the signal from port 1 of the network analyzer. The parameters used in this configuration are described in Table B.3. The enhanced "high-band" configuration uses the HP-8349B amplifier too. The parameters used in this configuration are given in Table B.4.

To accurately characterize the measurement system, the network analyzer was used to measure the gain of the amplifiers and attenuations of the cables over a wide range of frequencies. The results of these measurements are given in the thesis by Ross [45] and are reproduced here to indicate the limitation of measurement system, the improvements, and baseline measurements to assess future equipment changes. The signal gain of the HP-8349B amplifier is shown in Figure B.1. Note that the gain is about 20 dB over 2 GHz. The gain of the PPL-5812 amplifier is shown in Figure B.2. The gain decreases a lot over 4 GHz. This attenuation

Table B.1   Equipment used for frequency domain scattering measurements.

Hewlett-Packard HP-8720B vector network analyzer

Hewlett-packard HP-8349B microwave amplifier

Picosecond pulse labs PPL-5812 10 dB broadband amplifier

American electronics laboratory AEL H-1734 wideband TEM horn antennas

23.5 foot RG-9B cable with N-type connector

22.5 foot RG-9B cable with N-type connector

B&K precision D.C. power supply 1610 (for PPL amplifier)

Insulated wire inc. AEL H-1498 wideband TEM horn antennas

12 foot low loss cable with SMA connector

Table B.2   Low band measurement parameters.

Measurement parameter:	S21
Frequency sweep:	0.4 - 4.4 GHz
number of points:	401
IF bandwidth:	100 Hz
number of averages:	10
Sweep time:	30 seconds

---

limits usage of amplifier in higher frequency range. Cable losses for the system are shown

in Figure B.3. Note that this cable is very lossy at high frequencies. Now a pair of low

loss flexible cables 12 foot in length are available to help improve range performance. Tests of new cables show a 3.5 dB loss at 20 GHz.

Table B.3   High band measurement parameters.

Measurement parameter:	S21
Frequency sweep:	1.0 - 7.0 GHz
number of points:	601
IF bandwidth:	100 Hz
number of averages:	10
Sweep time:	60 seconds

Table B.4   Enhanced high band measurement parameters.

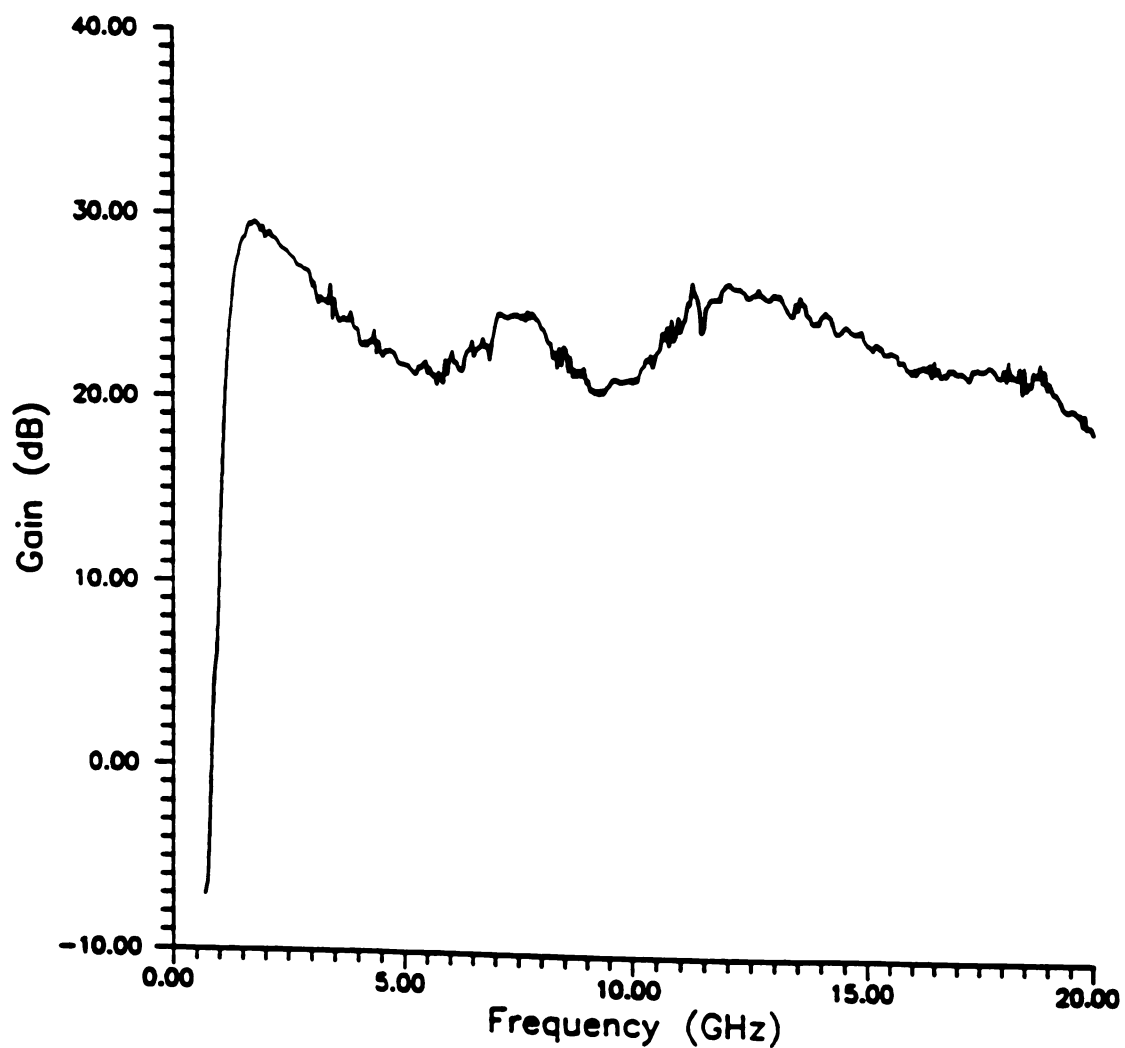| Measurement parameter:	S21
Frequency sweep:	2.0 - 18.0 GHz
number of points:	1601
IF bandwidth:	100 Hz
number of averages:	2
Sweep time:	60 seconds

Figure B.1 Gain of HP8349B Microwave Amplifier measured using HP-8720B network analyzer. Amplifier input power = -30 dB$_m$
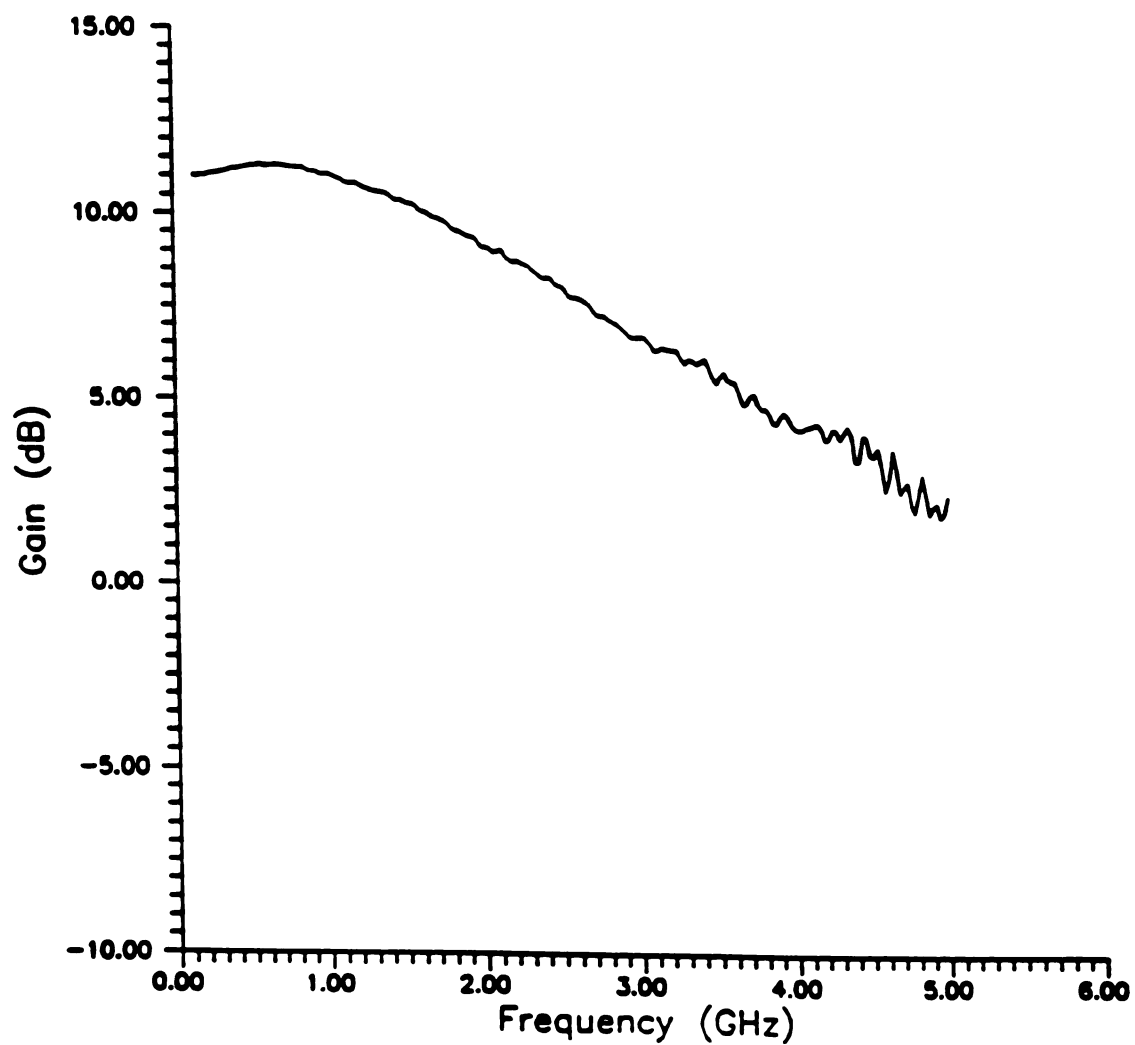
Figure B.2   Gain of PPL 5812 wide band amplifier measured using HP-8720B network analyzer. Amplifier input power = -10 dB$_m$.
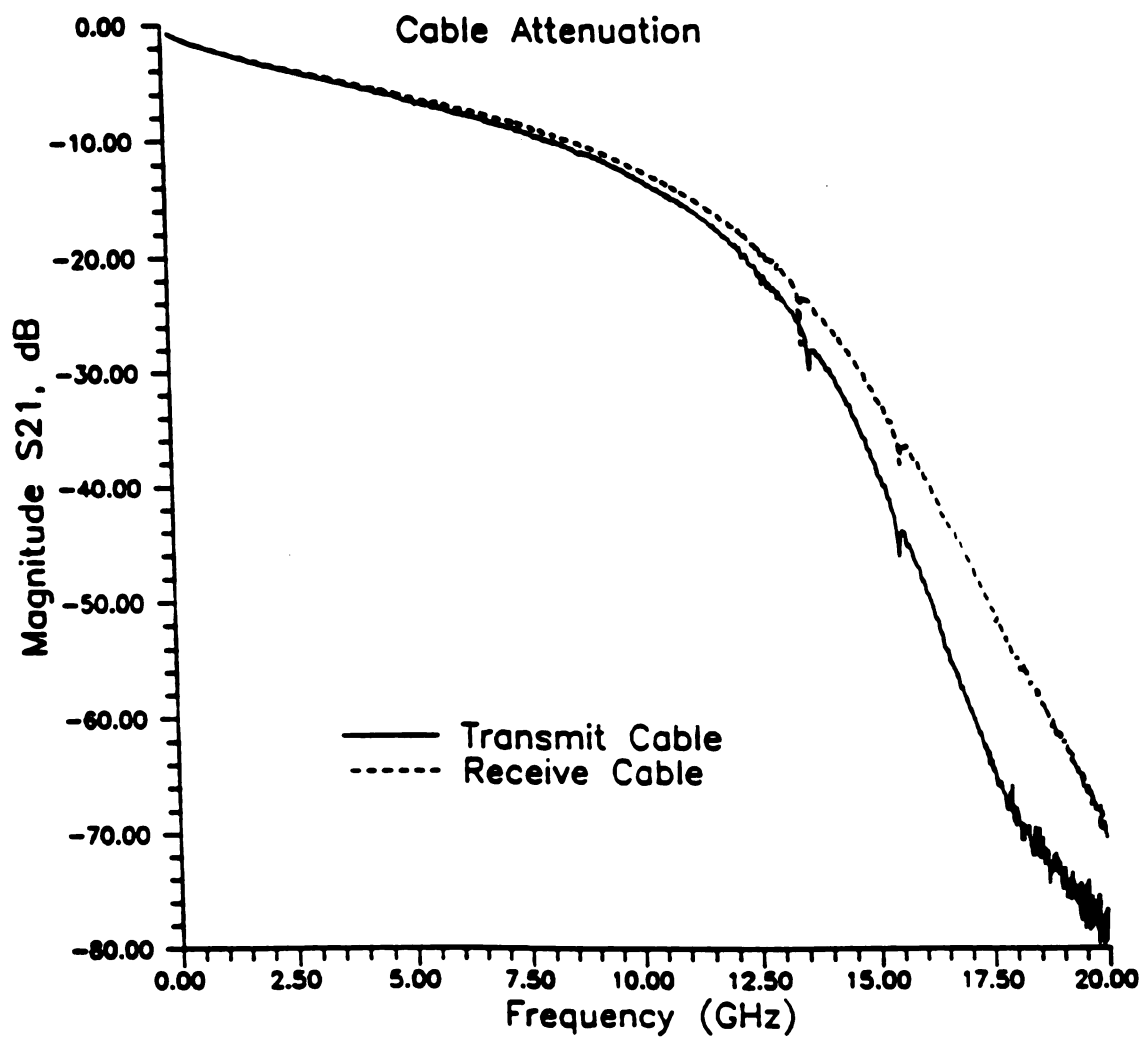
Figure B.3   Measured cable attenuation.

BIBLIOGRAPHY

BIBLIOGRAPHY

1. C. L. Bennett and G. F. Ross, "Time-Domain Electromagnetics and Its Applications" *Proceedings of IEEE,* vol. 66, No. 3, pp. 299-318 March 1978.

2. L. B. Felsen, *Transient Electromagnetic Fields*, Springer-Verlag, New York, 1976.

3. R. Mittra, *Computer Techniques for Electromagnetics*, Pergamon Press, New York, 1973.

4. B. P. Rynne, "Instability in Time Marching Method for Scattering Problems", *Electromagnetics* (1986) 6, pp. 129-144.

5. P. D. Smith, "Instabilities in Time Marching Methods for Scattering: Cause and Rectification", *Electromagnetics* (1990) 10, pp. 439-451.

6. E. M. Kennaugh and R. L. Cosgriff, "The use of impulse response in electromagnetic scattering problem," *REE National Convention Record*, part I. PP 72-77, 1958.

7. E. M. Kennaugh and D. L. Moffatt, "Transient and impulse response approximations", *Proc. IEEE*, vol. 53, pp.893-901, Aug. 1965.

8. J. D. Young, "Radar imaging from ramp response signatures", *IEEE Trans. Antennas Propagat.* vol AP-24 no. 3, pp.276-282, May 1976.

9. C. L. Bennett, "Time domain inverse scattering", *IEEE Trans. Antennas propagat.* vol. AP-29, no. 2, pp.213-219, Mar. 1981.

10. E. J. Rothwell, K. M. Chen, D. P. Nyquist and J. E. Ross, "Time domain imaging of airborne targets using ultra-wideband or short-pulse radar", *IEEE Trans. Antennas propagat.* vol. AP-43, no. 3, pp.327-329, Mar. 1995.

11. D. Ludwig, "The Radon transform on Euclidean spaces", *Comm. Pure and Applied Math.*, vol. XIX, pp.49-81, 1966.

12. Y. Das and W. M. Boerner, "On radar target shape estimation using algorithm for reconstruction from projections", *IEEE Trans. Antennas Propagat.*, vol AP-26, no. 2, pp.274-279, Feb. 1978.

13. S. R. Deans, *The Radon transform and some of its applications*. John Wiley & Sons, 1983.

14. N. N. Bojarski, "A survey of the physical optics inverse scattering identity", *IEEE Trans. Antennas Propagation,* vol. AP-30, No. 5, September 1982.

15. Y. Dai, E.J. Rothwell, D.P. Nyquist and K.M. Chen, "Time-domain imaging of radar targets using ultra-wideband or short pulse radars", *IEEE AP-S International Symposium and URSI Radio Science Meeting,* 1995.

16. J. Radon, "On the Determination of Function from their Integrals Along certain Manifolds", *Ber. Saechs. Akad. Wiss. Leipzig, Math. Physics Kl.,* vol. 69, pp. 262-277, 1917.

17. G. N. Ramachandran and A. V. lakshminarayanan, "Three dimensional reconstruction from radiographic and electron micrographic application of convolutions instead of Fourier transforms," *Proc. Nat.Acad. Sci. U.S.,* vol.68, pp. 21-24,1974.

18. A. K. Louis, "Picture reconstruction from projections in restricted range," *Math. Meth. Appl. Sci.,* vol. 2, pp.209-220, 1980.

19. T. Inoye, "Image reconstruction eith limited angle projection data," *IEEE Trans. Nucl. Sci.,* NS-26, pp.2666-2669, 1979.

20. J. A. Reeds and L. A. Shepp, "Limited angle reconstruction in tomography via squashing," *IEEE Trans. Med. Imaging,* vol. MI-6, pp.89-97.

21. M. I. Sezan and H. Stark, "Tomographic Image Reconstruction from Incomplete View Data by Convex Projections and Direct Fourier Inversion", *IEEE Trans. Medical Imaging,* vol. MI-3, No. 2, June, 1984.

22. L. M. Bregman, "Finding the common point of convex sets by the method of successive projections," *Dokl, Akad. Nauk USSR,* vol. 162, no. 3, pp. 487-490, 1965.

23. L. G. Gubin, B. T. Polyak, and E. V. Raik, "The method of projections for finding the common point of convex sets," *USSR Comput. Math. Math. Phys.,* vol. 7, no. 6, pp. 1-24, 1967.

24. D. C. Youla and H. Webb, "Image reconstruction by the method of projections onto convex sets-Part I," *IEEE TRANS. Med. Imaging,* vol. MI-1, pp 81-94, Oct. 1982.

25. K. M. Hanson G. W. Wecksung, "Bayesian approach to limited-angle

reconstruction in computed tomography," *Appl. Optics.* vol. 24, pp. 4028-4039, Dec. 1980.

26. P. Oskoui-Fard and H. Stark, "Tomographic Image Reconstruction Using the Theory of Convex Projections", *IEEE Trans. Medical Imaging*, vol. 7, No. 1, March,1988.

27. J. L. Prince and A. S. Willsky, "Hierarchical Reconstruction Using Geometry and Sinogram Restoration", *IEEE Trans. Image Processing*, vol. 2, No. 3, July, 1993.

28. G. T. Herman, *Image Reconstruction from Projections: The Fundamentals of Computerized Tomography*, New York: Acdemic, 1980.

29. J. Makhoul, "Linear Prediction: A Tutorial Review", *Proceedings of The IEEE*, vol. 63, No. 4, April, 1975.

30. J. G. Proakis and D. G. Manolakis, *Digital Signal Processing. Principle, Algorithm, and Applications. Macmillan, 1992.*

31. Y. Dai, E.J. Rothwell, D.P. Nyquist and K.M. Chen, "Time-domain imaging of radar targets using algorithm for reconstruction from projections radars", *IEEE Trans. Antennas Propergat.* Accepted for publication, 1997.

32. G. T. Ruck, D. E. barrick, W. D. Stuart and Krichbaum, *Radar Cross Section Handbook.* New York: Plenum.

33. G L. James, *Geometrical Theory of Diffraction for Electromagnetic Waves*, Third Edition, Herts SG1 1HQ, United Kingdom, 1986.

34. J. B. Keller, "Diffraction by an Aperture", *J. Appl. Physics*, vol. 28, pp.426-444, Apr. 1957.

35. P. Ya. Ufimtsev, "Approximate Computation of Diffraction of Plane Electromagnetic Waves at certain metal Objects - I. Diffraction Patterns at a wedge and Ribbon" *Sov. Phys. - Tech. Phys.* 27, pp. 1708-1718, 1957.

36. A. Michaeli, "Equivalent Edge Currents for Arbitrary Aspects of Observation", *IEEE Trans. Antennas Propagate.*, vol. AP-32, pp. 252-258, Mar. 1984.

37. A. Michaeli, "Elimination of Infinities in Equivalent Edge Currents, Part I: Fringe Current Components", *IEEE Trans. Antennas Propagate.*, vol. AP-34, pp. 912-918, July 1986.

38. D. P. Nyquist, "Antenna Theory", EE929A course notes, Michigan State University.

39. M. A. Morgan, "Time-domain scattering measurements," *IEEE Trans. Antennas Propagat. Newsletter*, vol. 6, pp. 5-9, August 1984.

40. M. A. Morgan and B. W. McDaniel, "Transient electromagnetic scattering: Data acquisition & signal processing," *IEEE Trans. on Instrumentation and Measurement*, vol. 37, pp. 263-267, June 1988.

41. M. A. Morgan and N. J. Walsh, "Ultra-wide-band transient electromagnetic scattering laboratory," *IEEE Trans. Antennas Propagat.*, vol. 39, pp. 1230-1234, August 1991.

42. M. A. Morgan, "Ultra-wideband impulse scattering measurements," *IEEE Trans. Antennas Propagat.*, vol. 42, pp. 840-846, June 1994.

43. F. T. Ulaby, T. F. Haddock, J. East and M. Whitt, "A millimeter-wave network analyzer based scatterometer," *IEEE Trans. on Geoscience and Remote Sensing*, Vol. GE-26, pp. 75-81, Jan. 1988.

44. B. Drachman, "Two methods to deconvolve: L^1-method using simple algorithm and L_2-method using least squares and a parameter," *IEEE Trans. Antennas Propagat.*, vol. 32, pp. 219-225, March 1984.

45. J. E. Ross, "Application of Transient Electromagnetic Fields to Radar Target Discrimination," Ph. D. dissertation, Michigan State University, 1992.

46. Mie, *Ann. Physik*, 25, 377, 1908.

47. J. A. Stratton, *Electromagnetic theory*, New York and London: McGraw-Hill, 1941, pp. 563-573.

48. R. F. Harrington, *Time harmonic electromagnetic fields*, New York: McGraw-Hill, 1941.

49. K. M. Chen, *EE 836-electromagnetic waves I: course notes*, Michigan State University, 1992.

50. G. Dural and D. L. Moffatt, "ISAR Imaging to Identify Basic Scattering Mechanism," *IEEE Trans. Antenna Propagat.*, vol. 42, No. 1, pp.99-110, 1994

51. D. L. Mensa, *High Resolution Radar Cross-Section Imaging*. Norwood, MA: Artech House, 1991.

52. S. Reichel, "Time domain of bistatic inverse scattering identity," Department of Electrical Engineering, Michigan State University, 1995.

53. H. Li, N. H. Farhat, Y. Shen, and C. Werner, "Image Understanding and

Interpretation in Microwave Diversity Imaging," *IEEE Trans. Antennas Propagat.,* vol. 37, No. 8, pp.1048-1057, August 1989.